STUDY OF DIRECT INJECTION FUEL DELIVERY IN A SPARK-IGNITED NATURAL GAS ENGINE

A Thesis

by

KYLE RAYLAND BEURLOT

Submitted to the Office of Graduate and Professional Studies of
Texas A&M University
in partial fulfillment of the requirements for the degree of

MASTER OF SCIENCE

Chair of Committee,	Timothy J. Jacobs
Committee Members,	Harry A. Hogan
	Hamn-Ching Chen
Head of Department,	Bryan P. Rasmussen

August 2021

Major Subject: Mechanical Engineering

ABSTRACT

Large bore, natural gas two-stroke engines form a vital backbone of the pipeline industry. With current green initiatives and governmental pushes to reduce harmful emissions, such as oxides of nitrogen (NOx) and hydrocarbons (HC), the need to continually improve the performance of an ageing compressor engine fleet is critical. A practical way to reduce NOx and HC emissions has been to pursue increasingly lean fuel to air ratio ignition limits, but lean mixtures are exceptionally hard to ignite and result in frequent misfires. Misfires produce high levels of harmful emissions, introducing a multitude of complexities related to engine stability and reliable operation. Building understanding of why these mixtures are difficult to ignite, or conversely, how to take a lean mixture and make it easier and more reliable to burn, is critical to enabling more restrictively lean engine operation.

This study sought to simulate a full crank cycle of the Ajax E-565, a single-cylinder, large bore natural gas two-stroke similar to those of the pipeline industry. To accomplish this, a computational fluid dynamic simulation of the engine was built in commercial software Converge CFD, then validated against experimentally measured datasets at a variety of spark timings. After successful validation, the performance impact of manipulating a low pressure system that delivers fuel directly into the engine cylinder was studied. This was examined by first lengthening the duration of fuel injection compared to standard baseline, then shortening the injection. Global equivalence ratio (ER) was maintained as a constant by varying fuel header pressures to

compensate for the altered injection durations. Finally, the best performing injection parameters were tested at progressively lower fuel header pressures until misfire to analyze fuel and performance benefits. Overall, the highest cylinder pressure and lowest fuel consumption was obtained by decreasing the fuel injection period and using higher fuel injection pressures. Injection pressures should be held as high as possible without impinging upon the cylinder walls and piston or over-penetrating the scavenging loop flow field.

DEDICATION

To my mother, father, and sister: I never would have made it here without you.

ACKNOWLEDGEMENTS

I would like to begin by thanking my committee chair, Dr. Jacobs, for being a truly gifted mentor and positive influence ever since my days in my undergrad. He never ceases to amaze me with his unending wisdom, straightforward approach, and willingness to always find time for his students. I feel truly blessed to have been given the opportunity to work with him.

To Dr. Mark Patterson, I extend my deepest gratitude. Though he had no reason to be so supportive and engaging, he never failed to answer a call or email, and his expertise was constantly invaluable. I don't know how many times he and Dr. Jacobs helped me navigate obstacles in my way.

I would also like to thank my fellow researchers within the AERL for their fellowship, support, and assistance in conducting my work. Thank you for always putting up with answering incessant questions, and at times, being the best classmates anyone could wish for.

Convergent Science is thanked for their generous support in allowing the use of Converge CFD. To John Etcheverry and Dr. Alireza Mashayekh of Convergent Science, my sincerest thanks for helping me throughout this work. Texas A&M HPRC is thanked for their support in providing abundant computational resources.

Finally, I would like to thank my committee members of Dr. Jacobs, Dr. Hogan, and Dr. Chen for their exceptional willingness to lend their time, expertise, and support of this study. Thank you, everyone, for embarking on this journey with me.

CONTRIBUTORS AND FUNDING SOURCES

Contributors

This work was supervised by a thesis committee consisting of Dr. Timothy Jacobs (advisor) and Dr. Harry Hogan of the Department of Mechanical Engineering and Dr. Hamn-Ching Chen of the Department of Civil Engineering.

This work validated numerical simulations using experimental datasets that were collected by Dr. Abdullah Bajwa and AERL researchers in late 2019. The work also utilizes the framework of a Converge CFD simulation created by Dr. Alireza Mashayekh during his dissertation work under Dr. Timothy Jacobs, published in 2017. All other work conducted for the thesis was completed by the student independently.

Funding Sources

This work was not supported by any external funding sources.

NOMENCLATURE

AERL	Advanced Engine Research Laboratory at Texas A&M University
AFR	Air to fuel ratio
AMR	Adaptive Mesh Refinement
ATDC	After top dead center
BDC	Bottom dead center piston position
BTDC	Before top dead center
CA	Crank angle
CAD	Crank angle degrees
CFD	Computational fluid dynamics
DI	Direct injection
EPC	Exhaust port close timing
EPO	Exhaust port open timing
ER	Equivalence ratio
FE	Fixed embedding grid control
FVC	Fuel valve closing
FVO	Fuel valve opening
HC	Hydrocarbon emissions
IC	Internal combustion
ICE	Internal combustion engine
IPC	Intake port close timing

IPO	Intake port open timing
LoPP	Location of peak pressure
MCC	Main combustion chamber, also known as the cylinder
MFB	Mass fraction burned
NO_x	Oxides of nitrogen (x tends to represent that there can be one or two typical oxygen atoms, such as in NO or NO_2)
RANS	Reynolds-Averaged Navier-Stokes
RNG	Re-normalization group
ROHR	Rate of heat release
RPM	Rotations per minute
SBS	Sub-grid scale
TDC	Top dead center piston position

TABLE OF CONTENTS

Page

LIST OF FIGURES

Page

LIST OF TABLES

Page

1. INTRODUCTION

For the past few decades, large bore natural gas two-stroke engines have served as an integral component of the pipeline industry. These engines promote both reliable and stable power necessary to provide continuous operation in a multitude of pipeline and oilfield operations that form the backbone of the energy industry in the United States. An example of such an engine is the Cooper Ajax E-565. This engine, the one under study herein, is a large bore, single cylinder, natural gas two-stroke engine known for a rugged design that not only continues to operate in adverse climates but also meets stringent federal emission regulations [1]. Installed in an instrumented test cell at the Texas A&M Advanced Engine Research Laboratory (AERL), the E-565 will serve as the subject of this study.

1.1. Background and Motivation

Large bore, natural gas two-stroke engines are exceptionally vital to the pipeline industry. With a governmental push to reduce harmful emissions, such as nitrogen oxides (NOx), hydrocarbons (HC) or other greenhouse gases, the need to continually improve and upgrade the performance of the legacy compressor engine fleet is critical. One primary way to reduce NOx emissions has been to pursue increasingly lean fuel to air ratio ignition limits. Decreasing the amount of fuel in the chamber relative to the inducted air serves to reduce the combustion temperatures produced, and this significantly reduces the production of NOx species. Similarly, the greater presence of air relative to the amount of fuel also helps ensure that all of the fuel ignites, reducing overall HC species that are released into the exhaust and atmosphere. However, while lean air to fuel targets enable advantages in terms of potential

emissions benefits, the mixture can also become exceptionally hard to ignite, introducing a multitude of complexities for engine designers regarding both engine stability and reliable cycle to cycle performance. In particular, exceptionally lean ignition can introduce higher rates of misfires and combustion instabilities, which ultimately produce cycles of significantly increased emissions [2].

Understanding why these mixtures are hard to ignite, or conversely, how to take the same leanness of mixture and make it easier and more reliable to ignite, are critical pieces of information to further enable attaining more restrictive engine operation targets. Experimental and numerical methods of analysis provide an opportunity for research engineers to study the underlying processes responsible for the overall performance of the engine under controlled conditions. Both research methods can provide ways to examine new theories, test redesigns of original parts for better functionality, or develop entirely new systems to improve engine operation.

1.2. The Ajax E-565 Engine

The Ajax E-565 of this study is a two-stroke, large bore, spark-ignited, natural gas engine. While only a single cylinder, it shares many of the design characteristics with common engines of the natural gas pipeline industry. A number of the characteristic parameters of the E-565 are shown below in Table 1.1 [1]. A description of how a two-stroke engine operates is included in the following section 1.3 Principles of the Two-Stroke Cycle.

Table 1.1: Specifications of the Ajax E-565.

Rated Continuous BHP	29.8 kW (40 hp)
Torque	542 N·m (400 ft-lb)
Rated Speed	525 RPM
Bore x Stroke	216mm x 254 mm (8.5” x 10”)
Compression Ratio	6:1

1.3. Principles of the Two-Stroke Cycle

A two-stroke engine design, like the one present in the Ajax E-565 of this study, is one that completes a full power cycle in a single rotation of the crankshaft. This involves one upward stroke of the piston and one downward stroke, known as the compression stroke and the expansion stroke [3]. In order to accomplish this, a fresh charge must first be compressed, ignited and burned, then exhausted during the scavenging process before beginning again [4].

Starting from bottom dead center (BDC) and moving up toward top dead center (TDC) and the cylinder head, the piston first covers and closes the intake ports then the exhaust ports soon after, as shown below in Figure 1.1. Once the piston has crossed the exhaust ports, the cylinder is closed, and a fresh supply of air has been trapped. Shortly before the exhaust port closes, the direct injection valve in the cylinder head opens and begins to release a stream of fuel. As the fuel injection finishes and the valve closes, the piston continues toward TDC, compressing the fuel and air mixture as shown in the compression stroke of Figure 1.1. While the fresh mixture is compressed, a partial vacuum is simultaneously created on the underside of the piston inside the stuffing box, drawing in

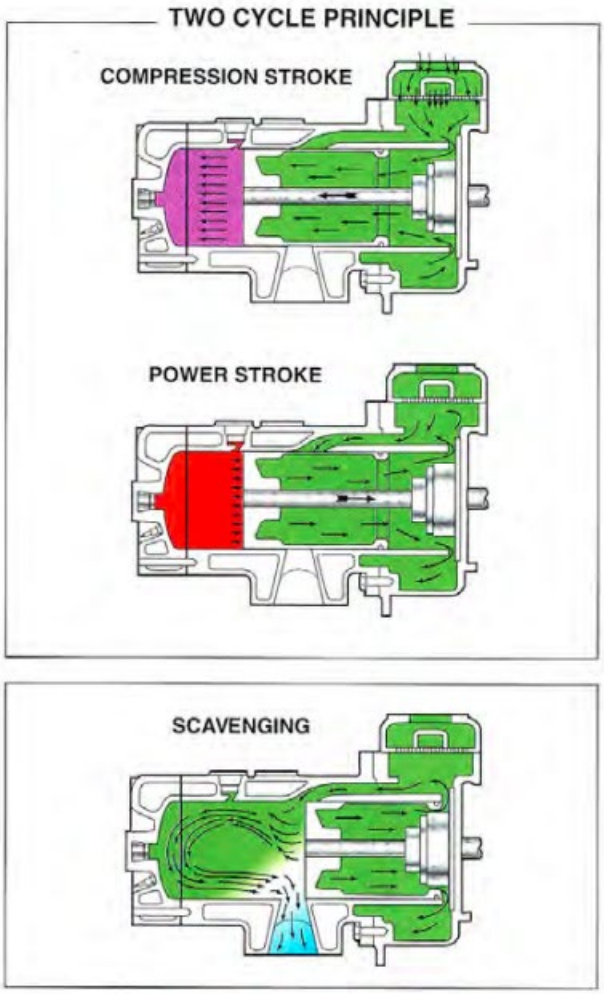

Figure 1.1: An illustration of the two-stroke engine cycle depicted with the Ajax E-565 [5].

fresh air from the outside. Just before the piston reaches TDC, the spark plug emits an electric discharge, providing energy to light off the combustion event. A flame propagates through the mixture, producing a rise in pressure due to expanding combustion products. The pressure begins to force the piston back downward, producing the power stroke depicted above [6].

The gases continue to expand until the piston eventually crosses the exhaust ports during the scavenging phase. The burned gases begin to flow out of the main chamber, and the piston crosses the intake ports shortly thereafter. The downward action of the piston during the expansion stroke also serves to pressurize the air previously drawn into the stuffing box. Once the intake ports open, the incoming pressurized fresh air helps to flush the burned gases out, and the piston returns to BDC to begin the cycle again [4].

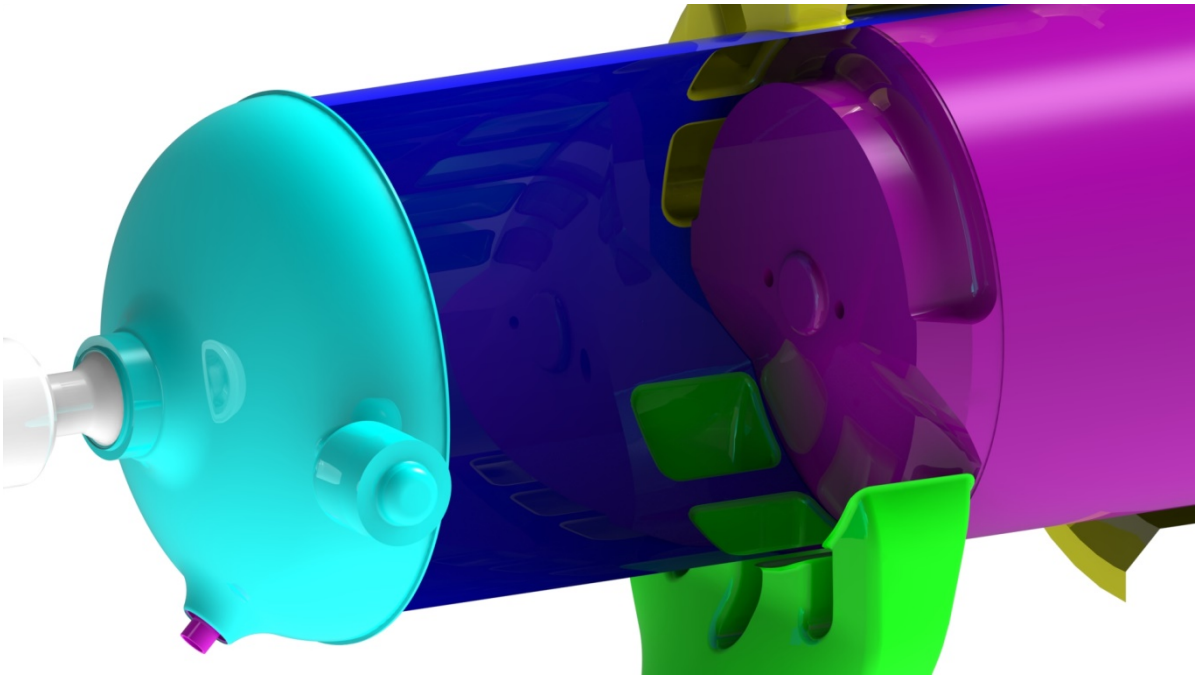

Figure 1.2: Piston crown and ports on the E-565.

While a number of different scavenging arrangements exist, the E-565 of this study utilizes cross-scavenging. In a cross-scavenged engine, the intake and exhaust ports are drilled on opposing sides of the cylinder, creating the swirled flow toward the head that is visible during the scavenging phase of Figure 1.1. Additionally, the piston crown of the E-565 is specifically designed with a deflector on the intake side and a gradual slope on the

exhaust side. Shown in Figure 1.2 above, the exhaust ports are visible in green, while the intake ports are shown in yellow and the piston crown purple. The deflector serves to direct the fresh air up toward the cylinder head, reducing loss of fresh charge through the exhaust ports and pushing burned gases out, while the gradual slope promotes flow of burned gases.

1.4. Advantages to Using CFD

Experimental and numerical investigations are different ways to analyze and examine the processes occurring in these engines, but there are a few advantages to pursuing the use of computational fluid dynamics (CFD) over traditional experimentation. First, experimental analysis can be exceptionally cost prohibitive and limited by the ability to effectively instrument an engine. While the Ajax E-565 of this study is single cylinder and relatively small by compressor station engine standards, other legacy engines have more cylinders and are significantly larger in comparison. Positioning proper sensors and probes can be difficult, or in some cases impossible, depending on the desired measurement location. CFD largely eliminates both of these concerns, while also enabling the ability to track measurements at the same locations that would be impossible to physically implement. With CFD, the costs associated with additional sensor installation, maintenance, and calibration are entirely eliminated and reduced to the hourly cost to create the model, the cost of computational time, and the cost of necessary software.

CFD also opens more doors beyond cost savings and the ability to study regions of the engine previously inaccessible by traditional means. CFD can provide full details of the fluid flow and combustion, as well as track a number of thermodynamic, performance, and emissions-related parameters: pressure, temperature, air-to-fuel ratio (AFR), spatial

equivalence ratio (ER) distribution, various energies, and more. A unique aspect of CFD is also the ability to start or restart simulations from any point in time and with any combination of desired parameters. This particular aspect allows for studying isolated periods of the engine cycle, for example the fuel injection process, in ways where factors like injection timing or fuel injection pressure can be independently and carefully controlled. This enables direct comparison between multiple cases from identical initial conditions. Such directly related and controlled studies can be difficult to produce experimentally, but a well-validated numerical CFD model can do so relatively easily and at a fraction of the cost and time required.

1.5. Motivation for Choosing CONVERGE CFD

The process of simulating an internal combustion (IC) engine utilizing CFD can be an incredibly daunting task. To begin with, geometries are frequently intricately dependent on high numbers of parts and operation is both highly transient and spatially varying. Not only that, but performance can vary widely depending on combustion characteristics. For the purpose of this work, Converge CFD was chosen as a widely used and industry proven IC modeling software package [7]. Converge possesses a number of unique features that are highly suited to simulating the E-565 two-stroke.

One of the most attractive features of Converge CFD is autonomous meshing. Converge generates the domain mesh at runtime rather than being a time consuming manual process by the user. The generated grid is always perfectly orthogonal and fit directly to imported geometry, rather than a common CFD approach to shift the mesh as the geometry moves [8]. The feature allows the solver to adjust the grid within each simulation time step

and also allows for implementation of a number of refinement techniques, such as adaptive mesh refinement (AMR) and fixed embedding (FE). Although these techniques will be discussed in great detail in 2.1.11 Base Grid and Grid Control Methods, they ultimately allow the solver to increase resolution in areas of complex processes, improving solution accuracy without sacrificing computational efficiency [9].

Converge also implements the SAGE detailed chemistry solver. SAGE makes use of a chemical kinetics approach for chemistry solutions that are fully coupled with the flow solver, but the chemistry and flow solvers are still implemented in a parallel and independent fashion. Similarly, the Converge version 3.0 solver used in this work has undergone significant improvements to load balancing across high core performance computing implementations. This allows significantly faster computations and better scaling compared to previous versions [10].

1.6. Objectives of the Study

The objective of this project is to accurately simulate a full crank cycle of the engine's cylinder, then use the simulation as a base model to analyze performance changes by manipulating the low pressure direct injection system. In order to meet these objectives, a number of the following subtasks need to be completed.

1.6.1. Simulation of Overall Ajax E-565 Engine Cycle

In order to accurately simulate the cycle as a whole, each individual process of the two-stroke cycle needs to be properly implemented. Starting from the beginning of the simulation at exhaust port opening (EPO), the existing gases in the chamber need to be flushed through the exhaust manifold, and the fresh charge needs to cross-scavenge properly

from the intake manifold and into the main chamber (MCC). Particularly with the planned removal of the reed valve componentry when converting to direct injection (DI), the simulation still needs to be able to accurately model the airflows through the intake manifold. With the introduction of the DI system, the stuffing box and intake manifold no longer need to model the mixing of air and fuel, but the fuel does need to properly mix into the MCC from the DI system. The interaction between the flow exiting the exhaust ports, the flow entering from the intake manifold, and the flow through the DI valve is highly critical to ensuring the proper mixing characteristics, and this can significantly influence every component of combustion performance within the MCC. Manipulating the DI valve parameters and resulting mixing characteristics to influence combustion serves as a major objective of this study. Upon successful completion of scavenging modeling and then the combustion process, overall simulation results will be validated against experimentally obtained data across multiple spark timing datasets including nominal, advanced, and retarded timing. Successful validation across such targets then builds trust in the model to be used to predict real-world engine behavior across a multitude of varied parameters.

1.6.2. Accurately Model the Direct Injection System

During the creation of the overall model, accurately representing the behavior of the DI system is critical to obtaining the correct MCC fuel to air ER, as well as overall chamber stratification. Since the DI system installed on the AERL engine is hydraulically controlled, it is exceptionally difficult to determine the correct valve motion profile without dedicated engine teardown and bench testing, which even then can fail to capture the true nature of the action due to lack of an actual firing engine cycle. The hydraulics are cam-driven in

actuation, but the nature of the system introduces a lag between the cam open and closure timing versus when the cylinder-mounted valve actually starts to move. In addition to the open and closing times, the overall shape of the profile between fully closed and fully open (as well as the maximum lift distance itself) influences the fluid interaction of the fuel stream entering the air scavenging loop during the intake process. In addition, with only a rough estimate of the fuel header pressure due to measurements taking place upstream of the engine governor, the determination of the correct profile requires significant research and extensive iteration during the validation process.

1.6.3. Pressure and Fuel Delivery Study

After successfully modeling the engine processes, including operation of the DI system, and validating the numerical CFD simulation against experimentally obtained datasets across three different spark timing points, the simulation can be trusted to sufficiently predict real-world performance. For this study, the valve lift profile will be modified to behave more like newer electronic valve systems, with easier-to-define open/close timings and shorter, well-defined transitions between minimum and maximum lift. First, a baseline will be produced with a simplified “electronic” profile with similar timings to the actual engine’s hydraulics with the intent to reproduce similar behavior. Subsequently, the open timings, close timings, and fuel header pressure will be modified (while maintaining constant maximum lift) to produce changes in the overall MCC pressure traces. The “electronic” valve profiles would be created such that the overall duration of valve timing is shortened or lengthened, but the header pressure is raised or lowered to produce the same global ER across all cases. This would establish which profiles, longer or

shorter durations, produce the most favorable stratification for a low pressure injection system, or in other words, which of these profiles produce the most pressure and power for the same amount of fuel. These few profiles will then be tested at lower and lower header pressures to reach a minimum global ER before misfire.

The goal is that manipulation of stratification in the MCC can promote easier ignition near the spark plug, thus enabling leaner global ER targets for potential emissions reduction. While ability to use less fuel produces a leaner mixture and lower temperatures, leaner operation may come at a tradeoff regarding reduction of overall pressure. In this case, the same stratification manipulation could meet a secondary goal of producing higher levels of pressure using the same amount of overall fuel.

2. NUMERICAL SIMULATION

2.1. Ajax E-565 Case Setup Parameters and Implementation

The following sections detail the creation of the Ajax E-565 CFD simulation, as well as rationale for why certain parameters were chosen over others. Extensively modified for this work, the basis of this model was originally created as a part of Dr. Alireza Mashayekh's study of conjugate heat transfer in the E-565. He successfully simulated the E-565 in its default configuration, using Fluid Structure Interaction (FSI) to model the reed valves used to control the AFR within the engine's stuffing box [11]. This work sought to simulate the same engine after converting to the use of a hydraulic, low pressure direct injection system and simplifying Dr. Mashayekh's original 58 part model to reduce overall simulation complexity.

2.1.1. Geometry Preparation and Modifications

The original CFD model with reed valves was created using CAD models provided by then GE Oil & Gas. Extensive geometry cleanup was performed, then the fluid-bearing surfaces necessary for the simulation were extracted and are shown below in Figure 2.1. The reed components are depicted in light blue, while the air intake and fuel intake are shown in white and brown, respectively. The stuffing box is cream, the intake manifold between the chamber and stuffing box is purple, and the chamber liner is orange. The final three parts, the exhaust manifold, cylinder head, and spark plug, are shown in green, blue, and brown. The final CAD file was then exported as an STL file for use in CONVERGE Studio.

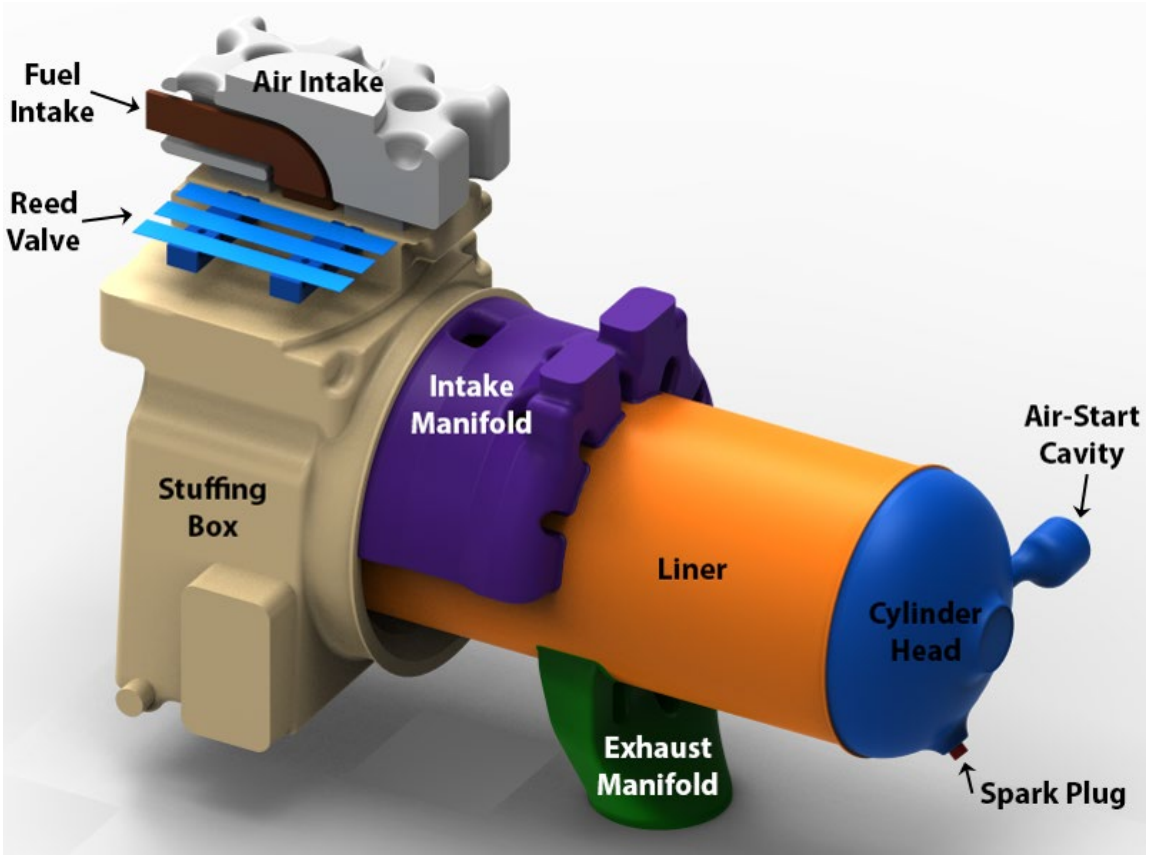

Figure 2.1: The finished geometry for the CFD simulation from Dr. Mashayekh's dissertation. The reed valves were shown in cut view to show the valve strips and fuel intake. Reprinted from [11].

In order to reduce the complexity of the geometry and overall size of the simulation, the existing model was first stripped down to the most essential components and the reed valve componentry removed. With the introduction of the direct injection (DI) system, the stuffing box no longer needed to serve as geometry influencing the fresh fuel and air charge. It was removed for later replacement with a simpler, but still effective, representative volume. These initial changes resulted in the reduction of the number of parts from 58 down to the seven shown below in Figure 2.2. In addition, the cylinder head was also removed to be replaced with the DI geometry, which had been notably removed during Dr. Mashayekh's

study, as evidenced by the flattened solid top center of the original cylinder head. This part was replaced and will be discussed later in this section. The remaining parts at this stage were the piston shown in purple, the intake manifold in yellow, the chamber liner in blue, and the exhaust manifold in green.

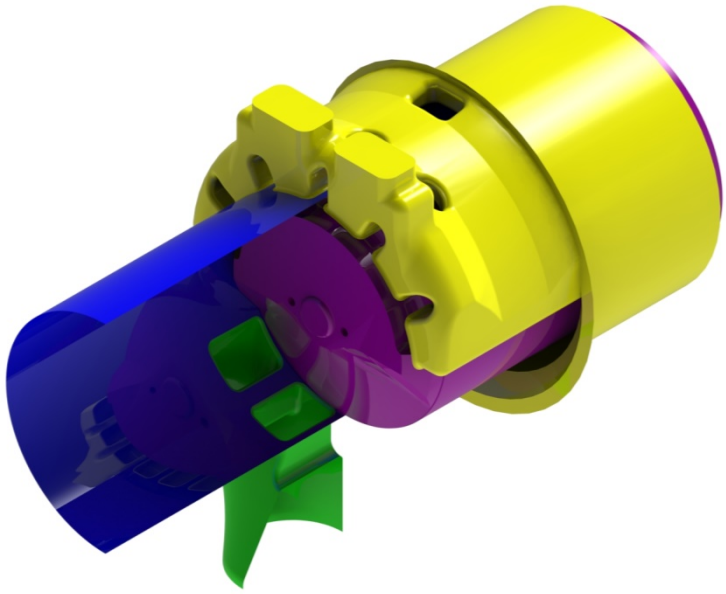

Figure 2.2: The geometry stripped down to the most essential components retained from the original model by Dr. Mashayekh, including the piston, intake and exhaust manifolds, and liner. Shown with the liner cut open to show the piston crown and port surfaces.

While still necessary for providing fresh air to the main chamber, the stuffing box geometry did not need to be rendered as a complex geometry in order to provide accurate results. Early test runs removed the stuffing box completely in favor of inlet boundaries immediately at the edge of the air intake manifold, but this method produced unrealistic pressure waves. As a result, it was instead replaced by simple cylindrical geometry of comparable size in order to use experimentally obtained pressure data as stuffing box

boundary conditions. The overall size was mitigated by the ability to use a very coarse mesh in the region. Further details of the mesh logic, and why it can be coarsened in the stuffing box region, will be discussed in section 2.1.11 Base Grid and Grid Control Methods. The final stuffing box replacement geometry is shown below in Figure 2.3 in red.

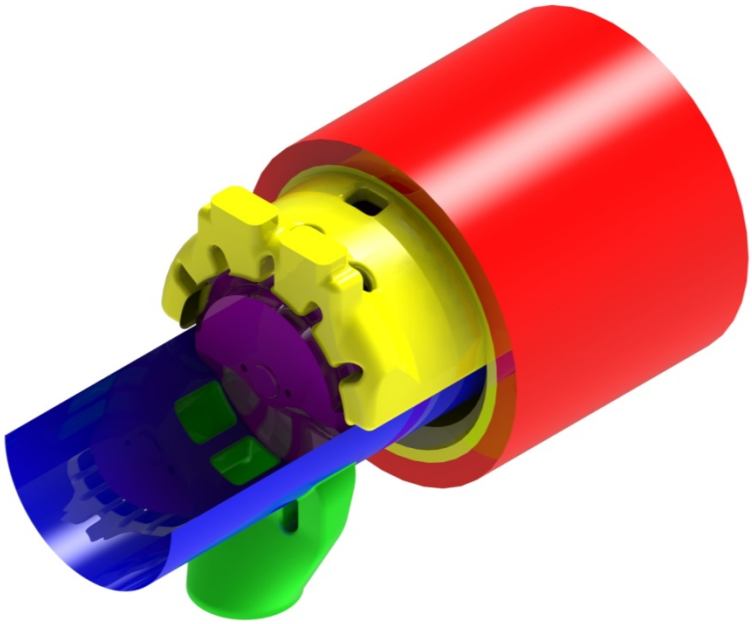

Figure 2.3: Progression of the simplified stuffing box geometry to the early DI modification to the CFD model.

For direct comparison, Figure 2.4 below shows the replacement representation of the stuffing box in silver on the left against the original and accurate geometry for the stuffing box, shown on the right in red. Triangle edges were also shown to demonstrate the relative complexity of the two parts. The silver stuffing box for the DI CFD model requires approximately 200 triangles to render representatively, while the original stuffing box required more than 90,000 and was among the most complex parts. Savings from the

stuffing box change in regards to cell counts in the mesh will be discussed further in section 2.1.11 Base Grid and Grid Control Methods.

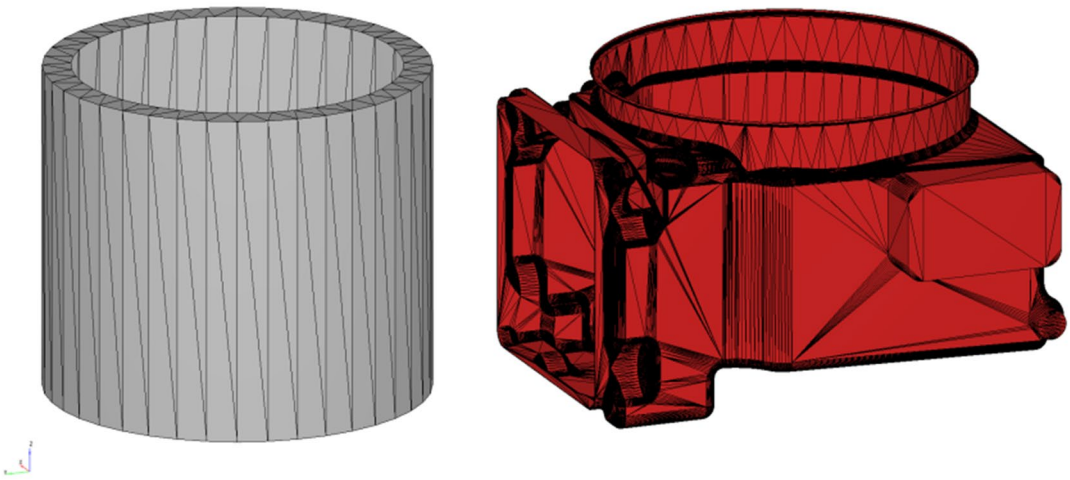

Figure 2.4: Comparison of the representative volume of the stuffing box (left, silver) used in the new DI CFD model against the original stuffing box geometry (right, red), including the relative complexity of triangulation.

The next focus was to incorporate the DI system, parasolid files for which were graciously provided by Baker Hughes, a GE Company. The identical system to the one installed on the AERL test cell E-565 was not available, but a comparable geometry was provided. The parts were imported into SolidWorks and then assembled in the proper orientation. The final components are shown below in Figure 2.5. Rather than just extracting surfaces from individual parts, the assembly was completed first to ensure that any necessary channels or fluid bearing surfaces were not neglected or missing, as well as provide a full geometry version of the model, if needed for analysis later.

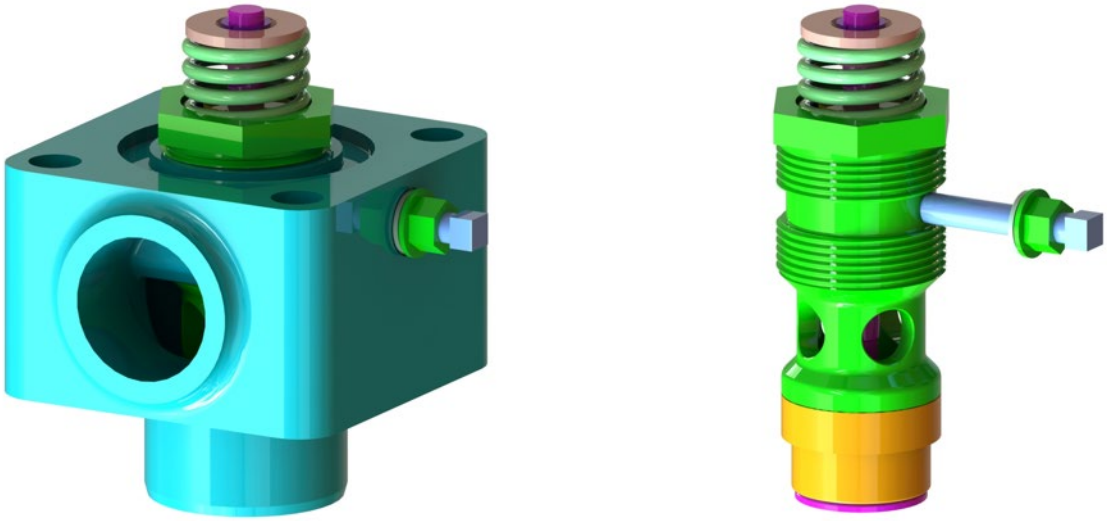

Figure 2.5: The comparable DI valve and housing geometry provided by Baker Hughes, a GE Company and assembled (left). The valve componentry is shown on the right with the external housing (blue) removed for clarity.

In order to properly "install" the valve housing virtually the cylinder head center needed to be reopened to allow for placement of the DI componentry. In the original simulation referenced prior in Figure 2.1, the coolant pathways had already been removed to only retain the interior chamber surface of the head and patch the hole. The full cylinder head, with the coolant pathways still intact, is shown below in Figure 2.6. The left side of the figure shows the mounting for the DI system housing, while the coolant pathways throughout the head, as well as the inlet channels between bolts, are shown on the right side of Figure 2.6. Also depicted on the right, the central hole is the injection valve mounting location, the left hole is the air start cavity, and the bottom hole is the spark plug location. In order to insure the DI parts from Figure 2.5 were placed correctly relative to the rest of the chamber and engine, the final parts were assembled prior to extracting the desired surfaces and are shown in Figure 2.7. Combining the parts before surface extraction also allowed for

close inspection to remove any parts that were unneeded in terms of maintaining the proper flows within the simulation.

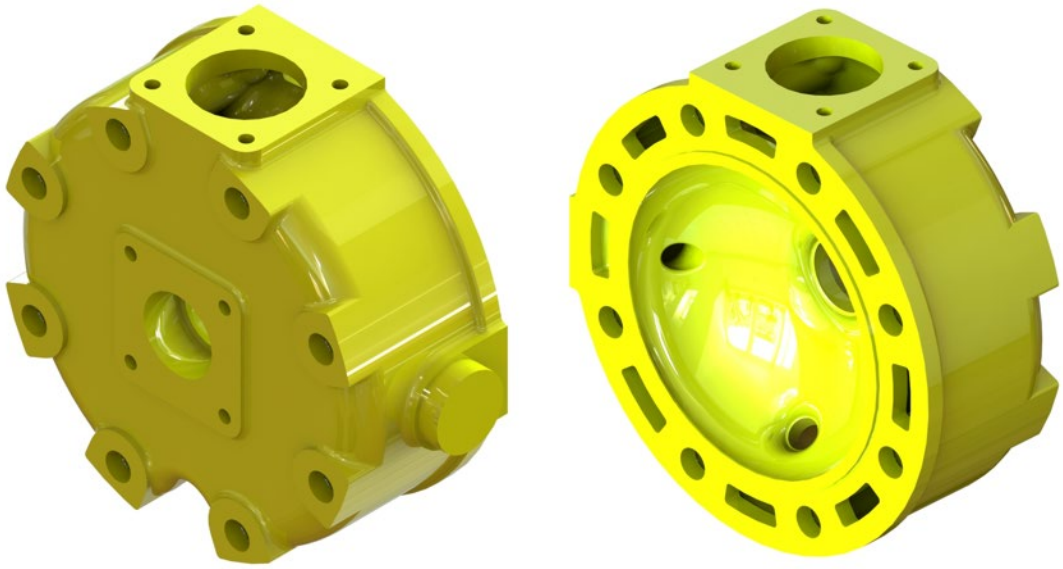

Figure 2.6: The cylinder head top and bottom before surface extraction.

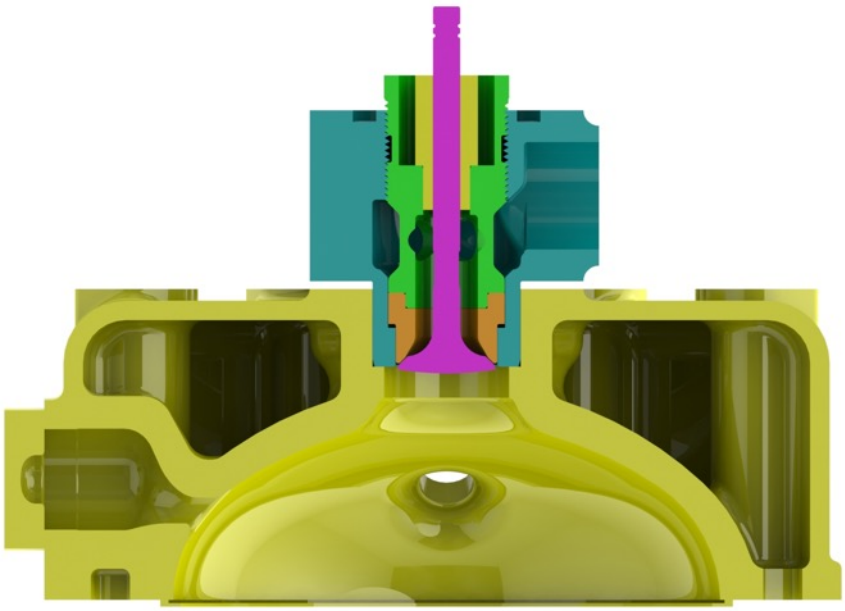

Figure 2.7: The total assembly of the DI geometry and full cylinder head prior to surface extraction. Note the air start cavity to the far left of the cylinder head and the dimple into the page for the spark plug.

The geometry was checked for any gaps that would create errors within the CFD simulation. Being a solid piece, the head was free from any discontinuities, but multiple part interfaces and tolerances within the DI valve housing led to spots that would allow unrealistic fluid flow. To mitigate this, a number of small rings or slivers were created to fill in gaps. After ensuring there were no breaks in the geometry, the surfaces were extracted, as shown in Figure 2.8. These final parts included the surface of the MCC head, including the air start cavity and spark plug hole, the interior piping for the DI fuel supply, and the DI valve itself.

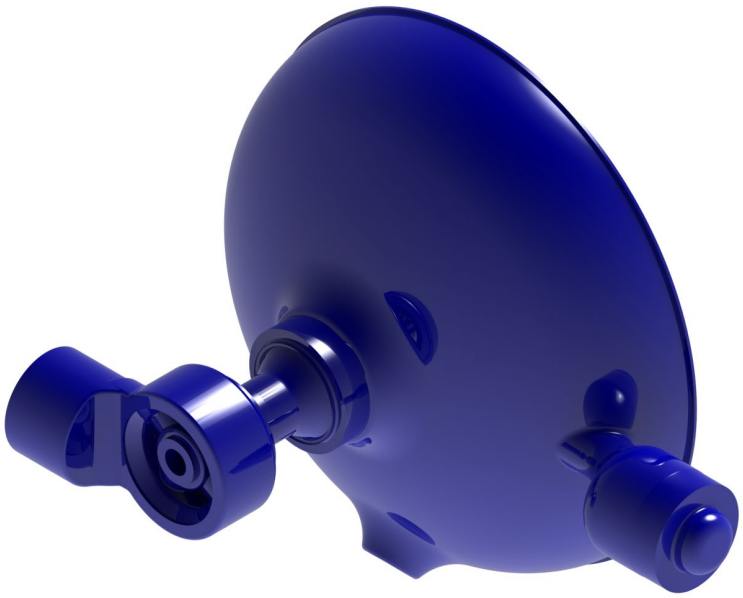

Figure 2.8: The surfaces extracted to form the cylinder head and associated DI system geometry.

After finalization of the recreated head and DI system, the combined assembly was placed back onto the full E-565 geometry and modified stuffing box previously displayed in Figure 2.3. The spark plug was added back to fill the hole in the head, and the DI fuel intake

was extended to include additional runner piping. This was a pre-emptive modification to avoid the pressure fluctuations seen with the reduction in size of the stuffing box geometry. The final completed domain for this study is shown below, with all parts, in Figure 2.9. The cylinder head is shown in light blue, the spark plug at the bottom left in light purple, the fuel injection housing in white, and the direct injection valve in maroon. Parts shown previously include the red stuffing box volume, yellow intake manifold, dark blue liner, and green exhaust manifold.

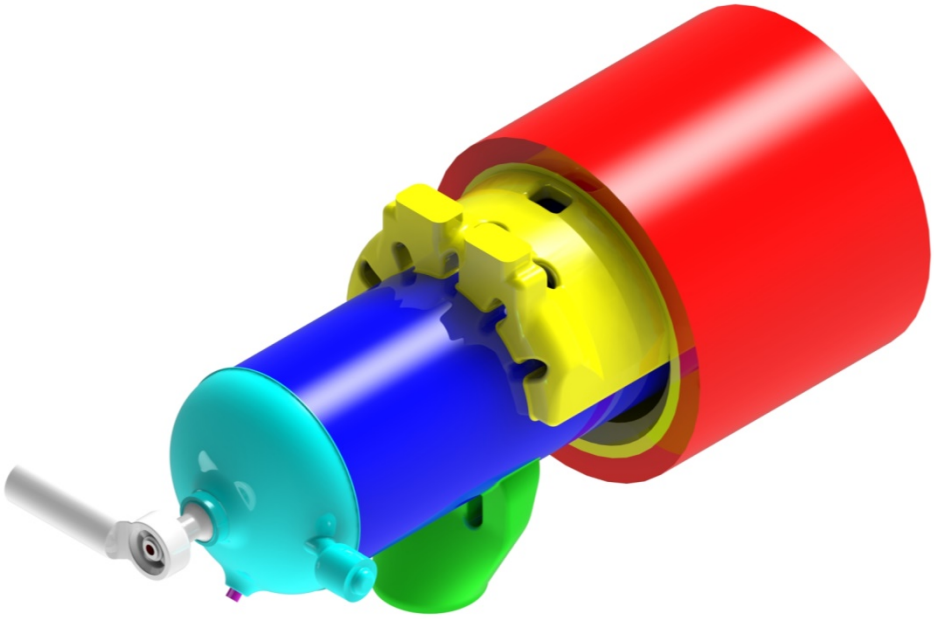

Figure 2.9: The complete Ajax E-565 geometry utilized for this study.

The entire assembly shown in Figure 2.9 was then exported as a single *.stl surface file for use within CONVERGE Studio and later split back into individual boundaries within Studio. Once imported into Studio, the geometry was checked again, and any lingering imperfections were painstakingly corrected to ensure any flaws were eliminated.

Figure 2.10: A cutaway view to show the interior of the added DI system geometry near the cylinder head, specifically the white housing and the maroon valve. The spark plug is purple and shown for relativity.

Once the surface was sufficiently cleaned, the triangles of the geometry were flagged into boundaries, first according to physical part similar to that seen in Figure 2.9, then subdivided as needed for numerical purposes to be discussed in the following sections, such as to resolve mass flow rates or species at specific locations of interest. Table 2.1 below summarizes the final geometric parameters input into Converge for a crank angle-based IC engine simulation.

Table 2.1: Summary of final Converge geometric quantities

Physical Parameter	Value
Cylinder bore	0.22m
Stroke	0.254m
Connecting rod length	0.508m
Crank offset	0.0
Swirl ratio	0.0
Swirl profile	3.11
Crank speed	525.0 RPM (High speed)

2.1.2. Configuration of Regions

After configuring the geometry as shown previously in Figure 2.9, the solution domain was split into the following four regions:

1. Intake air: This region included the stuffing box, the under surfaces of the piston exposed to the stuffing box, and the intake manifold from the stuffing box up to the interface of the intake ports and cylinder liner.
2. Intake gas: A region extending from the angle of the direct injection fuel valve up to the edge of the solution domain at the end of the added fuel runner geometry. The bottom of the fuel valve, being exposed to the main combustion chamber rather than the fuel intake, was included in the chamber region.
3. Chamber: This region includes the volume of the main combustion chamber. It notably includes the cylinder head, bottom of the fuel valve, piston crown, and liner.
4. Exhaust: This region extends from the interface of the liner and exhaust ports to the end of the solution domain. This is primarily only the exhaust manifold.

2.1.3. Initial Conditions and Time Parameters

Each of the four individual regions of the previous sections requires inputs of thermodynamic parameters, such as pressure, temperature, and species concentrations, to serve as initialization values in the simulation. The desired start time for the simulation is just before EPO, where scavenging and gas exchange processes have not yet occurred. This

also allows for starting the simulation with more easily defined initial species concentrations, to be discussed in the following sections.

Initial Pressure Conditions

All initial pressure values were set based upon experimental data for the associated spark timing, with exception of the fuel intake pressure upstream of the direct injection valve. The physical engine is instrumented with a manual read analog pressure gauge upstream of the fuel governor, which tended to read 8-10psi (approx. 55-70kPa) gauge during the experimental collections used for validation of this numerical study. Understanding that the fuel pressure downstream of the governor would experience pressure losses, a number of various pressures were iteratively tested, and the simulation fuel pressure was set to 142kPa absolute in all subsequent simulations.

Initial cylinder pressure was set by taking an average of experimental pressure data across 200 measured cycles in order to eliminate the effect of cycle to cycle variations, then recording the corresponding pressure value at EPO. This process was carried out to produce initial chamber pressure values for nominal spark timing, 5º retarded spark timing, and 10º advanced spark timing.

Initial Temperature Conditions

The fuel and air intake regions were set to ambient temperature on the experimental test day, then raised slightly to 350K to account for heating due to proximity to the combustion chamber. Initial temperature for the combustion chamber was estimated as 1700K. The initial temperature of the exhaust region was set based upon experimentally

measured exhaust gas temperatures for the spark timing case desired: nominal (NS), retarded (RS), or advanced (AS).

Initial Species Concentrations

Experimental data suggests that the instrumented E565 in the AERL tends to run at a lean equivalence ratio. With the simulation starting at EPO, both the chamber and the exhaust region were initialized to mixtures consisting of the perfect products of a complete combustion reaction with an ER of 0.81. The intake gas species were set according to a chromatograph report from local supplier ATMOS Energy in October of 2019 near the original experimental testing window [12]. The intake air region was assumed to be pure air, and a summary of the overall species is shown below in Table 2.2.

Table 2.2: Region-based species concentrations across all simulations.

Region	Species	Mass Fraction
Intake air	O_2	0.2300
	N_2	0.7700
Exhaust and Chamber	O_2	0.0422
	N_2	0.7315
	CO_2	0.1265
	H_2O	0.0998
Intake gas	CH_4	0.9034
	C_2H_6	0.0392
	C_3H_8	0.0035
	CO_2	0.0215
	N_2	0.0324

Time Parameters

All time parameters were set within Converge Studio default values. The time-step selection was the variable time-step algorithm, and the initial time-step was set to 1e-07s.

The minimum time step was 1e-08s, and the maximum step was 1e-04s. All CFL stability limits were left with recommended values.

2.1.4. Gas Simulation and Run Parameters

For this simulation, Converge's solver was set to transient mode with a crank angle-based engine temporal type. The transient option is necessary for an engine simulation, and the temporal type allows for calculations on a crank angle basis rather than time basis. Full hydrodynamic was selected for the simulation mode to ensure that Converge includes all transport and combustion equations. Similarly, the gas flow solver was set to compressible, as the high temperature and pressure levels in combustion engines cause fluctuations in gas densities.

In order to be able to couple pressure, density, and temperature for the compressible solver, the Redlich-Kwong (RK) equation of state was selected for the gas simulation. Compared to the options of ideal gas, Redlich-Kwong-Soave, or Peng-Robinson, standard RK is recommended when accounting for non-ideal gas parameters at the high pressures and temperatures in an engine chamber [13].

Presented in general form, the RK equation takes the form of the following (2.1):

$$P = \frac{RT}{v - b} - \frac{a}{v^2 + ubv + wb^2} \tag{2.1}$$

The values of the coefficients when implementing the standard RK equation of state are shown below in Table 2.3, where T_c, v_c, and P_c represent the critical temperature, critical volume, and critical pressure, respectively. In general, α represents the forces of attraction between molecules, and β represents molecule volume [13]. Default values of a critical temperature of 133K and critical pressure of 3.77e+06 Pa were used.

Table 2.3: Expanding coefficients for Redlich-Kwong general equation of state

Coefficient	Equations	Values
$\boldsymbol{u}$	-	$\boldsymbol{u = 1}$
$\boldsymbol{w}$	-	$\boldsymbol{w = 0}$
$\boldsymbol{b}$	$\boldsymbol{\beta_{rk} v_c}$	$\boldsymbol{\beta_{rk} = 0.08664}$ $v_c = \frac{RT_c}{p_c}$
$\boldsymbol{a}$	$\boldsymbol{\alpha_{rk} \frac{p_c v_c^2}{\sqrt{T_r}}}$	$\boldsymbol{\alpha_{rk} = 0.42748}$

2.1.5. Reaction Mechanism and Species

The reaction mechanism stores a list of all the gaseous elements present within the simulation, as well as all of the species. In this case, the SAGE detailed chemical kinetics solver was used, so the reaction file also needed to include reaction specifications [14]. For this, the heavily tested and well-validated GRI-Mech 3.0 mechanism, including its reaction, thermochemical, and transport mechanisms, was selected. Optimized for modeling natural gas combustion and including NO formation and detailed reburn chemistry, GRI-Mech 3.0 contains 325 reactions and 53 different species composed of five elements: oxygen, hydrogen, carbon, nitrogen, and argon [15].

2.1.6. Boundary Intersection Handling and Seals

Converge simulations are built upon triangulation of the geometry and a massive collection of vertices in space. In order for the case to run properly, the domain needs to consist of fluid bearing surfaces and be checked for any number of geometry-related errors, such as overlapping triangles, sliver triangles (triangles of essentially zero-area), and most commonly, surface intersections [14].

Surface intersections in this work were handled during the geometry preparation phase as part STLs were assembled into the final geometry presented earlier. Primarily, this consisted of making sure the parts interfaced properly. For example, when creating the cylinder liner, the liner was first created as a pure cylinder, then the ports were cut normal through the side using the exact profile of the intake and exhaust manifold. This ensured a perfect mating at the interface without gaps to allow undesirable flow and removed the possibility of any realistic tolerances present in the original CAD files creating imperfections.

In order to prevent sliver and overlapping triangles, moving surfaces, such as the piston, have to be checked to make sure that adjacent boundaries will remain intact throughout the entire simulation, not just at a single instant in time. For the two-stroke engine of this study, the piston must cross both the intake and exhaust ports in a single stroke, creating a situation where the triangles of the piston invert upon crossing the ports [16]. This breaks the boundary and will not allow the simulation to continue.

Additionally, the piston has a second problem, as to avoid intersections, the piston outer edge must be slightly smaller in diameter than the cylinder liner. While this prevents any intersection errors, it can introduce flow errors, as the slight discrepancy in diameters opens two sets of gaps: one between the piston skirt and liner than allows flow straight from the combustion cylinder into the stuffing box, and a second gap that allows flow from the ports into the space between the liner wall and the piston skirt. Converge includes a sealing feature to address both of these issues.

Sealing allows for control when controlling flow into different regions. It selectively allows flow between different parts of the same region. It also has the ability to be placed at specific locations, which was integral to implementing seals at the ports and top of the piston. The seal effectively allows Converge to remove the gap between the piston skirt and liner to prevent flow and neglect it from the main cylinder volume during calculations. Four seals were implemented, as shown below in Figure 2.11. This involved one seal at the bottom surface of the piston skirt out toward the liner, one seal at the bottom edge of the piston crown to the cylinder liner, and one seat of seals each for the intake and exhaust ports. With these seals in place, flow was prevented between the combustion chamber and the stuffing box, as well as prevented between the ports and the piston skirt.

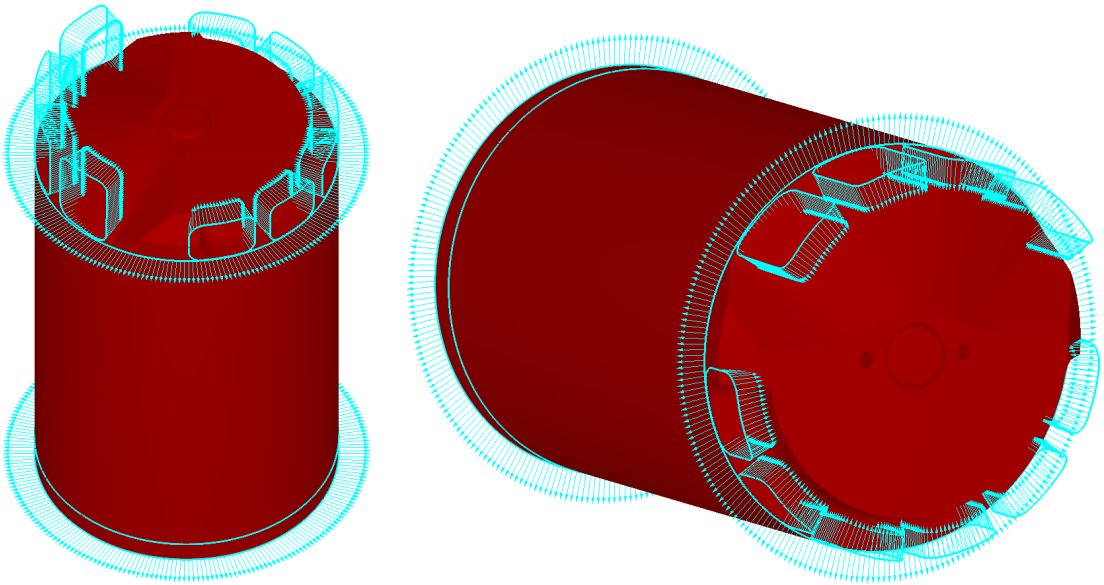

Figure 2.11: Four sets of seals configured between the piston and the cylinder ports and liner to prevent undesirable flow.

2.1.7. Boundary Conditions

Converge requires that all walls need to belong to a boundary and that all inlets need to have defined parameters. The following sections will detail the boundary conditions, as well as the events within the simulation.

Stationary Boundary Types

Almost all physical sections of the engine were set to stationary wall types with defined temperatures based on either best guesses, experimentally obtained data, or by referencing Dr. Mashayekh's original conjugate heat transfer study [11]. All boundaries, with exception of mass flow boundaries, were set to law-of-wall as the velocity boundary condition. Of note, each boundary must be assigned to one of the four defined regions to which it interacts with. The stationary walls, along with their wall temperatures and associated regions, are summarized below in Table 2.4.

The temperatures of the exhaust manifold were changed according to whether the spark timing was nominal (NS), retarded by five degrees (RS), or advanced by ten degrees (AS). This was completed by estimating the wall temperature with the average exhaust gas temperature during the exhaust process.

Table 2.4: Stationary boundaries with wall temperatures and associated regions.

Stationary Boundary	Region	Wall Temperature (K)
Intake manifold	Intake air	350
Exhaust manifold	Exhaust air	750 (NS), 809 (RS), 701 (AS)
Cylinder liner	Chamber	450
Spark plug	Chamber	800
Cylinder head	Chamber	610
Fuel valve housing	Intake gas	350

The intake manifold and fuel valve housings were intended to be slightly higher than ambient temperature to account for heating after reaching steady state, and the exhaust manifold temperatures were approximate guesses obtained by examining experimentally determined exhaust gas temperatures. Temperatures for the cylinder liner, spark plug, and cylinder head were assumed to be higher due to direct interaction with the combustion event.

Moving Boundary Types

While the above boundaries are stationary, the following piston and direct injection valve are not. The piston moves along a user-defined path, shown in Figure 2.12. The moving boundaries also require region and wall temperature assignment, shown in Table 2.5. The motion profile for the direct injection valve will be discussed in great detail in section 2.2 Direct Injection Valve Model Implementation.

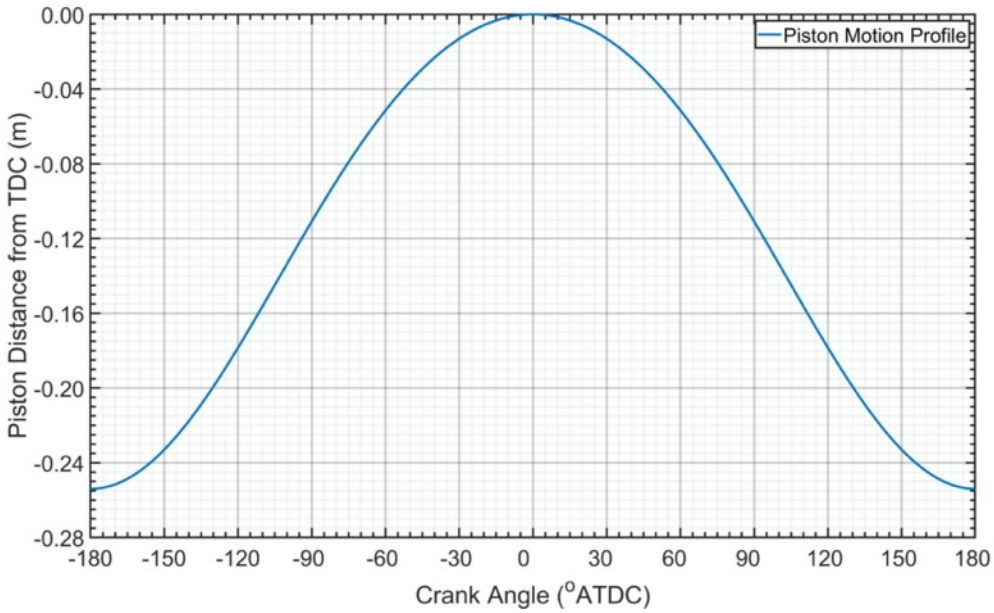

Figure 2.12: Piston distance from TDC against crank angle.

Table 2.5: Moving boundaries with wall temperatures and associated regions

Moving Boundary	Region	Wall Temperature
Piston crown	Chamber	810
Piston skirt	Dependent on seals	450
Piston bottom surface	Intake air	350
Fuel valve bottom	Chamber	610
Fuel valve angle stem	Intake gas	610
Fuel valve stem	Intake gas	350

Mass Flow Boundaries

Two inflow boundaries were implemented in this model along with one outflow boundary. One inflow boundary was placed as the stuffing box, and a second was placed at the beginning of the fuel intake runner. An outflow boundary was placed at the edge of the exhaust manifold. The species concentrations of the air intake inflow boundary and the fuel intake inflow boundary were set identically to the parameters specified as the initial region conditions for intake air and intake fuel, respectively. The species concentrations were summarized previously in Table 2.2, and the temperatures at both inflow boundaries were

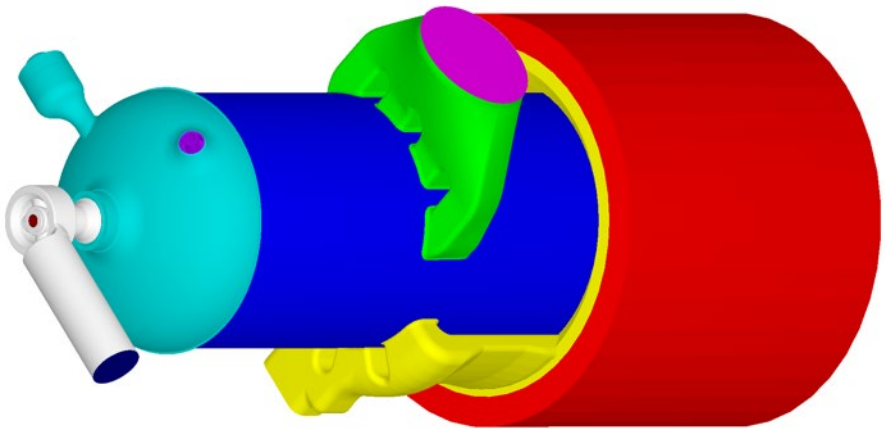

Figure 2.13: The fuel and air mass inflow boundaries with the exhaust mass outflow boundary.

set to 313K. Figure 2.13 depicts the fuel inflow boundary at the bottom left in navy, the stuffing box air inflow boundary in red on the right, and the exhaust outflow boundary in pink at top center.

Pressure Boundary Conditions

All inflow and outflow boundaries were configured as specified value Dirichlet conditions. In the case of the fuel inflow boundary, pressure was set to a constant 142kPa total pressure across all three spark timings, NS, RS, and AS. Both the air inflow and exhaust outflow boundaries were configured according to crank-angle resolved experimental datasets. These were produced as described in section 2.1.3 Initial Conditions and Time Parameters, where 200 individual cycles were averaged together to reduce cycle to cycle variability and used as the boundary conditions. Figure 2.14 and Figure 2.15 show the air manifold and exhaust manifold boundary averages overlaid on the individual experimental cycle traces for the nominal spark timing case. The boundaries for the RS and AS cases are similarly shown in Figure 2.16 to Figure 2.19.

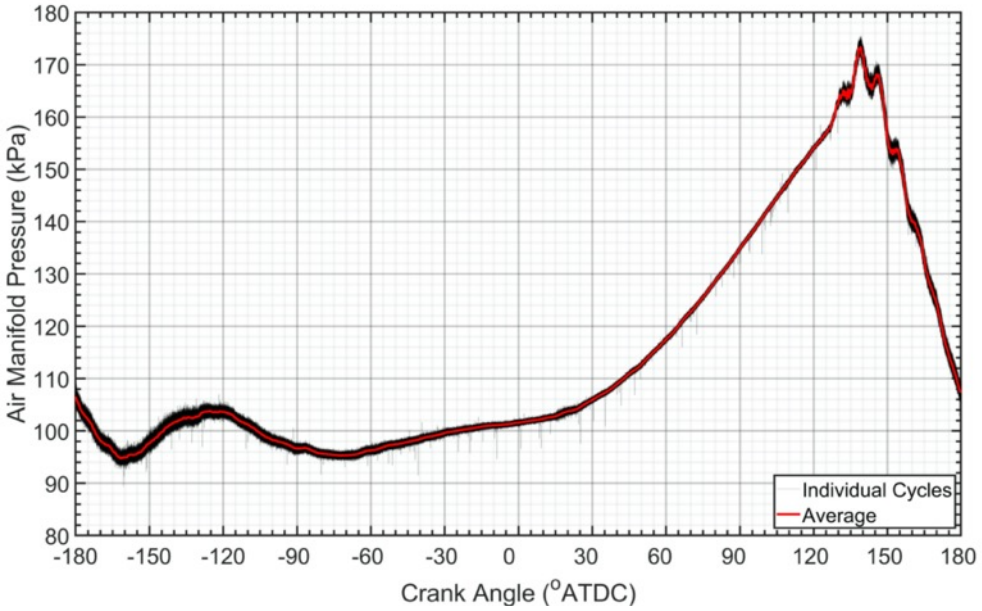

Figure 2.14: Experimental boundary conditions for the air manifold pressures in the nominal spark timing simulation.

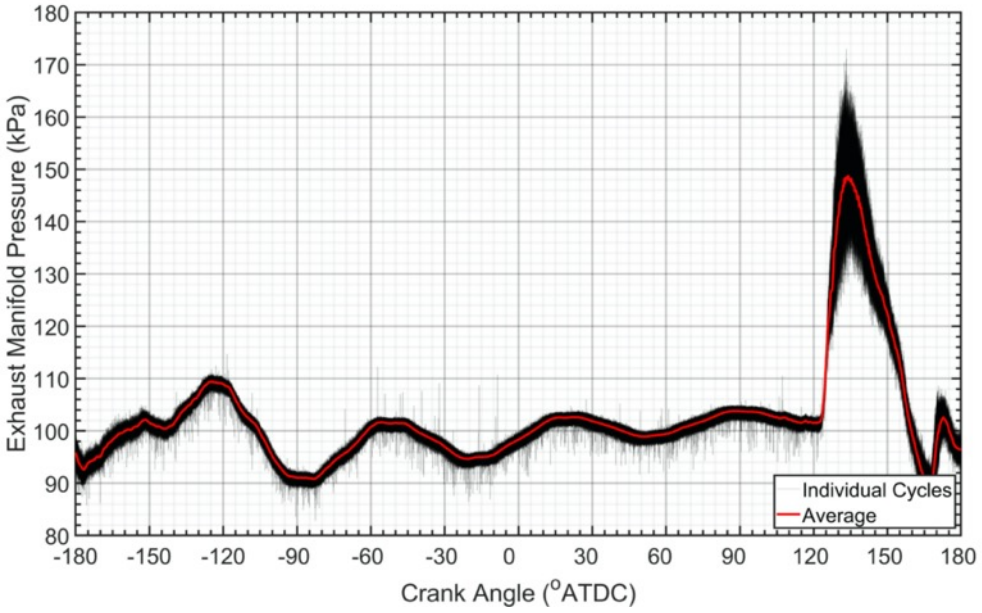

Figure 2.15: Experimental boundary conditions for the exhaust manifold pressures in the nominal spark timing simulation.

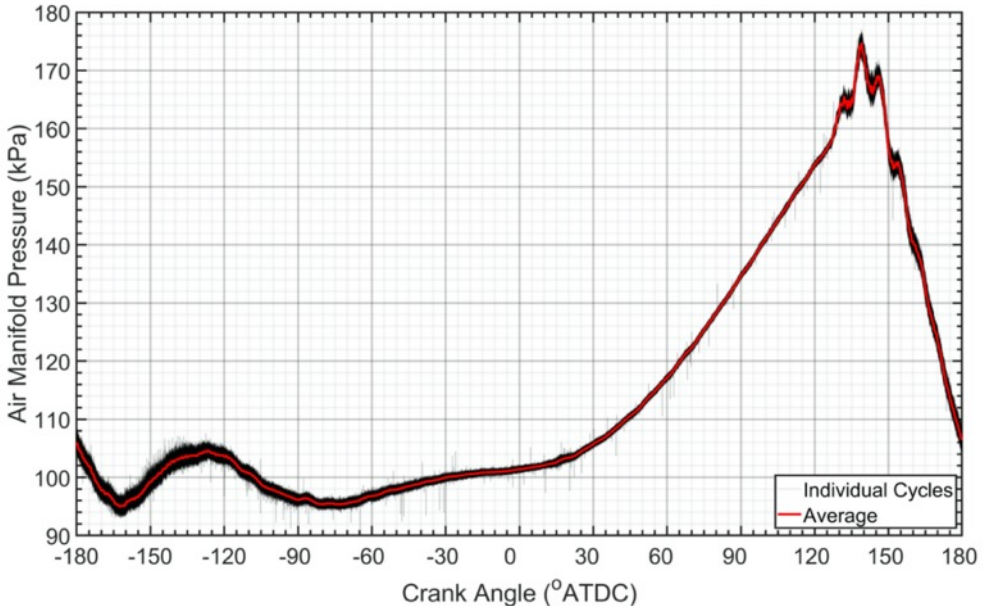

Figure 2.16: Experimental boundary conditions for the intake manifold pressures in the retarded spark timing simulation.

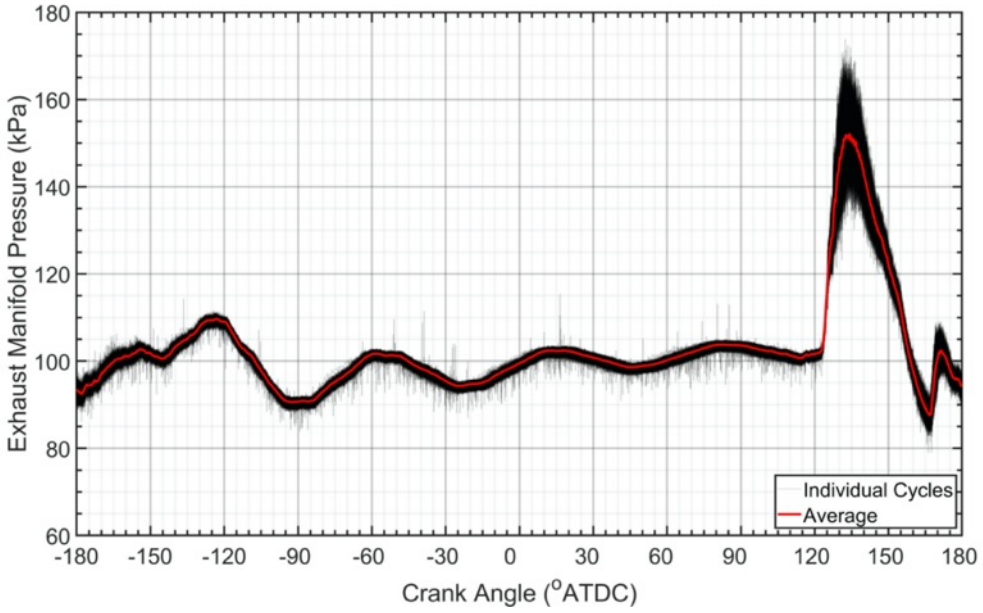

Figure 2.17: Experimental boundary conditions for the exhaust manifold pressures in the retarded spark timing simulation.

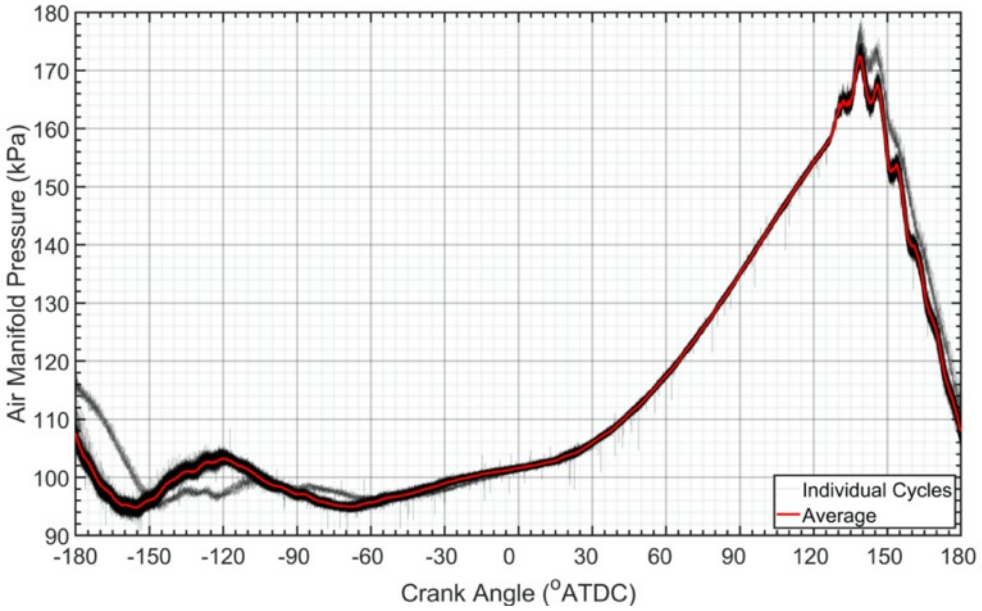

Figure 2.18: Experimental boundary conditions for the intake manifold pressures in the advanced spark timing simulation.

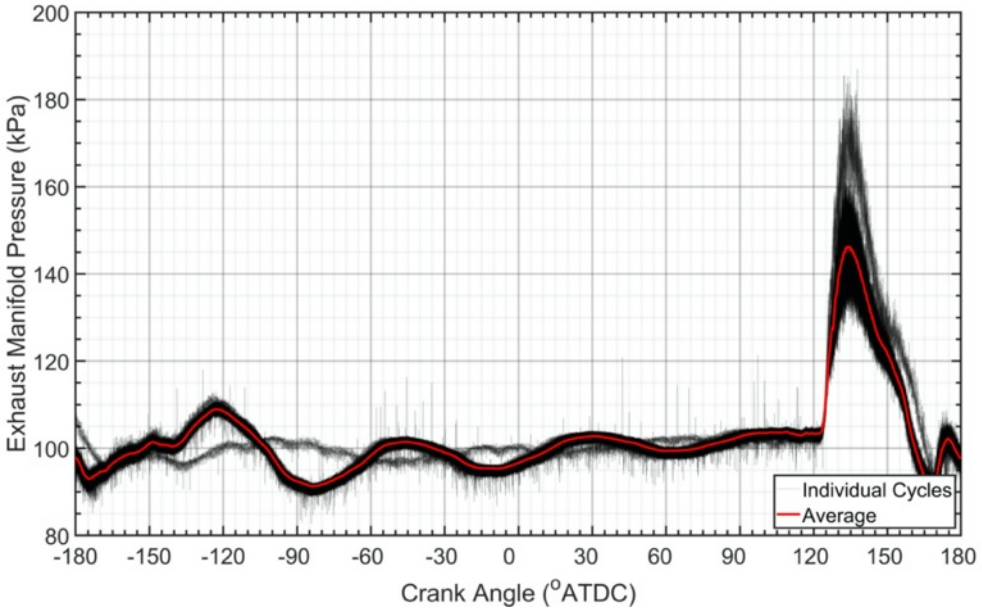

Figure 2.19: Experimental boundary conditions for the exhaust manifold pressures in the advanced spark timing simulation.

2.1.8. Combustion Modeling

Combustion modeling was performed by activating the SAGE detailed chemistry solver for a period beginning approximately 3 degrees before spark lasting until EPO. This corresponded to CAD start times of 15°BTDC (NS), 10°BTDC (RS), and 25°BTDC (AS), with an ending time of 120°ATDC for all three cases. Combustion was activated only in the chamber region for this period.

SAGE parameters were left with Converge defaults. The analytical Jacobian was selected, as according to the Converge manual, this can accelerate the SAGE solution [14]. The solver was set to constant volume coupled with CVODES with dense solver, which is recommended for less than 100 species. Adaptive zoning was also activated. This is a method that increases the speed of combustion calculations by grouping together similar cells and solving for chemistry once rather than on a per cell basis [14].

2.1.9. Source Modeling

In order to accurately simulate a spark event, two spherical source volumes were placed at the edges of the plug electrodes, as shown in Figure 2.20. Source volume one models spark breakdown, which occurs at the beginning of the event for a shorter duration, and source volume two models the arc and glow processes [3]. The arc and glow events were combined because they occur on the same time scale [17]. Source one is active between spark timing start at 348.8CAD and 348.9CAD (nominal timing), while source two also begins at 348.8CAD but persists longer until 349.5CAD (nominal timing). For the RS case, both sources were shifted five degrees to start at 353.8CAD, and in the AS case, both sources were shifted ten degrees earlier to 338.8CAD. All sources were set to produce 0.15J

of energy during their respective durations, and maximum temperatures were set to 50,000K.

Figure 2.20: The spark plug in purple and the initial placement of the source volumes at the electrodes in bright blue.

Although centered in the same location, spark volume one was given a radius of 0.5mm, while spark two was given a larger radius of 0.8mm. The sources were given no initial velocity but were allowed to move with the flow up to a maximum displacement of 1mm. After reaching the maximum displacement, the source location resets to the original location at the electrodes. The temperature rise in the chamber associated with the spark event, for the nominal timing case timing, is shown below in Figure 2.21. This event supplies the energy necessary to initiate the combustion process and flame propagation.

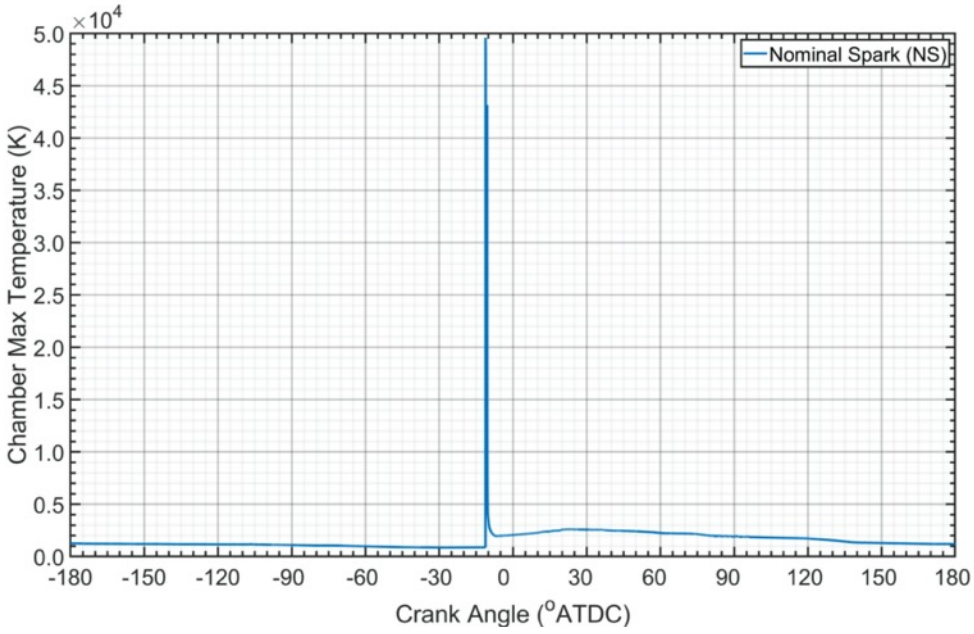

Figure 2.21: Maximum temperature in the main combustion chamber as a result of the spark event with nominal spark timing.

2.1.10. Turbulence Modeling

CFD simulations require turbulence models in order to obtain accurate results. Turbulence has a great impact on a number of parameters, but most notably the rate of mixing of momentum, species, and energy. Turbulent eddies exist on a wide variety of length scales, and in order to resolve these, the overall size of the grid in the simulation must be sufficiently small. However, this can be incredibly computationally expensive to calculate such a refined grid, and in many cases, is too expensive to be feasible. To make more efficient use of computational resources, simulations make use of more practical turbulence models [13]. In this case, Reynolds-Averaged Navier-Stokes (RANS) re-normalization group (RNG) k-ε modeling was activated, and law-of-the-wall was used with all boundaries for velocity and temperature.

RANS models are general turbulence models that establish a two-equation model to break flow variables into an ensemble mean term and a fluctuating term. The RNG k-ε is commonly used to account for the aforementioned effects of turbulence at small scales of motion [14], and the specific formations involved in the Converge CFD implementation may be found in the Converge 3.0 Manual [13]. All parameters were implemented with the recommended model values within Converge Studio.

2.1.11. Base Grid and Grid Control Methods

One of the major advantages to Converge CFD compared to other codes is the improvement associated with runtime meshing. Traditionally, manual grid generation tends to be a major time sink in the scope of a CFD project and can severely limit how detailed domain geometries might be. Converge mitigates this by automatically generating the simulation grid at runtime across each time-step. This is done by utilizing a modified cut-cell Cartesian grid of perfectly orthogonal cells, details of which may be found in the Converge manual [13]. Ultimately, it simplifies the intersections of boundaries, generates the grid, moves surfaces, and then applies any refinement techniques.

The base grid specifies the default cell size within the domain. During his previous work on the E-565, Dr. Mashayekh tested various base grid sizes and selected 7.5mm as a balance between solution accuracy and computation time [11]. After the simplification and rebuilding of the model with the DI system, new base grid sizes were tested. Coarser grids still failed to capture proper effects and were not validated, but finer grids caused significant slowdowns, particularly during the initial flows even before activation of the combustion solver. For this reason, the 7.5mm base grid was maintained as a safe computational

compromise, and a combination of fixed embedding and adaptive mesh refinement were used to improve the solution accuracy.

Fixed Embedding

In order to improve the solution accuracy due to the relatively large base grid size, fixed embedding was applied to critical. Fixed embedding (FE) is an algorithmic method that can refine the grid in specific areas at user-defined times. This can be incredibly useful to improve resolution around events of interest, such as near the spark plug at the start of combustion or next to valves during injection. The additional resolution can be important to ensure the simulation is adequately resolving effects in those areas. According to the Converge manual, FE refines the grid at a specified location according to equation (2.2) [13]. Each single cell is only allowed to be adjacent with two embedded cells to maintain Converge's two-to-one connectivity ratio, and if embedding is more than a difference of one level, the solver will automatically add intermediate scales.

$$embedded\ size\ = base\_grid/2^{embed\_scale} \tag{2.2}$$

Three FE areas were implemented in the simulation, according to areas that were expected to have impact in the overall accuracy of the solution:

1) Spark plug: Level 4 embedding (0.47mm grid) was applied in a spherical shape around the spark plug electrodes beginning 3° before spark timing extending until 22° after spark timing. The overall timing of the event was shifted according to the NS case, RS case, or AS case. This was activated earlier than spark in order to accurately resolve the surrounding field before any energy input and left active to capture the beginning of combustion and flame propagation.

2) Chamber: Level 3 embedding (0.94mm grid) was applied to the entire combustion chamber, including walls, beginning 2° before spark and lasting until 400°. The start time was shifted according to NS, RS, or AS, similar to the spark plug embedding. This was intended to improve the solution resolution compared to base grid during the combustion event.
3) Direct injection valve: Level 3 embedding (0.94mm grid) was applied in a spherical shape centered around the direct injection valve seat, and was activated between 217°ATDC and 272°ATDC. These were implemented with sufficient leeway such that changes to valve timings would not necessitate changes to the embedding timing and will be described in greater detail in the following section 2.3 Power and Fuel Study Setup. Table 2.6 summarizes the FE levels used and in what areas.

Table 2.6: Summary of applied fixed embedding.

Area of Interest	Embed Level	Start CAD	End CAD
Spark plug	4	3° before spark	22° after spark
Chamber	3	2° before spark	51° after spark
Injection valve	3	217° BTDC	272° BTDC

Adaptive Mesh Refinement

Adaptive mesh refinement (AMR) is a technique that allows the solver to automatically increase the resolution in the grid based on the gradients of parameters such as temperature, pressure, or species [13]. This allows extra gridding to be added to specific locations in the domain where the flow field might be under-resolved. This allows the solver to increase solution accuracy without having to refine the mesh across the entire domain,

saving significant computational resources. The additional cells and accuracy obtained by utilizing AMR may also eliminate the need to run extensive independence studies [18].

When active, AMR adjusts grid refinement according to the same levels and equation (2.2) as fixed embedding. Three AMR processes were applied. First, AMR was permanently applied at level 2 for both the intake air and intake gas regions according to the velocity sub-grid scale (SBS). Level 3 SBS AMR was permanently applied to the MCC according to the velocity and cyclically applied to temperature beginning 3 degrees before spark until EPO (480CAD). The sub-grid criterion for velocity groups was set to 1.0m/s, and the criterion for temperature applications was set to 2.5K. In order prevent the AMR feature from increasing cell counts above reasonable computational levels, the maximum number of cells was capped to 4.5 million in the entire domain. The minimum number of cells was left unlimited.

2.2. Direct Injection Valve Model Implementation

Accurately representing the behavior of the direct injection system is critical to obtaining not only the correct ratio of air to fuel in the MCC, but also overall chamber stratification and flow patterns. The system installed on the real E565 installed in the lab is hydraulically controlled by cams mounted on the layshaft. In general, a plunger in the hydraulic pump is lifted by the cam, which then contacts a plunger in the injection valve system. This plunger hits the end of the direct injection valve stem, which then opens to allow fuel to flow into the MCC. Eventually, the cam then allows the valve to return to closed [19]. The nature of this hydraulic system introduces a set of unknown lags between the timing of the controlling cams versus when the hydraulic system eventually opens and

closes the cams. This makes it difficult to determine the actual opening and closing times of the valve within the numerical simulation. The timing diagram of the E565 is shown in Figure 2.22. The DI valve cam is set to open at 193CAD and close at 266CAD.

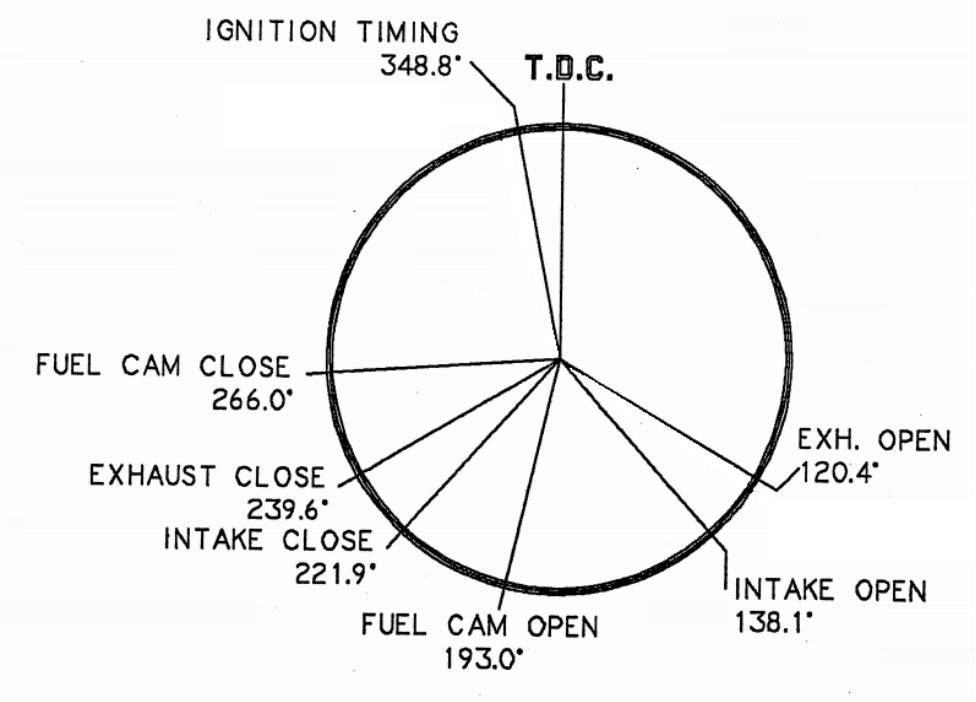

Figure 2.22: The timing diagram for the E-565. Modified from **[20]**.

In addition to the open and closing times, the overall shape of the profile as it transitions while open is difficult to determine. Bench testing outside the cylinder does not always produce meaningful results, as the lack of an actual firing cycle can produce lower than realistic lags. Although lags for the E-565 were unknown, Cooper Machinery Services was able to provide tested lag values from a similar engine, the Ajax 2800. This engine also possesses a hydraulic system, where the cam actuates a distance of 3.9mm for open and close timings at 217CAD and 296CAD. On that engine, the fuel valve actually responds at 242CAD and 299CAD, respectively. This results in an opening lag of 25CAD and a closing

lag of 3CAD. These lags were applied as a best guess in creating the profile to be used in the simulation for the E-565.

In addition, the engine is not instrumented with a pressure gauge downstream of the fuel governor, meaning the exact fuel pressure is largely unknown, aside from treating the upstream pressure as an absolute maximum before losses due to the governor. Details of the fuel pressure utilized in the simulation were discussed previously in section 2.1.3 Initial Conditions and Time Parameters. The cam lift of 3.9mm was treated as an initial maximum value to be used for the valve lift in the simulation, and after extensive iteration of valve profile, a maximum lift of 3.175mm was determined to provide the closest match to experimental data. The final valve profile showing fuel valve opening (FVO) and fuel valve closing (FVC) to simulate the hydraulic system on the E-565 is shown below in Figure 2.23. The profile was assumed to be symmetric in opening and closing.

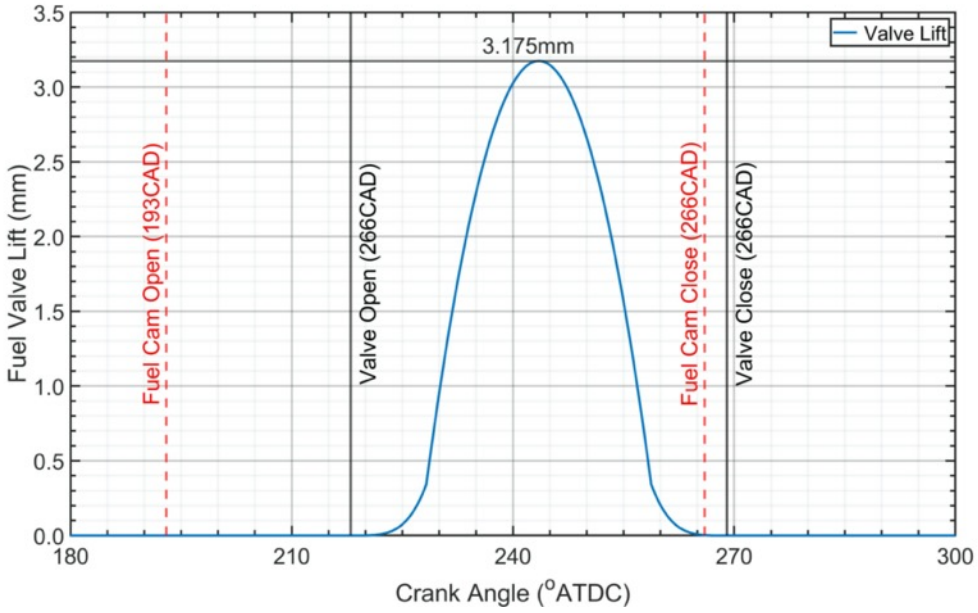

Figure 2.23: The final hydraulic direct injection fuel valve lift profile for the E-565.

The valve motion profile shown in Figure 2.23 was implemented into Converge as a translating velocity boundary condition with a cyclic valve event type between the intake gas region and the chamber.

2.3. Power and Fuel Study Setup

In this study, the valve lift profile was modified to behave like newer electronic valve systems. This eliminates the lag due to the hydraulic system, but also allows for faster actuation of the valve itself, with more defined transitions between minimum and maximum lift. In all forthcoming simulations, the electronic valve profile would be created to require 3CAD to open and also to close, a much shorter period to reach maximum lift than the hydraulic profile. In addition to swapping to the electronic valve profiles for this part of the study, the overall simulation was shortened to reduce computational time. This was accomplished by recognizing that the period between the start of the simulation at EPO and before the start of fuel injection was identical for all cases. Therefore, the state of the simulation before fuel injection (180° BTDC) was mapped to an output file and used as the starting point of future cases.

The first step to testing the electronic profiles was to provide a translation between the original hydraulic profile, shown in Figure 2.23, and the electronic simulations. This simplified electronic profile will the same maximum lift and utilize the same fuel pressure, but reduce the overall dwell time in order to account for how much longer the valve sits fully open at maximum lift. The dwell time would be iteratively reduced until the global ER was matched to that of the nominal spark timing validation simulation and served as a baseline for all electronic cases. This profile will serve as the most direct translation between

the hydraulic and electronic profile simulations. Figure 2.24 shows the electronic baseline in orange, with open and close times of 230.5CAD and 256.5CAD respectively, compared to the original hydraulic profile in blue with open and close times of 218CAD and 269CAD.

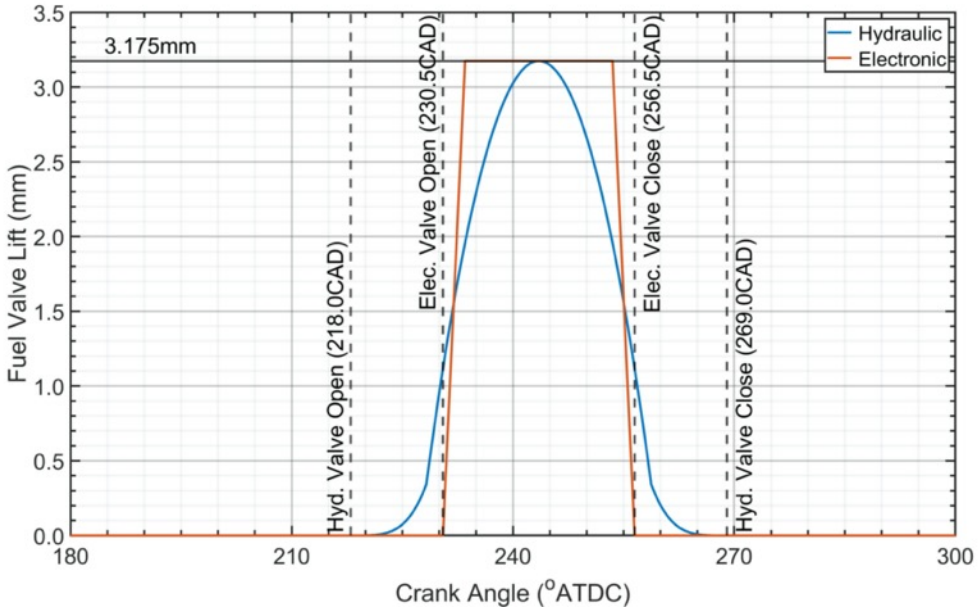

Figure 2.24: Comparison of the hydraulic valve profile and the baseline electronic valve profile.

Following creation of the electronic profile baseline, the valve open and close timings, as well as fuel header pressure were modified to determine if stratification of the MCC could promote better combustion, thus enabling leaner global ER targets. These varied electronic profiles were created such that when the overall dwell time of the valve was lengthened or shortened, the fuel header pressure was lowered or raised to produce the same global ER, eliminating ER but not stratification as a factor in performance. The results were then be analyzed to determine whether longer or shorter injection durations provide the most favorable performance, and subsequently, whether similar cylinder pressure levels to

standard operation can be produced with less fuel. Conversely, higher pressure levels may be attainable without increasing fuel consumption.

Both lengthened and shortened valve profiles were tested. After creation of the electronic baseline, a set of longer dwell profiles were created from 0CAD (baseline) to 20CAD in increments of 4CAD. Injection cannot be any longer without shifting earlier in the cycle, as the injection pressure no longer remains higher than the chamber pressure and will reverse flow. The electronic baseline (NSV) is named according to nominal spark timing (NS) and electronic valve (V) together, as well as having been started from the map file discussed prior rather than EPO. The lengthened profiles are shown in

Figure 2.25 and are labeled according to how many degrees have been added to the overall dwell time. For example, NSV+4° refers to the electronic valve profile that has a dwell time 4 degrees greater than baseline, while NSV+12° has been increased by 12 degrees. Similarly, a set of shorter dwell profiles were created from 0CAD to 16CAD, also in increments of 4CAD, and are shown in Figure 2.26. These follow the same nomenclature, save for showing negative dwell time. For example, the case that has a dwell time shortened by 8 degrees is referred to as NSV-8°. For these cases, 16 degrees is the maximum that the dwell time can be reduced before the valve can no longer reach maximum lift and still maintain 3 degrees to open and close.

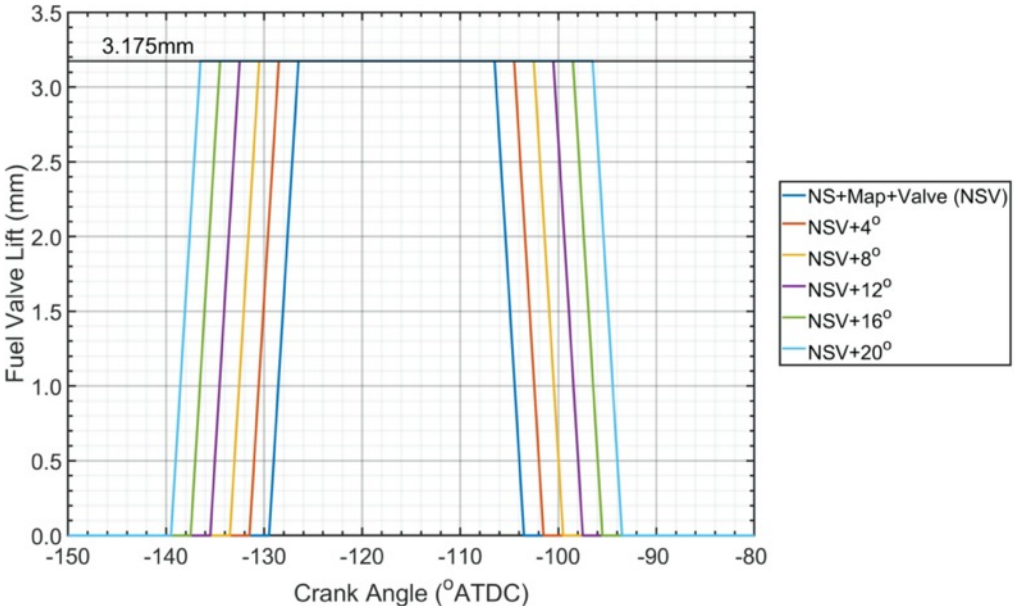

Figure 2.25: Increased dwell time electronic valve lift profiles.

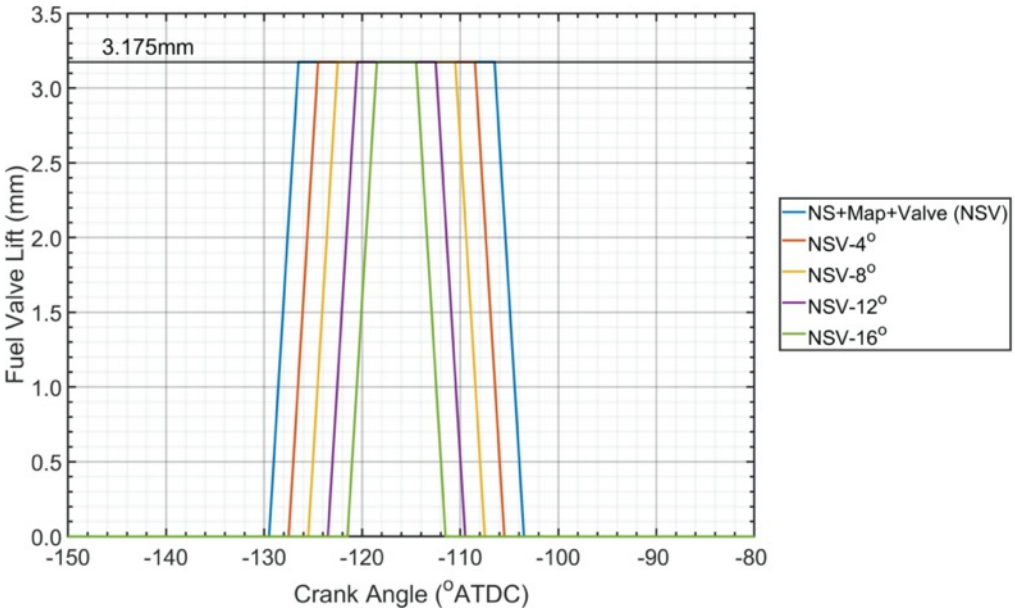

Figure 2.26: Decreased dwell time electronic valve lift profiles.

For each of these dwell times, the fuel header pressure was raised or lowered in order to maintain the desired global ER. The brute force approach would involve guessing a fuel

header pressure, then running the simulation through the end of the injection process to determine the global ER. Iteration is then performed by raising and lowering the pressure until hitting the target. This is not only time consuming and costly; it must be completed for each altered valve profile. While this approach certainly works, it lacks efficiency and wastes tremendous amounts of computation hours at great expense.

An alternative approach was implemented to produce estimates for where the fuel pressure needed to be set for a given valve profile. This was performed by applying isentropic fuel flow relations through a nozzle as an estimate to the required fuel pressure to maintain desired equivalence. Details of these formulations are discussed in APPENDIX B: Fuel Header Pressure Estimation. In summary, the direct injection fuel valve was modeled as ideal flow through a nozzle, and numerical integration was utilized to match overall mass flowing through the valve relative to the amount of air present in the nominal spark case. While this approach was not perfect and neglects many effects almost certainly occurring in the engine, it did greatly improve the starting estimates for the fuel pressure required. This reduced waste of computational hours and significantly cut down the number of iterations required per profile. Table 2.7 summarizes the pressures obtained, as well as the open and close timings of each profile.

Table 2.7: Summary of valve profile timings and pressures.

	Case	Valve Open (CAD)	Valve Close (CAD)	Fuel Pressure (kPa)
Base Case	**NSV**	230.5	256.5	142.0
Increased Injection Period	**NSV+4°**	228.5	258.5	137.8
	NSV+8°	226.5	260.5	135.6
	NSV+12°	224.5	262.5	133.5
	NSV+16°	222.5	264.5	131.0
	NSV+20°	220.5	266.5	128.7
Decreased Injection Period	**NSV-4°**	232.5	254.5	149.8
	NSV-8°	234.5	252.5	168.9
	NSV-12°	236.5	250.5	214.4
	NSV-16°	238.5	248.5	326.3

3. RESULTS AND DISCUSSION

After finalizing the configurations of the simulations, the runs were started on one Texas A&M University's high performance computing clusters, Ada. After a few initial short tests to optimize core and memory requirements, each run was queued to have parallel access to 160 cores and 2.5GB of memory per core running Converge MPICH solver version 3.0.15. This was a target of approximately 5,000 cells per core, although this number could reach a theoretical maximum near 28,000 cells per core, using the AMR ceiling of 4.5 million cells as a reference. This maximum is still within a reasonable computational window, and the single longest simulation required approximately 8 wall-time days. On average, shortened simulations started from the map file (allowing simulations to begin just before the fuel injection process rather than EPO) required less time of approximate 4 wall-time days and were run through to the end of the cycle.

3.1. Model Validations and Grid Independence

Validation is required to build trust in the accuracy of any numerical simulation. In order to do so for this study, the numerical results were first examined to ensure grid independence. Secondly, they were compared to experimentally obtained datasets across three different operating points of the instrumented Ajax E-565, including nominal spark timing, retarded spark timing, and advanced spark timing. Successful validation across these three points will suggest that the numerical simulation performs similarly to the real engine. This allows the numerical simulation to be used to predict how the engine might respond to

changes in various parameters and examine what may not usually be accessible with physical instrumentation.

3.1.1. AMR and Grid Independence

As discussed previously, the implementation of AMR may eliminate the need to run extensive grid independence studies. AMR allows the solver to automatically refine the mesh in areas where calculated gradients are too high, simultaneously improving computation time and increasing the accuracy of the solution. Across all simulations, AMR was limited to a maximum of 4.5 million cells. In a similar fashion, FE allows for mesh to be selectively refined in areas of critical importance without the need to cripple performance by refining the entire solution domain. Figure 3.1 displays the total cell count in all regions combined on a crank angle basis for the nominal spark, retarded spark, and advanced spark cases used for experimental validation.

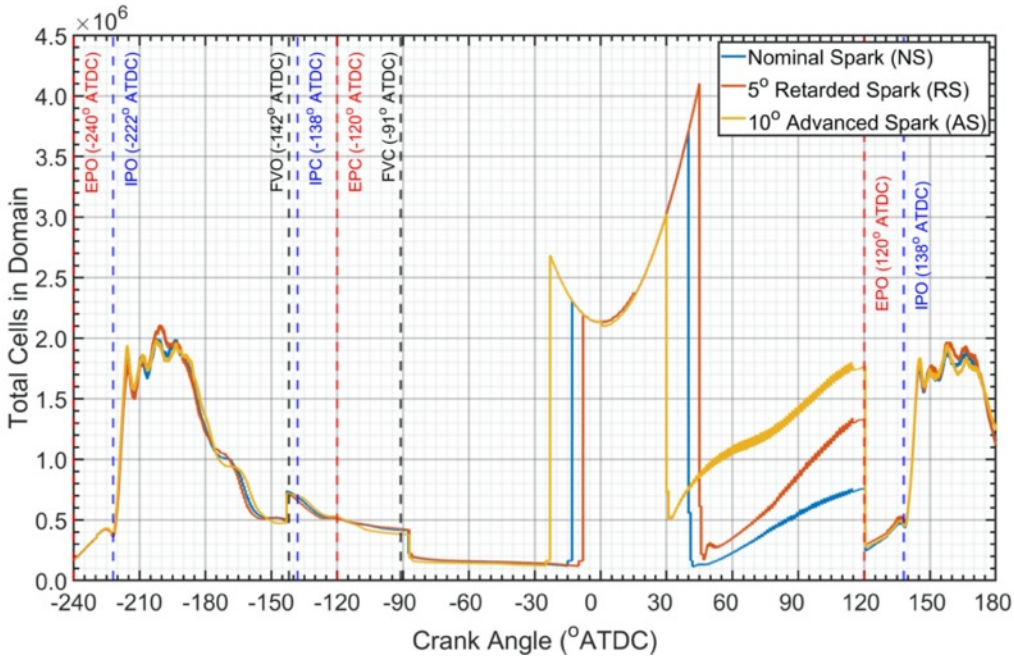

Figure 3.1: Total cell counts in the solution domain.

In Figure 3.1, the effects of grid refinement and various events within the engine were visible at a number of different crank angles of note. First, the sharp rise in cell count due to the fuel injection valve fixed embedding may be seen between FVO (-142°ATDC) and FVC (-91°ATDC). Small rises due to the spark plug embedding are visible at -24.2° (AS), -14.2° (NS), and -9.2° (RS). While the level 4 embedding level for the spark plug was high and a large increase in cells was expected, the size of the embedding sphere was relatively small in the scope of the cylinder size. Just after the spark embedding went active, the level 3 chamber embedding initiated at -23.2° (AS), -13.2° (NS), and -8.2° (RS).

The effects of the applied AMR groups were also visible from the consistently changing number of cells outside of the specific FE periods. This was weakly noticeable in the period immediately following EPO but before IPO, when AMR detected high velocity gradients of gas exiting the MCC through the exhaust manifold and applied refined mesh. Similarly, this was more strongly evident upon IPO, when the cell counts increased from less than 500,000 cells to over 1.5 million to resolve the flow of fresh charge from the intake manifold into the MCC. Finally, upon deactivation of the chamber FE at 51° after spark for each respective case, level 3 velocity and temperature AMR may be seen continuing to add additional cells until EPO. Maximum cell counts were reached at the tail end of chamber FE for all three spark timing cases, and the maximum 4.5 million cells allowed by AMR was never reached. This suggests that no gradients in the MCC were high enough to trigger AMR to further refine the mesh and implies independence from the grid size. Cell counts for the remaining pressure and fuel study cases are included in APPENDIX A: Additional Figures.

3.1.2. Air and Exhaust Manifold Experimental Validation

After establishing grid independence, the models were validated against experimentally measured parameters, starting with measured air and exhaust manifold pressures. As discussed previously in sections 2.1.3 Initial Conditions and Time Parameters and 2.1.7 Boundary Conditions, 200 cycle averages of the air and exhaust manifold pressures were used as boundary conditions for the air intake and exhaust outlets as well as initial conditions for the intake air and exhaust regions. The initial conditions begin to wash away as soon as the simulation marches away from time zero (EPO), and the boundary conditions for inflow and outflow do not directly maintain regional conditions. For this reason, the availability of crank angle resolved air and manifold pressures from experimental datasets provide a strong basis to begin comparing against numerical simulation results.

3.1.2.1. Air Manifold Pressures

The nature of the E-565 as a cross-scavenged two-stroke means that the pressure in the air manifold plays a critical role in how strongly the fresh charge helps flush burned gases out [3]. This not only has a large impact on the residual mass left in the MCC but also significantly affects the overall mass of air inducted into the cylinder. The scavenging process and inflowing air mass both create a flow field that later interacts with the fuel injection cloud. If the model fails to predict the air manifold pressure accurately, the scavenging could be unrealistic, the ER of the cycle could be impacted, and the overall mixing within the chamber would likely not represent proper operation of the engine.

Figure 3.2 below compares the air manifold region pressures between experimentally obtained data and the results of the numerical simulation. 200 individual experimental cycles

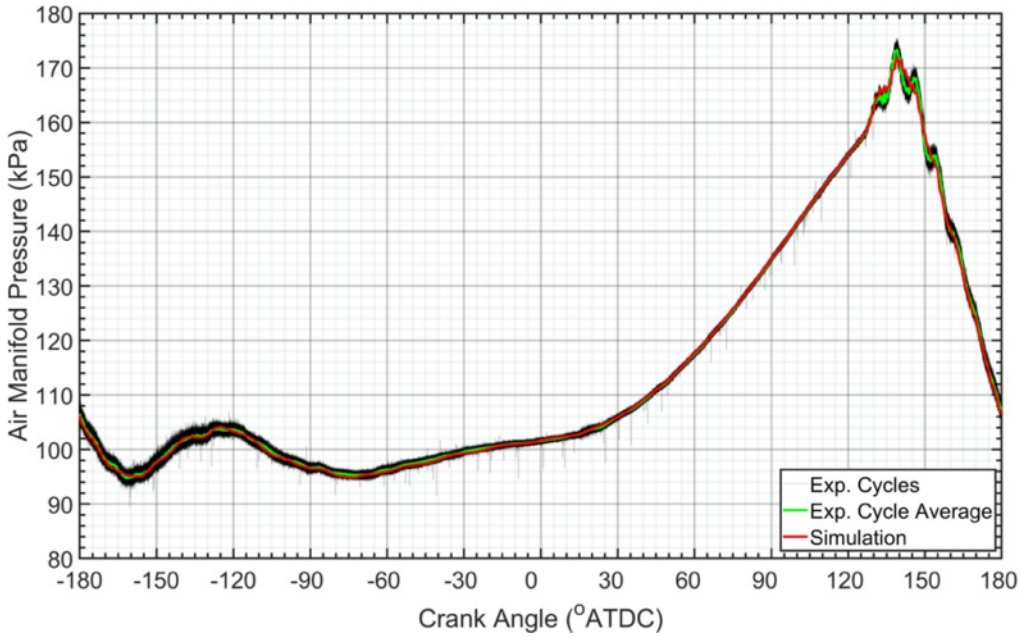

Figure 3.2: Experimental and numerical simulation validation using air manifold pressure comparison at nominal spark timing across one cycle.

at nominal spark timing and high speed high load are shown overlaid on each other in black, while the average of those 200 experimental cycles is shown in green. The CFD simulation results are shown in red. Across all crank angles, the simulation validates well, and results fall within the spread of the individual cycles, even during the critical period of IPO to IPC. This suggests that the numerical model predicted the air manifold pressure well for the nominal spark case.

To ensure that the model validated well across multiple operating points, the same information was compared when running the engine at 10° advanced spark timing and 5° retarded spark timing. The air manifold pressures for AS and RS are shown below in Figure

3.3 and Figure 3.4, respectively. Displaying individual experimental cycles, experimental average, and the simulation results similarly to the NS case, the numerical simulation was seen to also be accurately modeling the air manifold pressures for the additional spark timings. Of note, the 200 individual experimental cycles were randomly selected, eliminating cycle to cycle variance as a false validation. In terms of the air manifold pressures, performance was relatively consistent, and cycle to cycle variation within the experimental dataset was low.

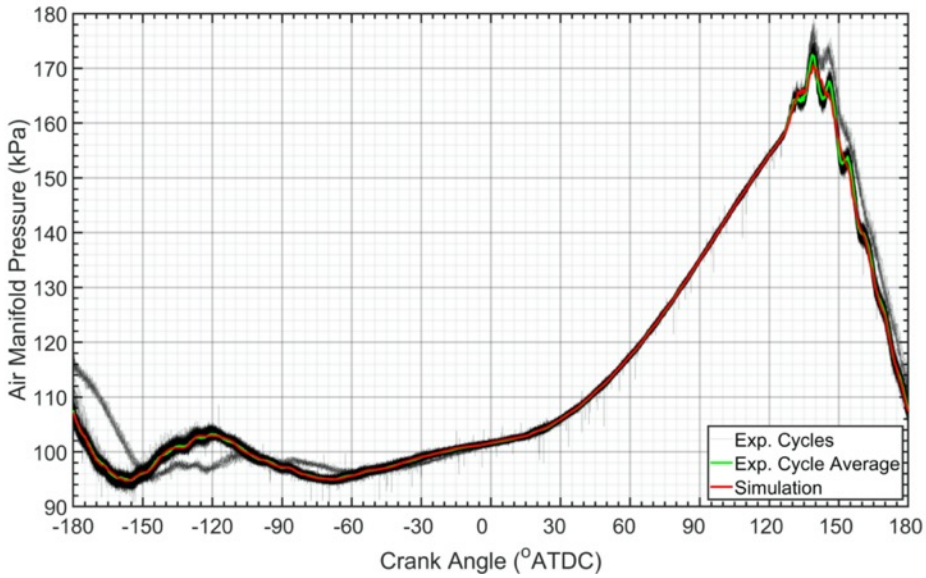

Figure 3.3: Experimental and numerical simulation validation using air manifold pressure comparison at advanced spark timing.

The intake manifold pressures are also impacted by the position of the piston. In the E-565, the air intake manifold serves as a bridge between the MCC intake ports and the stuffing box. As the piston moves up and down within the chamber, the crank side of the piston creates a scavenging chamber in the crankcase. As the piston rises during the

compression stroke, a vacuum is created in the stuffing box to draw in fresh air to the stuffing box and air intake manifold. Similarly, as the piston drops during expansion, this air is pressurized, helping to scavenge the MCC and induct fresh air [5].

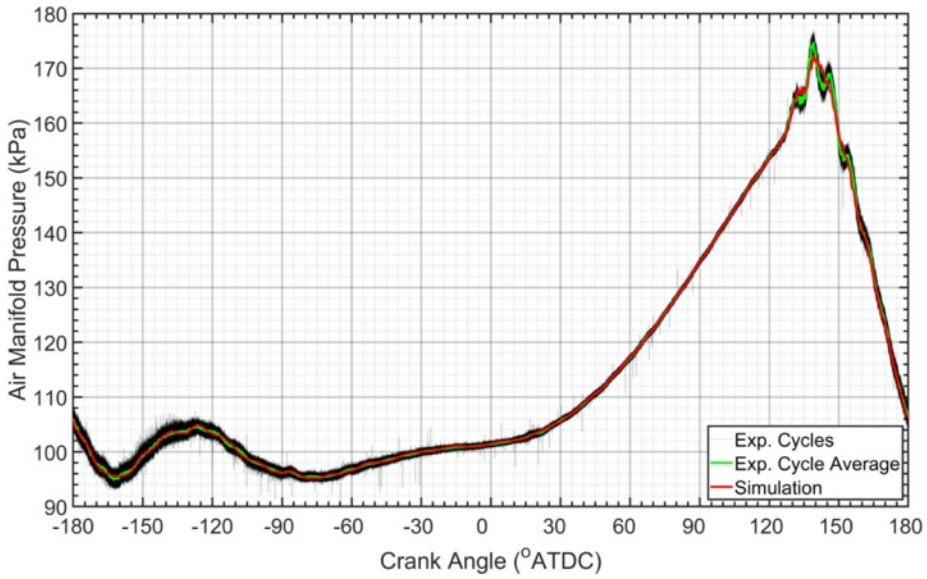

Figure 3.4: Experimental and numerical simulation validation using air manifold pressure comparison at retarded spark timing.

Across all three validation cases, the pressure fluctuated first at the beginning of the cycle (intake ports are already open at -180°ATDC) until IPC at -138°ATDC. An expected pressure rise occurred beginning at 0°ATDC due the expansion stroke of the piston pressurized the stuffing box, and the pressure began dropping from peak again once IPO occurred at 130°ATDC. A close match between the experimentally obtained air manifold pressures and numerical pressures validated the air manifold pressure and the interaction of the piston geometry with the stuffing box during the entire cycle.

3.1.2.2. Exhaust Manifold Pressures

Like with the air manifold pressures, the experimental and numerical exhaust manifold pressures were compared for validation across an entire simulation cycle, save for the critical moment of interest now falling between EPO and EPC as burned gases are flushed out of the MCC. Of note, the exhaust ports were already open at -180°ATDC then closed at -120°ATDC. After the combustion process occurs, the ports reopen at 120°ATDC. Figure 3.5 displays the exhaust manifold pressures for the NS case, while Figure 3.6 and Figure 3.7 show the AS and RS cases.

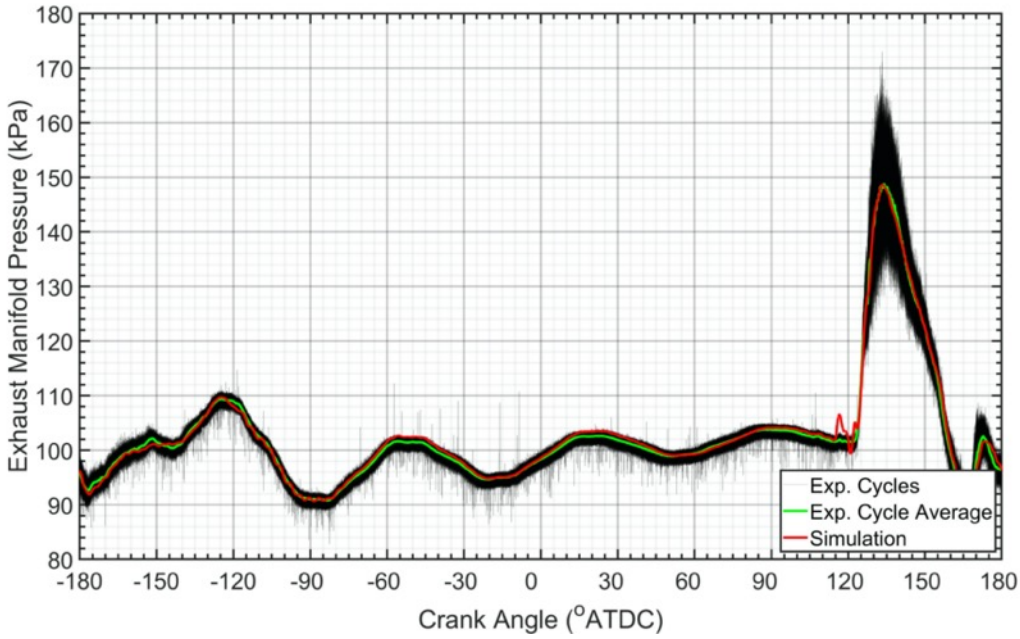

Figure 3.5: Experimental and numerical simulation validation using exhaust manifold pressure comparison at nominal spark timing.

As before, 200 randomly selected individual experimental cycles are shown in black, while the average of those individual cycles is overlaid in green. The CFD simulation results are shown in red. In general, the maximum spread of the individual cycles was low for the

majority of the cycle; however, during the period between EPO (120°ATDC) and 180°ATDC, the experimental spread was much higher. The CFD model once again validates well. The pressures are within the spread of the individual experimental cycles across all crank angles, and frequently lay close to the experimental average, even while the exhaust ports are open.

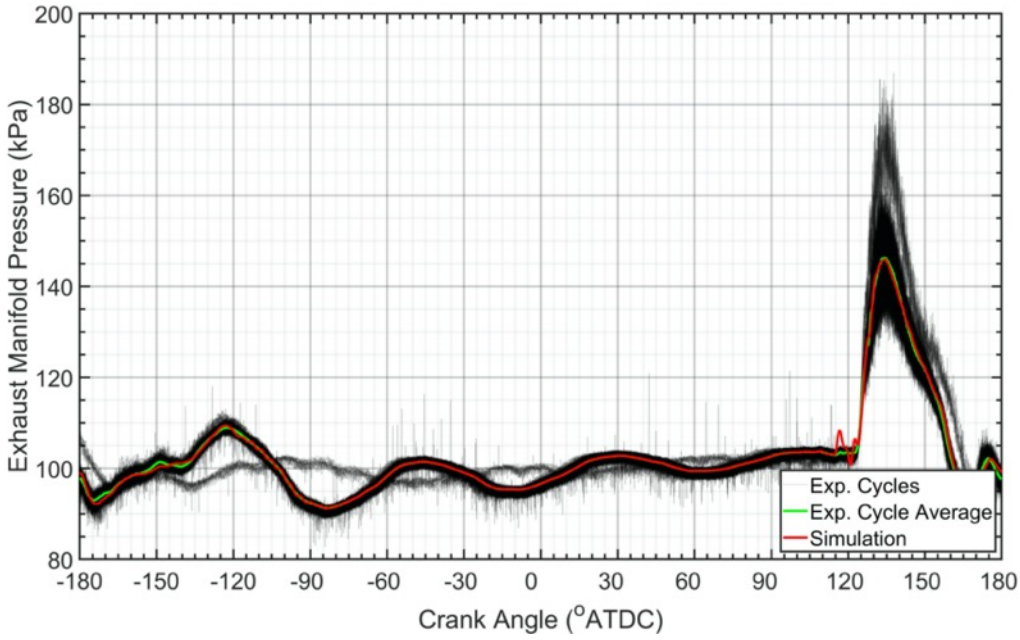

Figure 3.6: Experimental and numerical simulation validation using exhaust manifold pressure comparison at advanced spark timing.

Across all three numerical simulation cases, a slight pressure fluctuation of approximately 4kPa amplitude was observed just before EPO at 115°ATDC. This phenomenon was found to be due to a slight mismatch in the port geometry height compared to the real engine. In the CFD simulation, boundaries must have perfect intersections and do not incorporate tolerances. Investigation revealed that the cleaning of the geometry to create the perfect intersections, combined with the implementation of sealing described in 2.1.6

Boundary Intersection Handling and Seals, resulted in the exhaust ports opening slightly earlier in the numerical simulation compared to on the physical engine. However, after this brief period, exhaust manifold pressure levels quickly returned to within range of the experimental validation datasets.

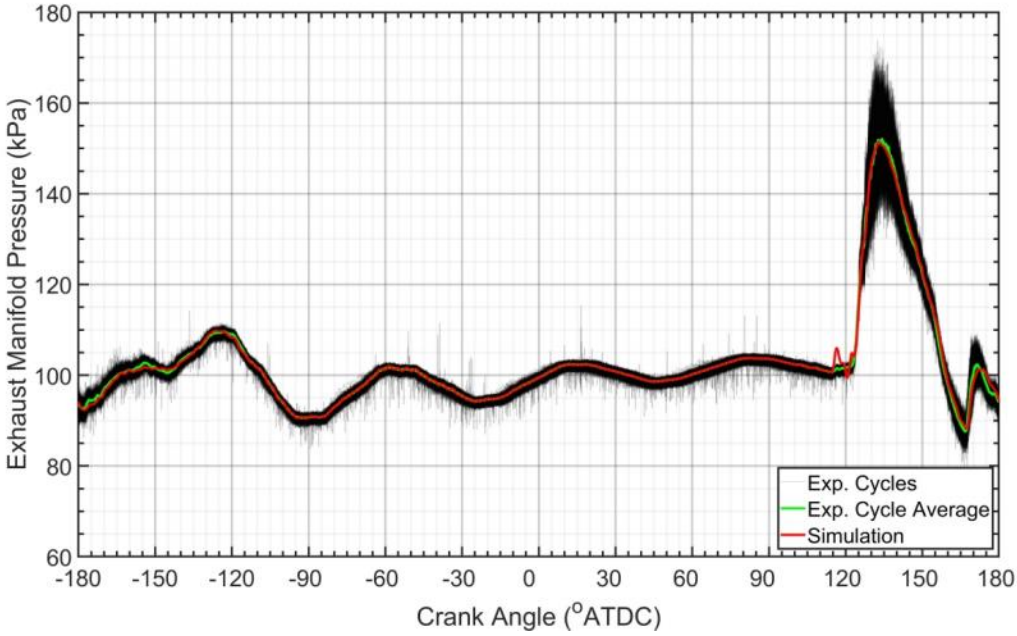

Figure 3.7: Experimental and numerical simulation validation using exhaust manifold pressure comparison at retarded spark timing.

3.1.3. Main Chamber Experimental Validation

Unlike the intake manifold and exhaust manifold pressures, the MCC pressure experiences greater variances cycle to cycle, which may typically be quantified by examining the coefficient of variability of indicated mean effective pressure (COV_{IMEP}). While a single numerical cycle fails to provide enough data to directly compare against experimental COV_{IMEP}, the overall pressure trace may be examined to ensure it properly models real world performance. Figure 3.8 shows the spread of 200 randomly selected

individual MCC pressure traces along with the average of those cycles shown overlaid in red for NS, AS, and RS cases.

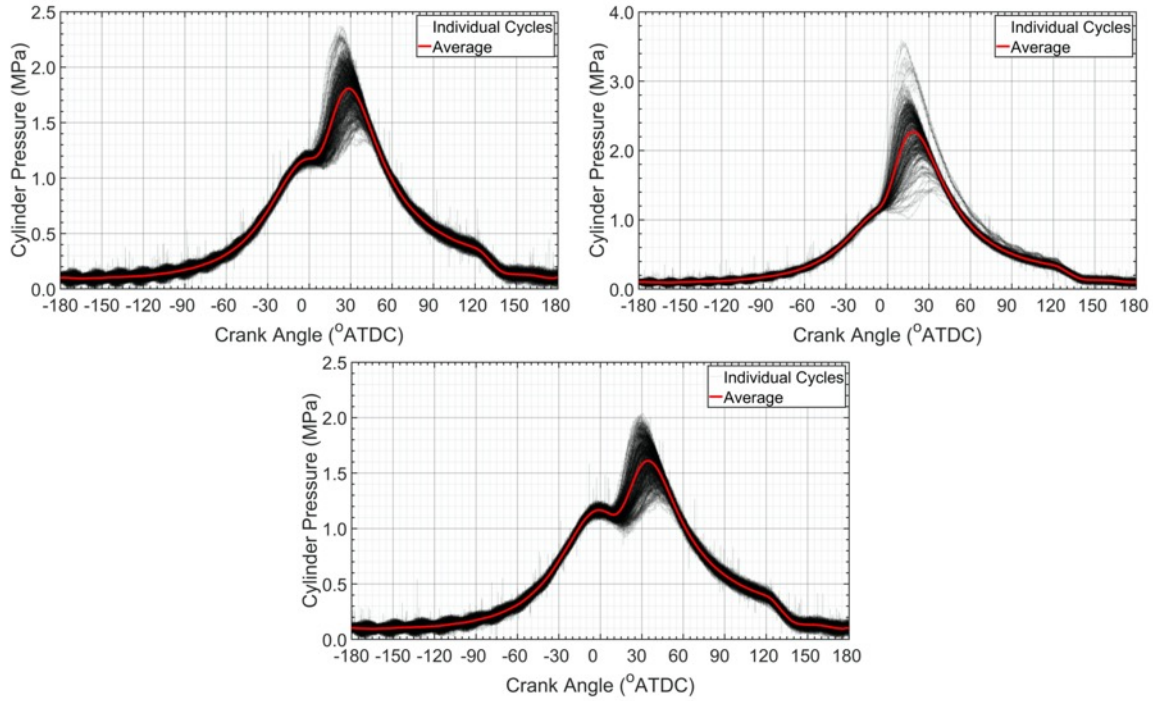

Figure 3.8: Individual experimentally measured in-cylinder pressure traces and 200 cycle average for nominal spark (top left), advanced spark (top right), and retarded spark (bottom), all at high speed, high load.

Validation involved first assuring that the compression strokes were similar to the experimental traces, supporting proper inlet pressure conditions and correct total mass being present in the MCC. Secondly, the trace from spark through expansion and exhaust should fall somewhere within the spread of traces that exist for a given operating point. Rather than try to model an average trace that may not be representative of any single realistic cycle, each of the three experimental datasets was examined to find out if a real cycle existed that was similar in nature to the numerical simulation prediction. Beginning with the NS case,

Figure 3.9 displays three selected experimental pressure traces compared against the numerical simulation results. It was evident that the simulation results, shown in black,

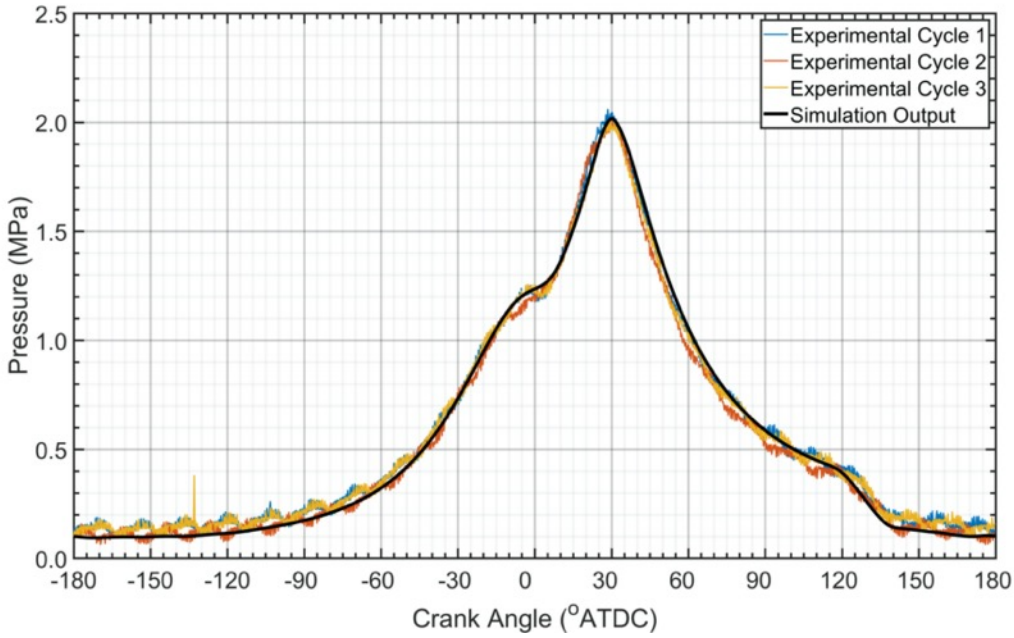

Figure 3.9: Validation of the numerically simulated cylinder pressure with experimental pressure datasets for nominal spark timing.

strongly match with the three colored experimental cycles. Although the experimental traces are noisy, the numerical simulation tracks well through the compression coming into TDC, and the pressure rises begin at almost identical crank angles. The location of peak pressure falls at 30.5°ATDC for the numerical cycle, and the peak pressure locations are estimated to be between 28°ATDC and 30°ATDC for the experimental cycles. Peak pressure during the simulation was 2.02MPa, while the experimental traces 1, 2, and 3 reached peaks of 2.06MPa, 2.01MPa, and 2.02MPa, respectively. Following the expansion after peak pressure levels, the simulation continued to track well with the experimental traces until EPO (120°ATDC). At 115°ATDC, the early exhaust port opening in the simulation was once

again evident, as discussed previously in 3.1.2 Air and Exhaust Manifold Experimental Validation. The impact was minor, and the pressure quickly returned to levels similar to the experimental traces. Figure 3.9, along with Figure 3.2 and Figure 3.5, successfully validate the results of the high speed, high load NS case.

A similar comparison was completed for the RS case, shown in Figure 3.10, and the AS case, shown in Figure 3.11. Compression, location of peak pressure, and peak pressure values matched similarly well across both. For RS, pressure immediately following TDC but before peak pressure (approximately 0°ATDC to 30°ATDC), was over-predicted in the numerical simulation and pressure rise was slower than expected. The experimental data has a harmonic-like noise with a period of approximately 10CAD, and a valley of that signal appears in the low pressure region. This was not considered to be an invalidation of the

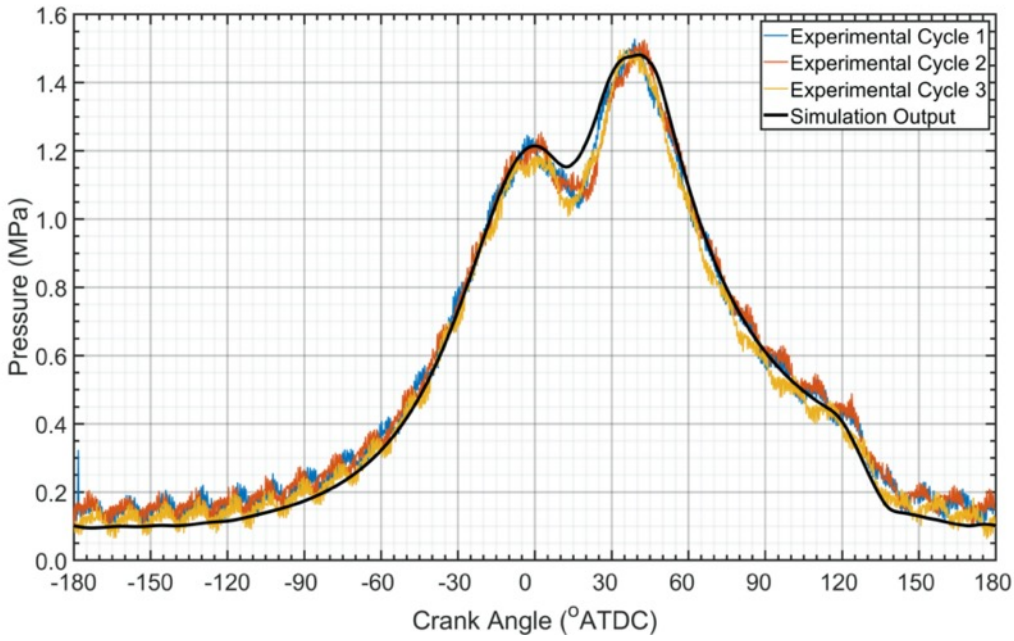

Figure 3.10: Validation of the numerically simulated cylinder pressure with experimental pressure datasets for retarded spark timing.

numerical model. The expansion after peak pressure continued to track well with the experimental dataset for the RS case, but beginning at the location of peak pressure (LoPP), the AS case increasingly over-predicted. This was believed to be due to thermal shock occurring with the pressure transducer in the experimental dataset. As the AS operating point produces higher pressures, subsequent in-cylinder temperatures are higher, progressively heating the transducer through the expansion stroke. For both RS and AS, similar behavior to the NS case was observed just prior to EPO. Combining the analysis of air manifold pressures, exhaust manifold pressures, and in-cylinder pressures through the entire cycle across three different spark timings, the numerical model was validated.

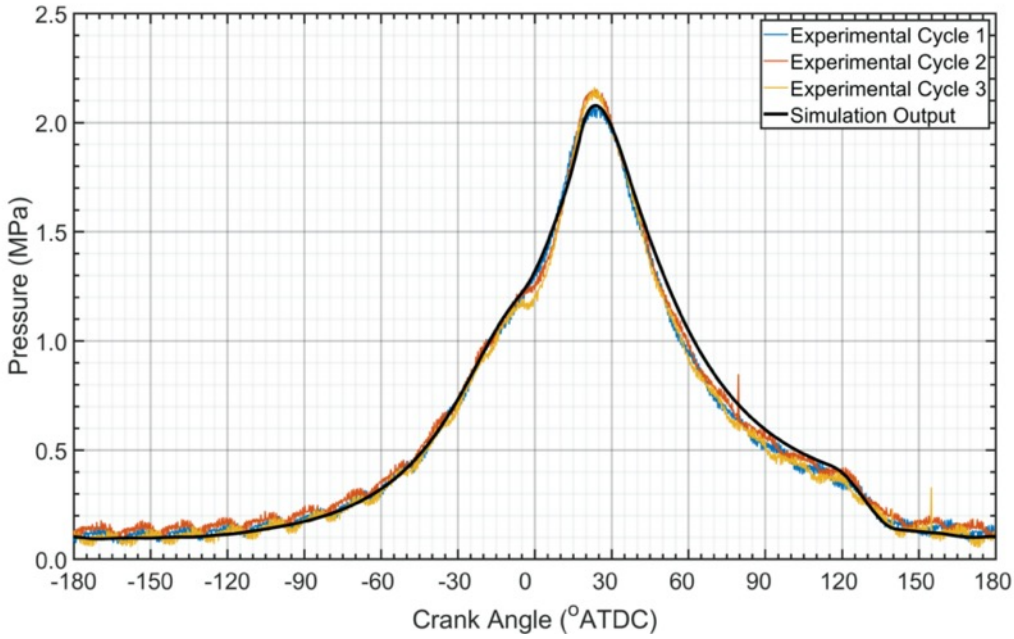

Figure 3.11: Validation of the numerically simulated cylinder pressure with experimental pressure datasets for advanced spark timing.

3.2. Pressure and Fuel Study Results

With successful modeling and validation of the CFD model against experimental datasets, the numerical results may be trusted to sufficiently predict real-world performance. As described earlier in section 2.3 Power and Fuel Study Setup, the fuel valve lift profiles were modified to behave more like electronic valve systems, with faster open and close actuations and straighter transitions between minimum and maximum lift. The results were analyzed to establish which profiles, longer or shorter durations, produced the most favorable stratification for a low pressure injection system, as well as which profile could produce the most pressure for the same amount of fuel. The most favorable profile was then selected and tested at progressively lower fuel header pressures to reach a minimum global ER before misfire.

Before beginning testing of the modified profiles, a baseline electronic case was created as a reference. To provide the most direct translation between the original NS case and an "equivalent" electronic case, only two changes were made. First, the valve profile was changed from the original NS hydraulic validation profile to the new trapezoidal electronic profile. While maintaining the same 142kPa fuel header pressure of the NS case, the open and closing times were symmetrically shortened until reaching the same global ER as in the original NS case. Secondly, rather than beginning the simulation at EPO, the state of the NS simulation was mapped at -180°ATDC. This served both to provide an identical starting point across all studies and reduce the overall length of the simulation by 66CAD, saving computational resources. Primarily, the electronic baseline was not expected to provide an identical match but was intended to serve as a point of relativity for future tests.

The results of matching the global ERs of the NS case and electronic baseline are shown below in Figure 3.12 across three cases: the original NS validation, the NS case with no changes aside from implementing the map file (NS+Map), and the NS case with both the map file and the electronic valve implementation (NSV). Compared to the validated NS case, the introduction of the map produces a slight decrease in ER, but the ER was able to be adjusted slightly higher with the chosen timings of NSV. The final electronic valve baseline profile for NSV was shown and compared to the validated hydraulic valve profile in Figure 2.24.

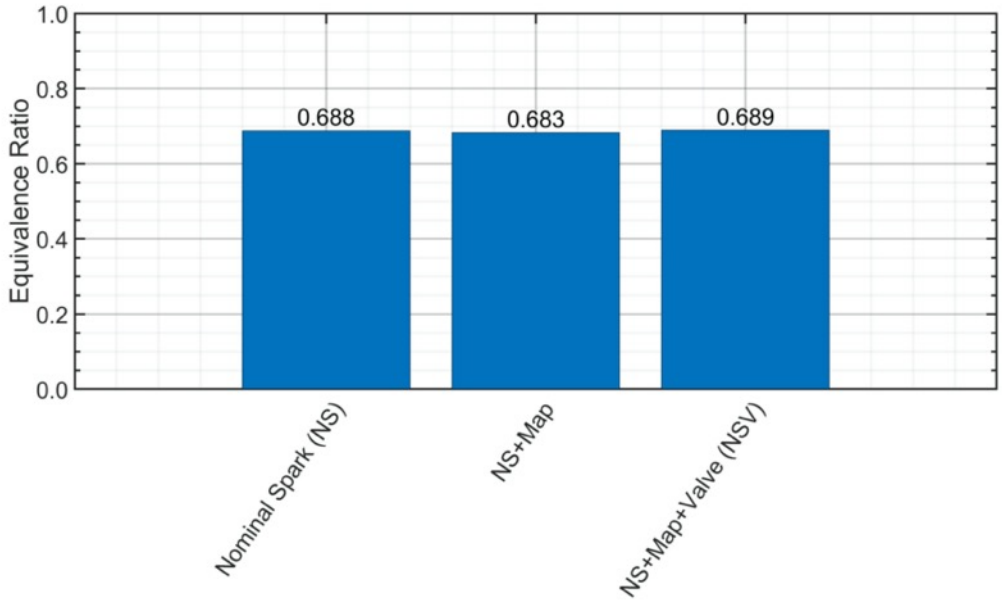

Figure 3.12: Global equivalence ratio comparison between NS, NS with mapping, and NS with mapping and electronic valve profile.

One of the requirements for the pressure and fuel study was to maintain a similar global ER across all cases to eliminate ER as a contributing factor in any observed changes in performance. The results of creating the electronic baseline also gave an indication of

how closely the global ERs could feasibly be matched, so a 1% tolerance was implemented. To that end, taking the base case as NS an ER of 0.688, all future cases were required maintain global ERs within 0.681 to 0.695.

Figure 3.13 displays the in-cylinder pressure of the NS case directly compared against the results from NS+Map and NSV. The key change was between the NS and NS+Map cases. In this instance, starting the simulation from the map file brought two impacts: slight reduction of peak pressure from 2.02MPa (NS) to 1.91MPa (NS+Map) and a similarly small ignition delay leading to LoPP shifting from 30.2°ATDC (NS) to 32.3°ATDC (NS+Map). Changes were expected from implementing the electronic valve, but the variation between NS and NS+Map was explained by examining the total cell count in the solution domain, shown in Figure 3.14. While the map file maintained all variables

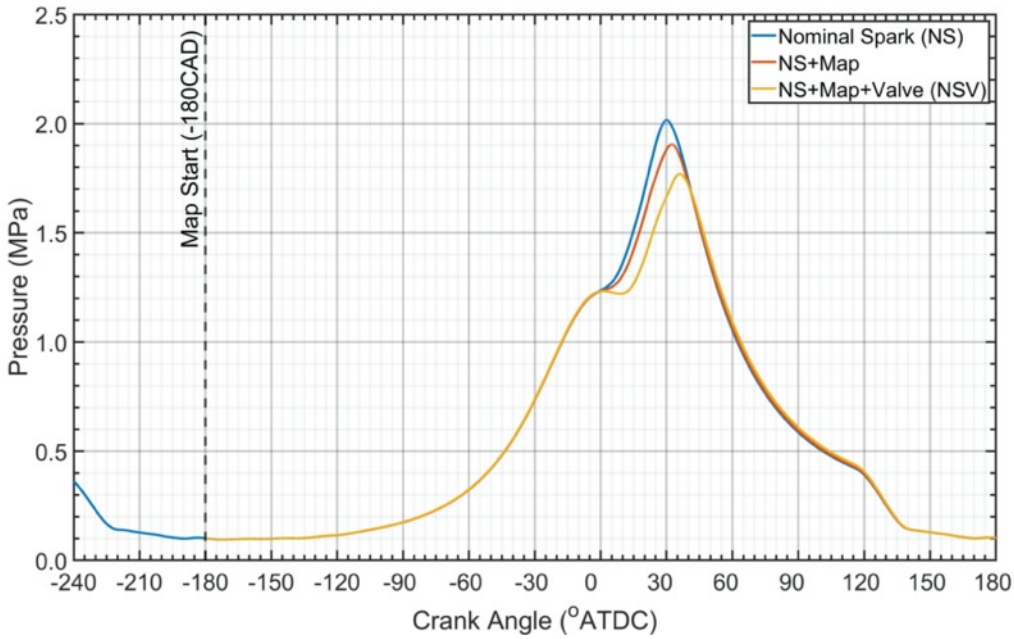

Figure 3.13: Translating performance between the NS case, implementation of variable mapping, and addition of the electronic valve profile.

from the NS case, the mesh at that moment was not maintained. As a result, NS+Map and NSV reinitialized cells counts and immediately began reapplying AMR. The difference in mesh explains the discrepancy, and for the remaining studies, they will all initialize from the same conditions. With that in mind, any observed changes in the following studies were accurate relative to the NSV baseline.

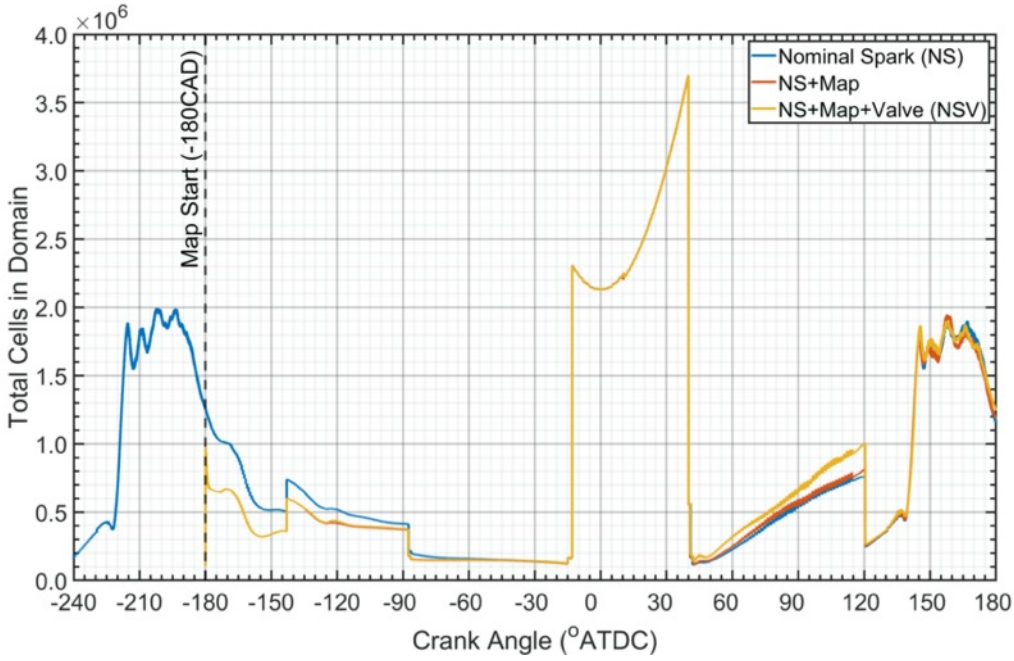

Figure 3.14: Crank angle resolved total cells in the domain for NS, NS+Map, and NSV.

3.2.1. Increasing Overall Injection Duration

After establishing the electronic valve profile baseline, the effects of increasing the overall injection duration were examined. As discussed previously, injection durations were increased by 4, 8, 12, 16, and 20CAD relative to the baseline, and the fuel header pressures were initially estimated according to the process described in APPENDIX B: Fuel Header Pressure Estimation. If an ER was outside of the 1% margin, it was iteratively adjusted until

testing within range. 20CAD served as the maximum the duration could be increased before the injection pressure could no longer be maintained as higher than the chamber pressure, and an additional case of a 2CAD increase was produced to increase resolution near the default electronic baseline profile. Table 3.1 reintroduces the increased dwell time profiles, as well as the final fuel pressures that resulted in acceptably matched ERs. As stated before, cases are named according to the base case (NSV) then by how many CAD the valve lift profile has been increased or decreased. For example, NSV+4° represents the case where valve duration has been increased by 4 degrees. The resulting global ERs are presented in Figure 3.15. All measured global ERs were within

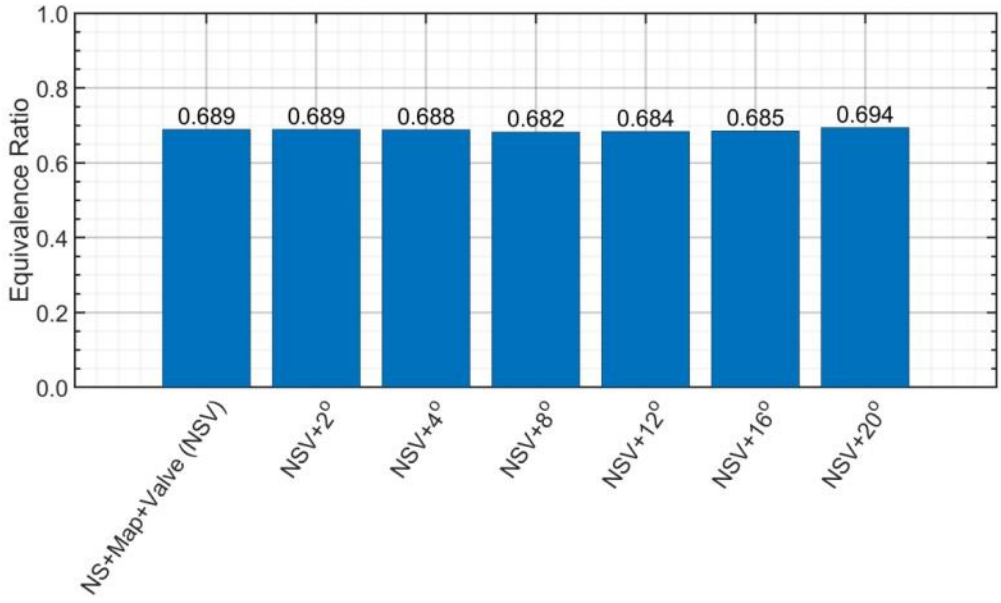

Figure 3.15: Global equivalence ratios for all increased fuel injection period cases.

the desired 1% range of 0.681 to 0.695, sufficiently supporting that ER was not responsible for any major variations in performance.

Table 3.1: Summary of increased injection timings and pressures.

	Case	Valve Open (°ATDC)	Valve Close (°ATDC)	Pressure (kPa)
Baseline	**NSV**	-129.5	-103.5	142.0
Increased Injection Period	**NSV+2°**	-130.5	-102.5	139.6
	NSV+4°	-131.5	-101.5	137.8
	NSV+8°	-133.5	-99.5	135.6
	NSV+12°	-135.5	-97.5	133.5
	NSV+16°	-137.5	-95.5	131.0
	NSV+20°	-139.5	-93.5	128.7

The results for crank angle resolved cylinder pressure changing as a function of lengthening the valve lift profile and reducing fuel injection pressure are shown below in Figure 3.16. Referenced against NSV, increasing the injection duration to NSV+2° from baseline initially increased peak pressures and advanced LoPP. The trend continued and reached a maximum with NSV+4°, which reached a peak pressure of 2.00MPa at 31.18°ATDC, an increase of 12.8% pressure and 4.84CAD earlier LoPP relative to NSV.

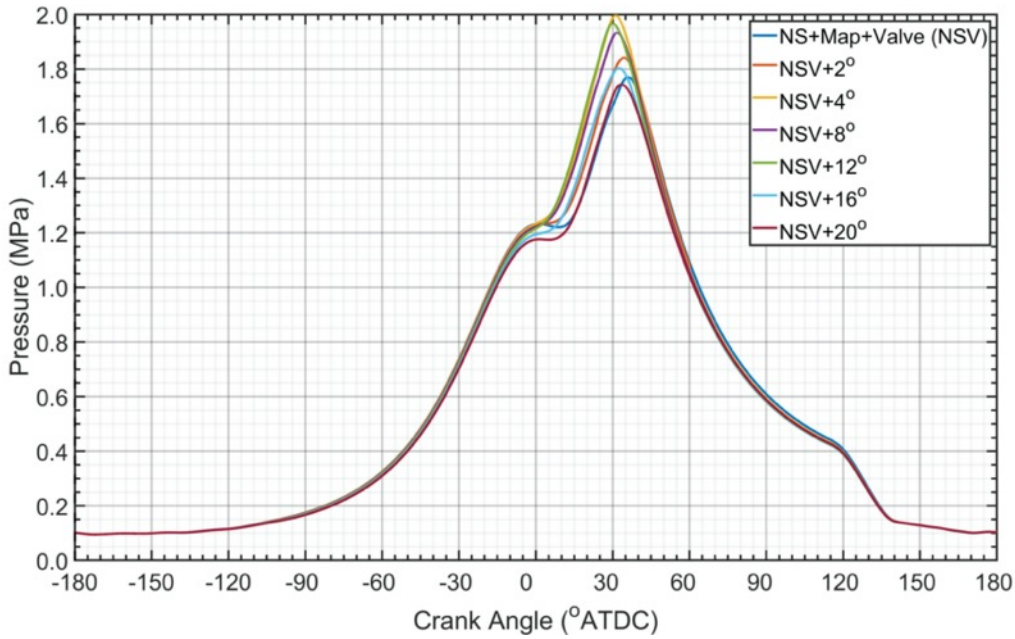

Figure 3.16: Cylinder pressures for all increased fuel injection period cases.

Once injection duration was increased to 8CAD and higher, the trend began to reverse and peak pressures fell back toward NSV and retard LoPP relative to NSV+4°, although still not as late as NSV. NSV+12° falls just barely outside the trend, with a peak pressure higher than NSV+8° and a slightly more advanced LoPP. Table 3.2 summarizes the increased valve duration pressure data.

Table 3.2: Summary of increased valve duration pressure data.

Case	Peak Pressure (MPa)	Percentage Increase from NSV (%)	LoPP (°ATDC)	LoPP Ret./Adv. from NSV (CAD)
NSV	1.77	-	36.03	-
NSV+2°	1.84	3.95	34.54	1.49 ADV
NSV+4°	2.00	12.87	31.19	4.84 ADV
NSV+8°	1.93	9.23	31.79	4.24 ADV
NSV+12°	1.97	11.15	29.95	6.08 ADV
NSV+16°	1.80	1.86	32.46	3.57 ADV
NSV+20°	1.74	-1.51	33.34	2.69 ADV

In order to truly investigate the impacts of the valve and pressure changes on the performance of the engine, a number of processes need to be examined outside of what can be shown on a pressure trace. Mass fraction burned (MFB) profiles are one way to characterize differences across the various stages of combustion, including the flame development period, the rapid-burning period, and the overall burn duration. In particular, the early phase of flame development is highly sensitive to the composition of the mixture and the flow field near the spark plug, while the rapid-burning period becomes more dependent on conditions throughout the rest of the MCC [3]. According to Heywood, MFB may be obtained integrating the rate of heat release (ROHR), then normalizing to unity [3].

The flame development period (or ignition delay period) is characterized as the period of time beginning with electric discharge at spark until the flame begins to develop locally at the plug. Although difficult to define the exact moment when the flame has developed, the fraction may generally be accepted as 10% MFB [3]. The majority of the mixture burns during the rapid-burning period, which occurs after flame development and lasts until the flame completes propagation through the cylinder, a period indicated by 10-90% MFB. The combination of the two defines the overall burn duration, and after reaching 90% MFB, the flame may be considered terminated [3]. Ultimately, the pressure in the MCC is a direct result of the combustion characteristics of the MFB curve.

Figure 3.17 displays the crank angle resolved mass fraction burned for the increased valve duration cases, while Figure 3.18 displays the overall durations of the flame

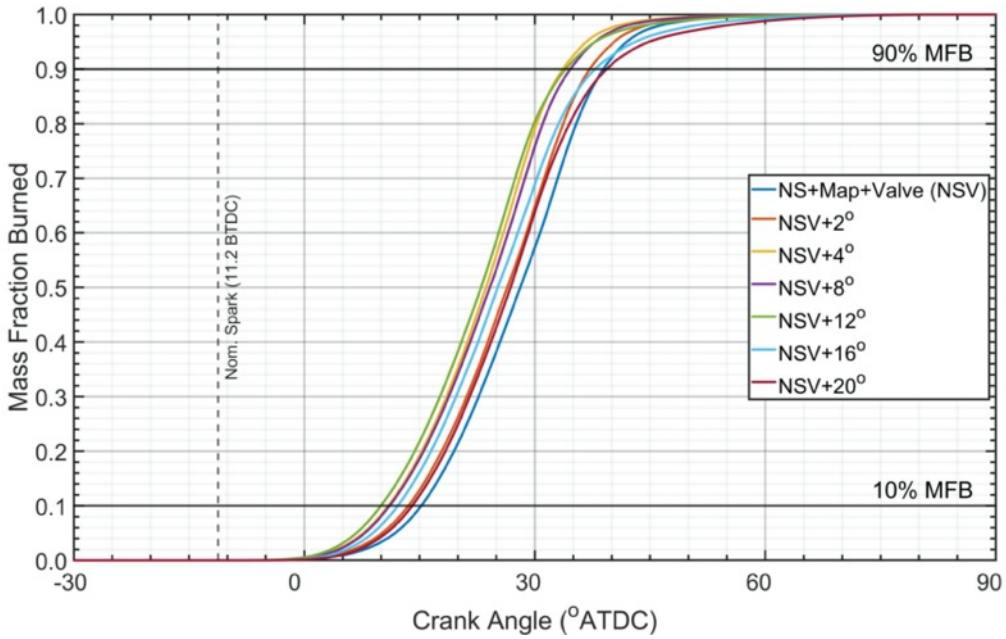

Figure 3.17: Crank angle resolved mass fraction burned for the increased valve duration cases.

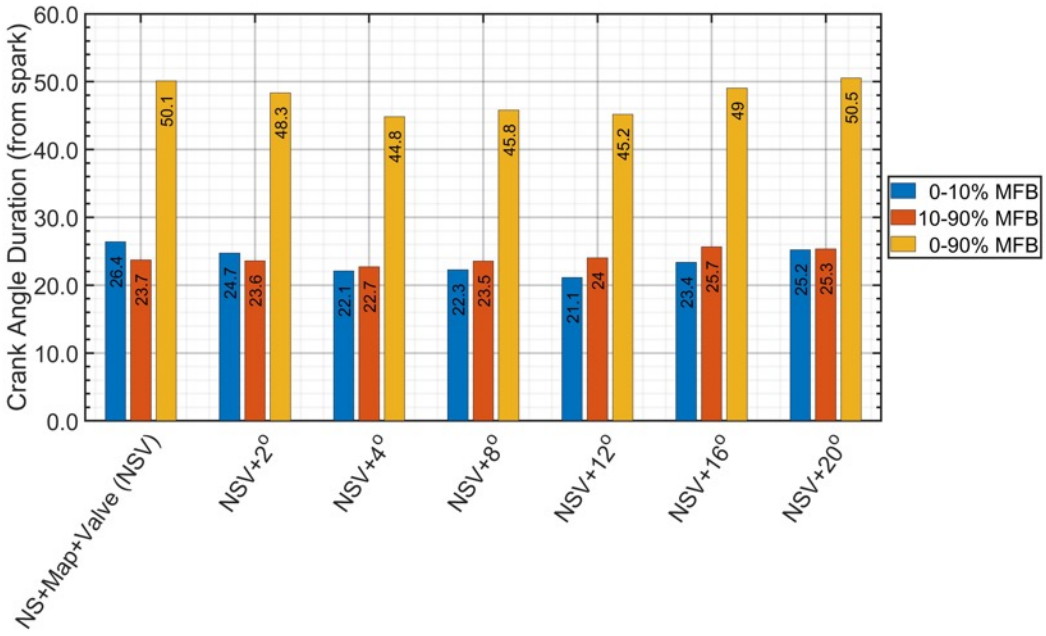

Figure 3.18: Crank angle durations for mass fraction burned curves.

development, rapid-burning, and overall burning periods. Together, these offer insights into the behaviors observed in the overall pressure traces. The longest flame initiation period was observed in NSV, and as the valve injection duration increased, the flames initiated quicker. Cases NSV+4° and NSV+8° possessed roughly equivalent development periods of 22.1CAD and 22.3CAD, respectively. Once the valve was duration was increased by 8CAD or more, the flame initiation period began to lengthen again, and the shortest of 21.1CAD was found by increasing the valve duration by 12CAD. For the rapid-burn period and overall burn angles, a similar trend was found of initially decreasing durations, then increasing once valve durations were increased by 8CAD or more. Of note, Figure 3.17 showed decreases in the burn rates during the flame termination period for valve increases of 16CAD and 20CAD, indicated by reductions in the curve slopes above 90% MFB.

Fundamentally, while the curves shown above do indicated changes in trends as the fuel injection period is increased, variations between cases were ultimately small. As discussed previously, fuel header pressures were reduced with increasing injection duration in order to maintain matched ERs. If injection pressure acts as the primary factor effecting chamber stratification and was responsible for the majority of differences observed, it stands to reason that with pressures of such low variation, stratification levels between cases would be similar.

In order to provide a quantification of chamber stratification, Figure 3.19 displays the total mass within the simulation domain categorized by ER, captured 0.3CAD before spark. For example, just before spark, approximately 15% of the domain in case NSV+20° has local ERs between 0.7 and 0.8, while 10% of the domain in NSV has local ERs between 0.8 and 0.9. Binning across all cases was similar, further supporting the

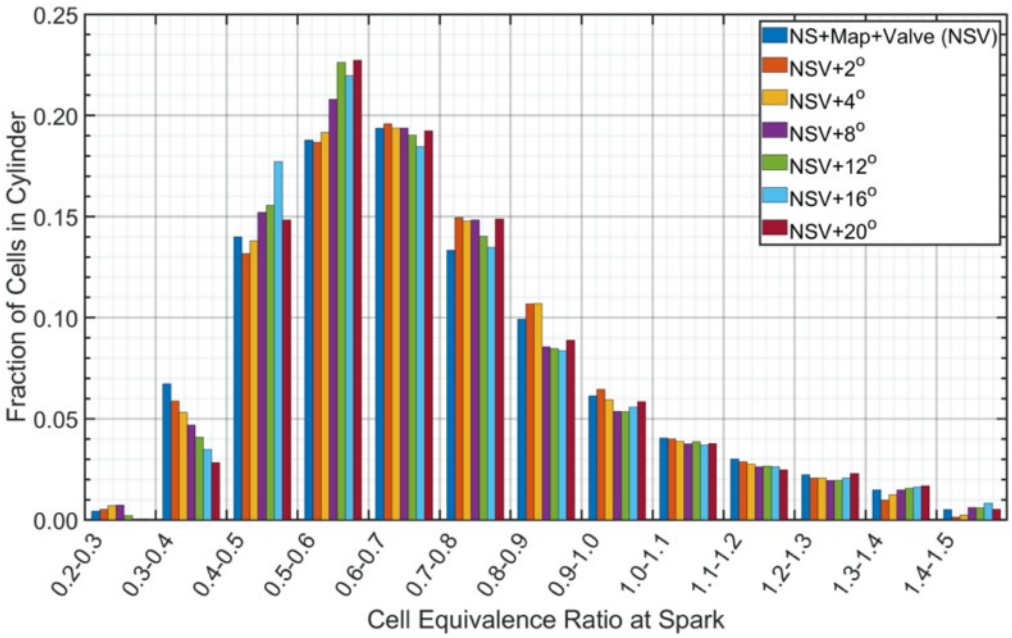

Figure 3.19: Fraction of cells in the domain binned by equivalence ratio.

relatively small changes in performance observed in the MFB curves. If the relatively similar injection pressures were the cause of similar stratification rather than the interaction between the incoming fresh air and fuel valve timings themselves, the significantly larger pressure differences tested by decreasing the valve injection durations would be expected to show larger variations in performance.

3.2.2. Decreasing Overall Injection Duration

To investigate the impact of reducing the overall injection duration, the electronic valve profile was modified and decreased by increments of 4CAD, 8CAD, 12CAD, and 16CAD (graphically shown previously in Figure 2.26), and fuel header pressures were raised to maintain matched global ERs. Table 3.3 reiterates the adjustments to the valve durations, as well as the final pressures required. As a validation of the desired 1% tolerance relative to the NS ER target, Figure A.7 in APPENDIX A: Additional Figures shows the global ERs for all decreased injection period cases. This ensures that ER was not a factor for variations in performance.

Table 3.3: Summary of decreased injection timings and pressures.

	Case	Valve Open (CAD)	Valve Close (CAD)	Fuel Pressure (kPa)
Baseline	NSV	-129.5	-103.5	142.0
Decreased Injection Period	NSV-4°	-127.5	-105.5	149.8
	NSV-8°	-125.5	-107.5	168.9
	NSV-12°	-123.5	-109.5	214.4
	NSV-16°	-121.5	-111.5	326.3

Figure 3.20 below shows the results for crank angle resolved cylinder pressure as it changes according to shortening the valve lift profile and increasing fuel injection pressure. Compared to NSV, decreasing the valve lift duration by 4CAD first decreased the peak

pressure and retarded LoPP. Once the lift was shortened by 8CAD however, peak pressures began to increase and advance. NSV-12° reached a maximum compared to other cases with a peak pressure of 2.30MPa at 25.94°ATDC, 29.94% higher than NSV and 10.09CAD earlier. After NSV-12°, further decreasing the lift by 16CAD experienced a sharp drop-off in pressure to 1.55MPa and a retarded LoPP compared to NSV. Table 3.4 summarizes the peak pressures, percentage increase relative to NSV, LoPP, and LoPP relative to NSV.

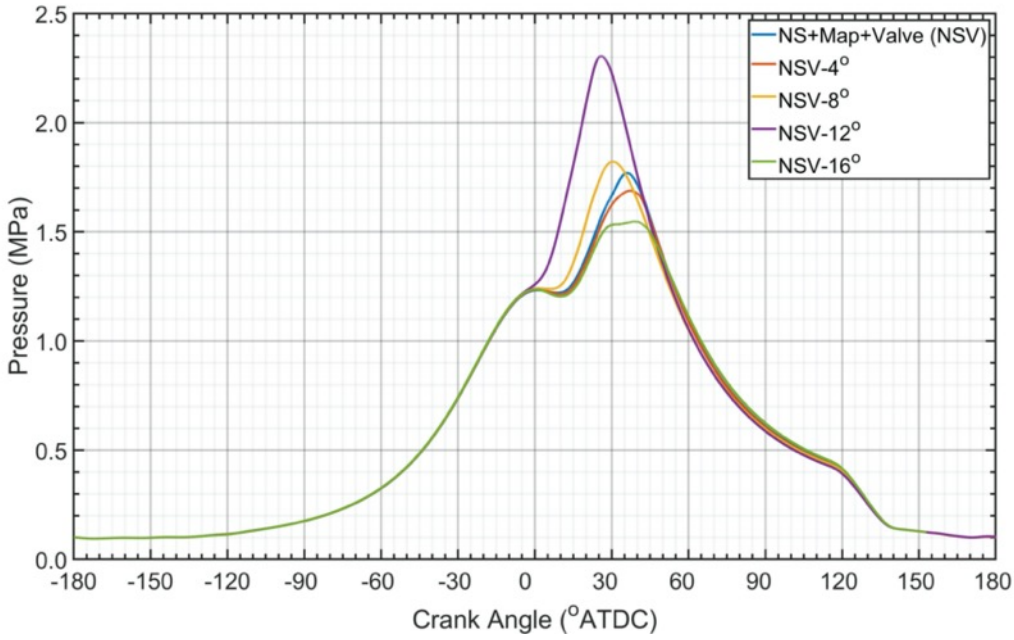

Figure 3.20: Cylinder pressure for all decreased fuel injection period cases.

Table 3.4: Summary of decreased valve duration pressure data.

Case	Peak Pressure (MPa)	Percentage Increase from NSV (%)	LoPP (°ATDC)	LoPP Ret./Adv. from NSV (CAD)
NSV	1.77	-	36.03	-
NSV-4°	1.69	-4.52	37.10	1.07 RET
NSV-8°	1.82	2.82	30.47	5.56 ADV
NSV-12°	2.30	29.94	25.94	10.09 ADV
NSV-16°	1.55	-12.43	38.83	2.80 RET

Similar to the analysis of the longer valve duration cases, MFB was examined to begin to characterize the changes in combustion to produce the varied pressure traces. Figure 3.21 displays the crank angle resolved mass fraction burned profiles for the decreased duration cases, while Figure 3.22 shows the overall durations of the flame development, rapid-burning, and overall burning periods. Decreasing the injection duration between NSV and NSV-4° produced a negligible change to the ignition delay, but further decreases of 8CAD and 12CAD began to result in faster ignition before ultimately decreasing again with NSV-16°. NSV-12° produced the fastest flame development period of 18.7CAD. An different trend was observed within the rapid-burning phase. Between NSV and NSV-4°, rapid-burning periods were similar, but then NSV-8° experienced a slower burn. NSV-12° then propagated significantly faster before the period slowed again once the injection was

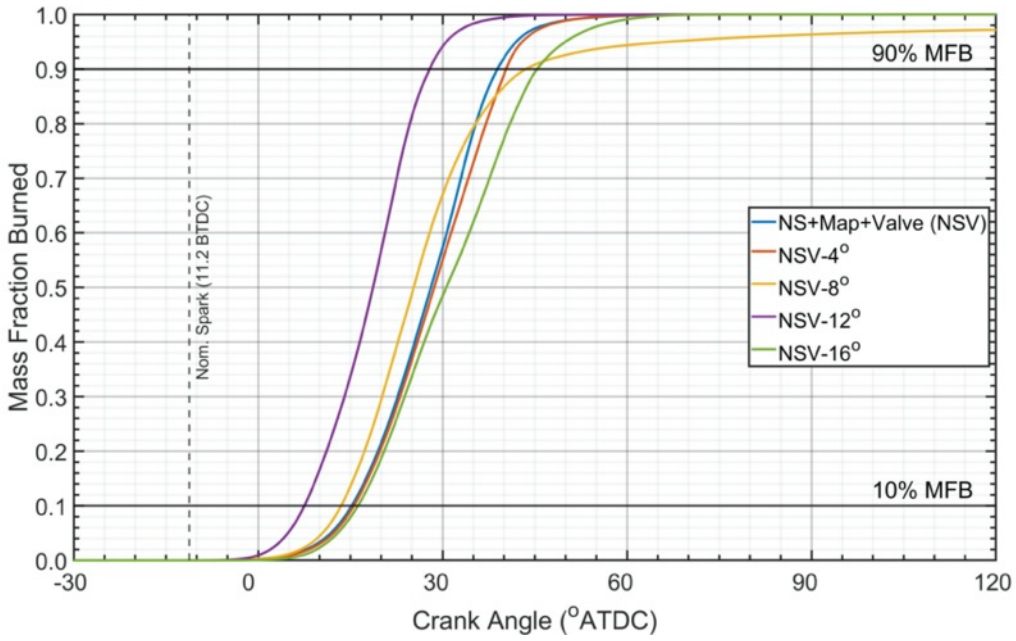

Figure 3.21: Crank angle resolved mass fraction burned for the decreased valve durations and higher injection pressures.

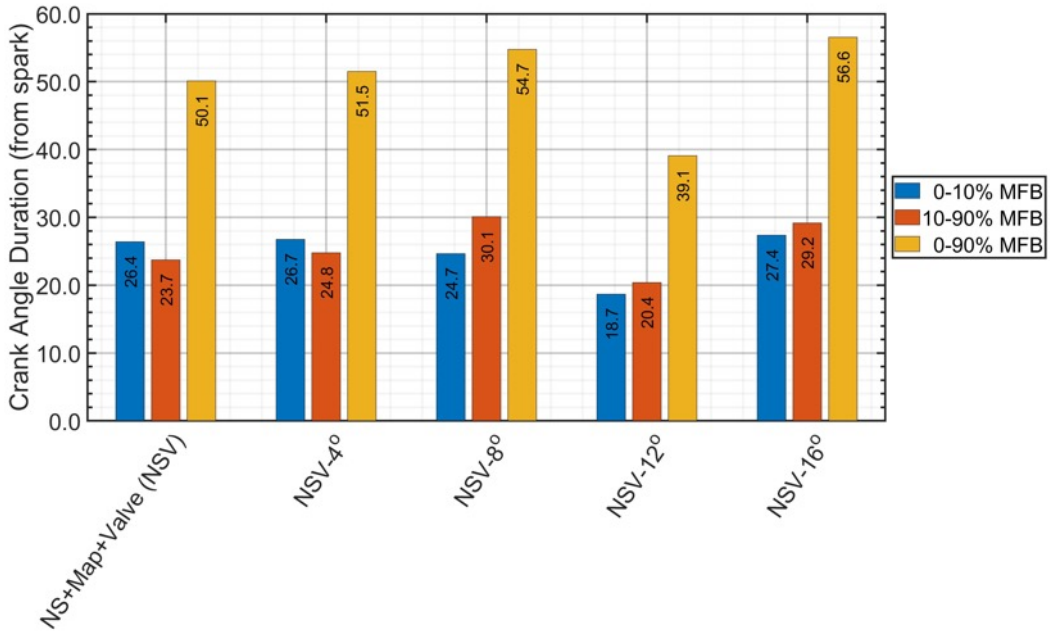

Figure 3.22: Crank angle durations associated with the MFB curves for the decreased valve lift duration cases.

reduced by 16CAD in NSV-16°. Regarding overall burn durations, decreasing the injection period unanimously increased the 0-90% MFB period, with exception of NSV-12° that provided an overall burn duration 11CAD shorter than baseline. Of note, NSV-8° displayed notably odd behavior, indicated by a noticeable decrease in burn rate near 30°ATDC and flame termination before completing a full burn of the chamber.

Previously, it was postulated that the higher injection pressures associated with decreasing the injection durations would promote a more homogeneous MCC and produce higher cylinder pressures. In order to begin investigating the differences in performance, particularly the anomaly occurring in NSV-8° and why NSV-16° failed to produce higher pressures than NSV-12°, the total mass of the MCC was categorized according to ER, shown in Figure 3.23. These results display significantly more variation between cases that

that which was observed previously with the longer duration injections and lower fuel pressures. Most notably, NSV, NSV-4°, and NSV-8°, showed similar overall stratification, but NSV-8° and NSV-12° showed significantly higher fractions of cells near the global ER targets. Higher injection pressures produced a more homogeneous MCC, and although NSV-16° was noticeably more homogeneous than cases of NSV-8° and longer,

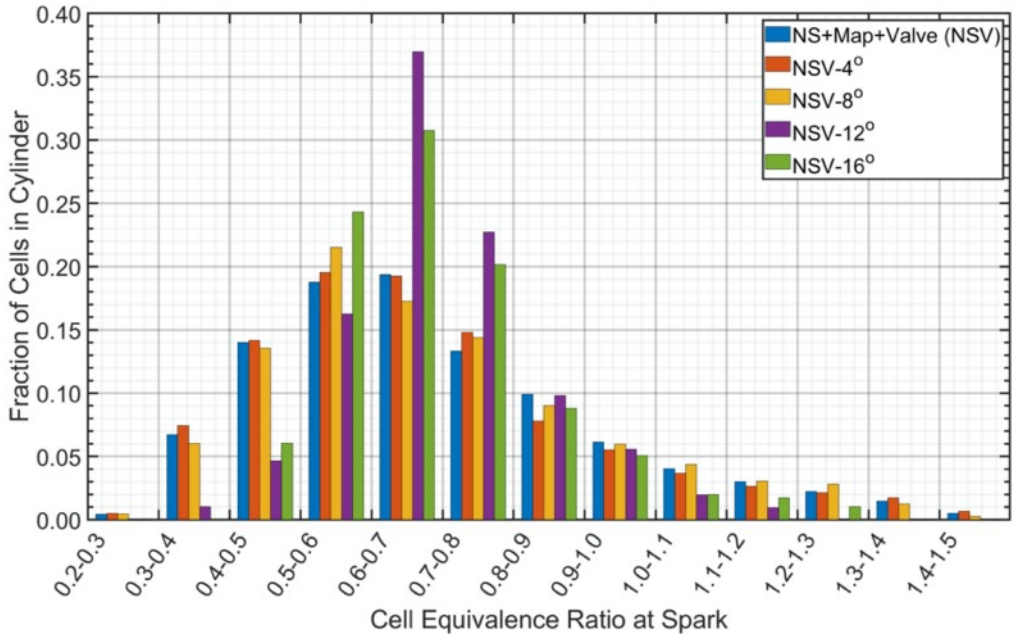

Figure 3.23: Fraction of cell in the domain binned by equivalence ratio for decreased fuel injection periods (higher injection pressures).

it still remained more heterogeneous than NSV-12°. The reduced mixing quality in NSV-16° compared to NSV-12° explains how the unexpected trend observed in the MFB curves occurred, but fails to explain why NSV-16° homogenized more poorly than NSV-12° or the early flame termination of NSV-8°.

Examining the spatial flame front propagation may reveal clues as to why NSV-8° failed to finish burning. In Figure 3.24, the flame propagation has been visualized by a

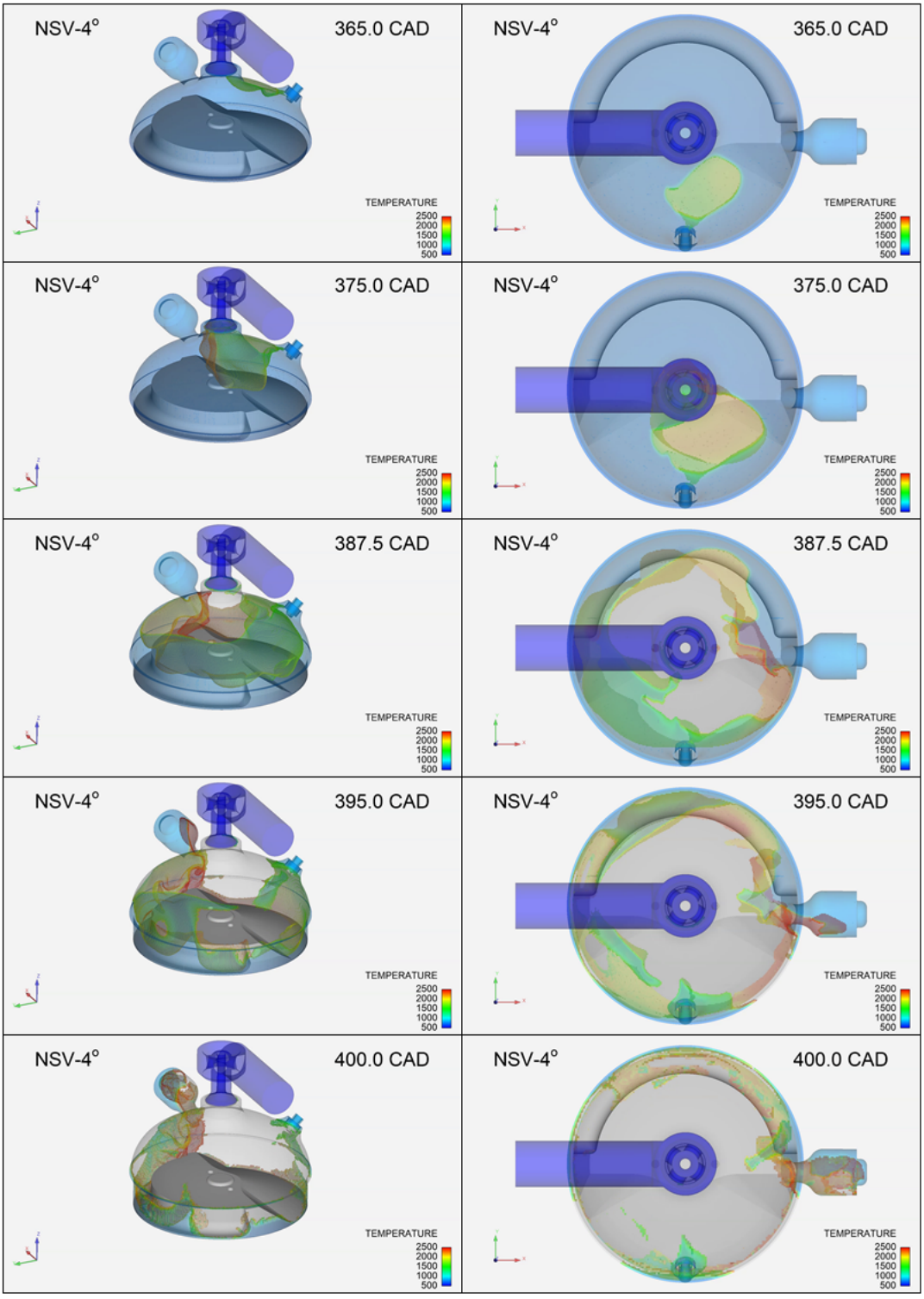

Figure 3.24: Typical flame front propagation in the MCC during case NSV-4° visualized using a CH4 volume colored by temperature.

showing a solid volume in any cell containing more than 1e-05 mole fraction CH4, which was then colored according to temperature. As the flame travels and burns the CH4, the volume disappears. For example, at 365CAD (5°ATDC), the MCC was largely unburned and cool, showing a nearly full-chamber of blue (between 500K and 1000K) volumes pre-combustion. By 400CAD (40°ATDC) the volumes have nearly disappeared, save for residual pockets of CH4 in the air-start cavity, near the surface of the piston crown, and near the spark plug. The fuel supply piping upstream of the DI valve remains solid and uniformly less than 500K for the entire combustion event. On the left, the domain is shown in an isometric view, while the exact same moments in simulation time are shown in top view on the right.

NSV-4° was selected as a case displaying normal flame propagation and burn characteristics. The flame front begins to appear and expand just after spark at 348.8CAD, and the front has begun to travel up toward the DI valve while expanding radially at 365CAD. The flame then continues to expand out and down toward the cylinder walls. At approximately 392.5CAD, the flame begins to enter and burn the air-start cavity. By the end of the cycle and flame termination, small pockets of unburned CH4 remain in the crevice surrounding the spark plug and near the piston crevice. NSV-12° may be found in Figure A.8 of APPENDIX A: Additional Figures as a second case showing regular flame dispersion.

Figure 3.25 below shows the flame front at similar checkpoints during the NSV-8° case. Compared to NSV-4° which burned fully, NSV-8° possesses one major difference.

Usually, the flame front wraps expands radially around the cylinder and then begins to wrap downward while simultaneously burning into the air-start cavity, but in NSV-8°, the flame

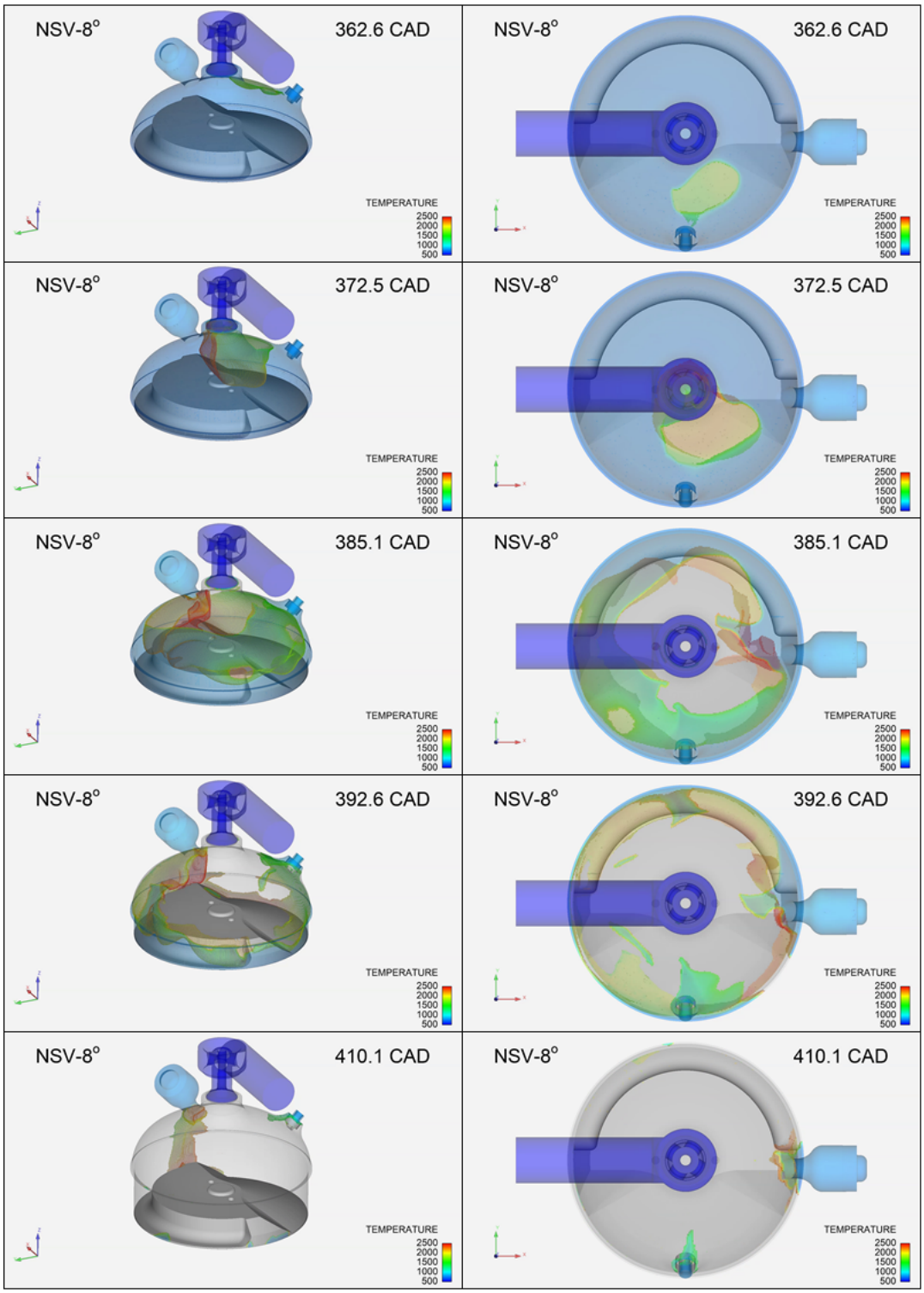

Figure 3.25: Flame front propagation in the MCC during case NSV-8° visualized using a CH4 volume colored by temperature.

front intersects itself just before the entering the throat of the air-start cavity. This intersection then prevents the flame from propagating into the cavity, leaving residual unburned CH4. The fuel left in that region produces the incomplete burn discovered in the MFB curves of Figure 3.21.

NSV-16° was also examined to determine why a continued decrease in injection duration and increase in pressure failed to produce better homogeneity and lower combustion durations. Figure 3.26 illustrates the fuel injection period for NSV-4°, shown on the left as a good model, against NSV-16°, shown on the right. Velocity streamlines were plotted to visualize the flow field in the MCC, and transparent isosurfaces of cell ER were added to illustrate the influx of fuel and gradient of mixing. Five colored isosurfaces were plotted, ranging from ERs of 0.5 (blue) to 1.5 (red) in increments of 0.25.

At the beginning of the injection period at 240CAD (-120°ATDC), NSV-4° clearly shows the existing flow field loop created by the cross-scavenging and gas exchange of the intake and exhaust ports. The fuel can be seen flowing through the valve at the top middle of the cylinder head and being caught by the existing flow, wrapping down toward the piston crown and around the chamber in a counter-clockwise fashion. Well after the valve has closed, the fuel continues to swirl around the cylinder, and gradually becomes more homogeneous. This contrasts strongly with NSV-16°, where the stream of fuel injected may be seen to over-penetrate straight through the existing flow field, impact the piston crown, and mushroom back up the cylinder. In a study by Hung, et al. on a low pressure direct injection gasoline engine, it was suggested that injection produced better mixing by reducing

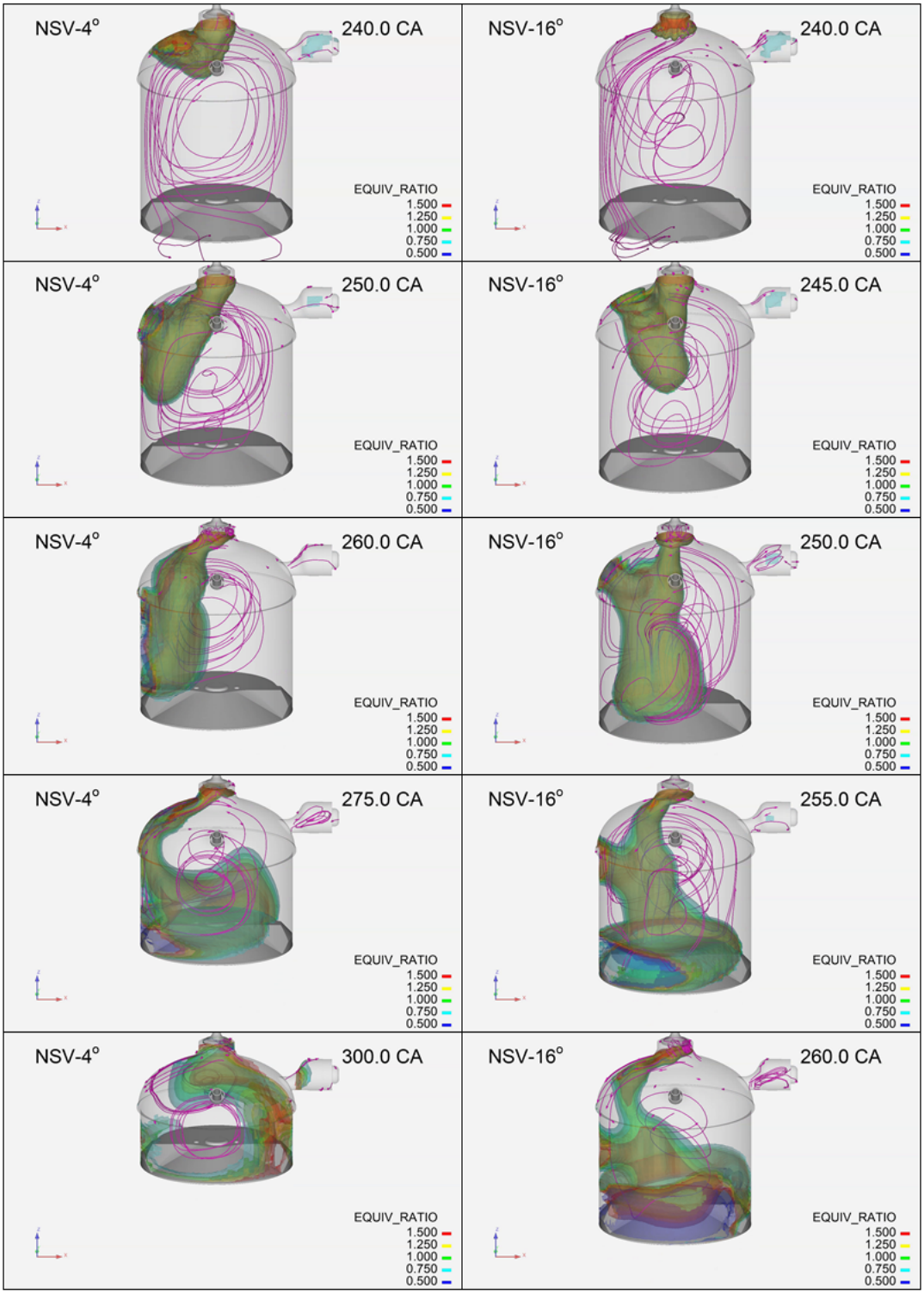

Figure 3.26: Compared isosurfaces of equivalence ratio used to visualize fuel mixing into the MCC during the fuel injection period between NSV-4° and NSV-16°.

interaction with the boundaries of the chamber, namely the liner walls and piston crown [21]. While the fuel still eventually mixes prior to spark and does ignite as a fully firing cycle, poor mixing quality caused by impacting the piston produced the weaker combustion event shown previously.

3.2.3. Reducing Fuel Pressure With Decreased Injection Duration

The final objective of the study was to take the valve lift profile that created the most favorable stratification for the fuel injection system and test it at progressively lower fuel header pressures to reach a minimum global ER before producing a misfire. The goal was that by utilizing the most favorable profile, a leaner cycle could produce similar pressure to the original baseline, reducing fuel consumption, or conversely, use the same amount of fuel to produce higher pressure. After testing the injection duration with both longer and shorter profiles, the profile of best performance was deemed to be NSV-12°. NSV-12° produced a significant increase in cylinder pressure while still maintaining the same global ER as NSV. Table 3.5 lists the reduced level 1, 2, and 3 (decreased in increments of 5kPa) fuel header pressures that were tested with the 12CAD reduced injection period, as well as the global ERs that were obtained.

Table 3.5: Reduced fuel pressures tested with 12CAD reduced injection timing.

Case	Fuel Header Pressure (kPa)	Measured ER
NSV	142.0	0.689
NSV-12°	214.4	0.691
NSV-12° Reduced Fuel Pressure 1	210.0	0.677
NSV-12° Reduced Fuel Pressure 2	205.0	0.660
NSV-12° Reduced Fuel Pressure 3	200.0	0.644

The impact of reducing the fuel header pressures while maintaining the same valve lift profile and injection duration on cylinder pressure is shown below in Figure 3.27. The electronic valve baseline, NSV, was included for reference. Relative to case NSV-12°,

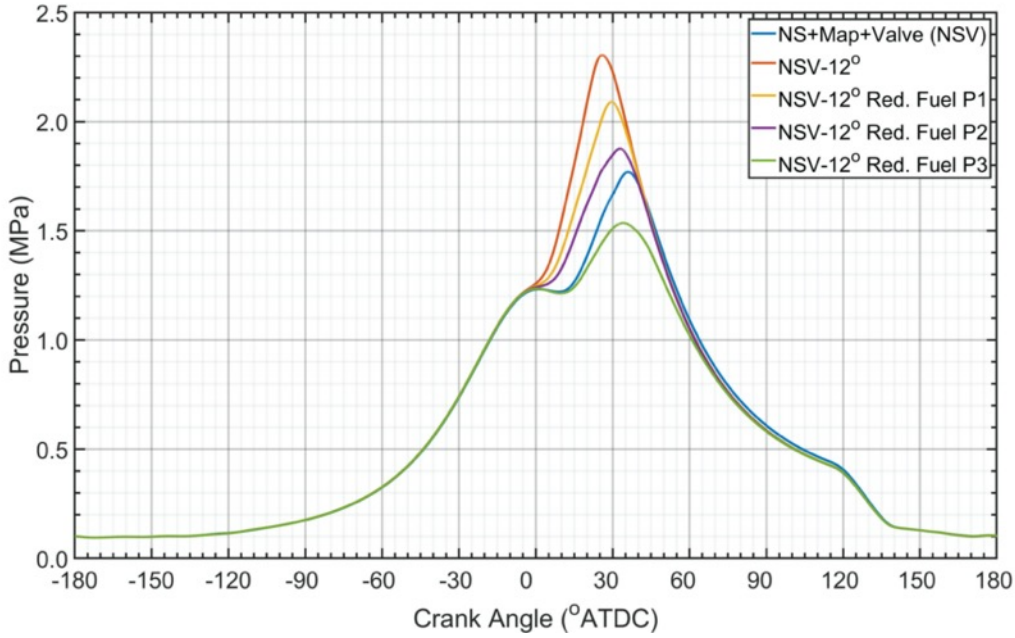

Figure 3.27: Cylinder pressures obtained by sweeping fuel header pressure with the NSV-12° lift profile.

reducing header pressure produced a straightforward trend. As fuel header pressure was decreased, peak pressure decreased, and LoPP retarded. NSV-12°, as well as cases Red. Fuel P1 and P2 both produced higher peak pressures and earlier LoPPs compared to the NSV baseline, while Red. Fuel P3 produced a lower peak pressure than NSV but still an earlier LoPP. Table 3.6 summarizes the peak pressures, percentage increase relative to NSV, LoPP, and LoPP relative to NSV. Pressure levels below P3 resulted in misfires and are not presented.

Table 3.6: Summary of reduced fuel cylinder pressure data.

Case	Peak Pressure (MPa)	Percentage Increase from NSV (%)	LoPP (°ATDC)	LoPP Ret./Adv. from NSV (CAD)
NSV	1.77	-	36.03	-
NSV-12°	2.30	29.94	25.94	10.09 ADV
Red. Fuel P1	2.09	18.08	29.62	6.41 ADV
Red. Fuel P2	1.88	6.21	32.86	3.17 ADV
Red. Fuel P3	1.54	-12.99	34.11	1.92 ADV

MFB was once again examined to characterize the changes in the cycles observed. Figure 3.28 shows the crank angle resolved mass fraction burned profiles, while Figure 3.29 shows the overall flame development, rapid-burn, and overall burn durations. As the fuel header pressure was reduced, the flame development period, rapid-burning period, and overall burn durations all increased with decreasing fuel pressure. Of note, Reduced Fuel P3 produced a near identical flame development duration to the NSV baseline but with a

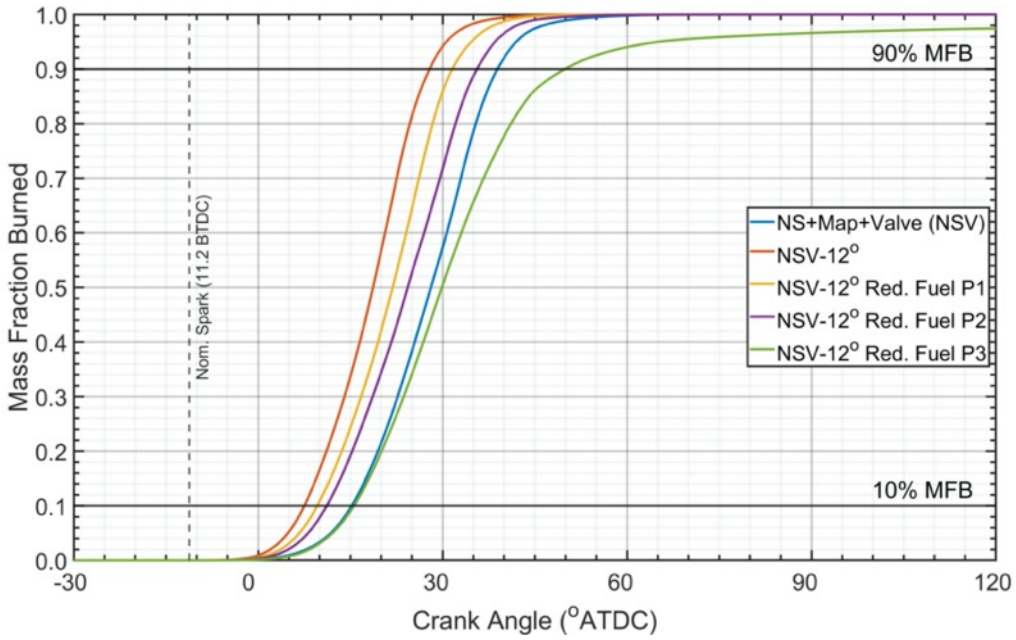

Figure 3.28: Crank angle resolved mass fraction burned for the reduced fuel header pressure cases.

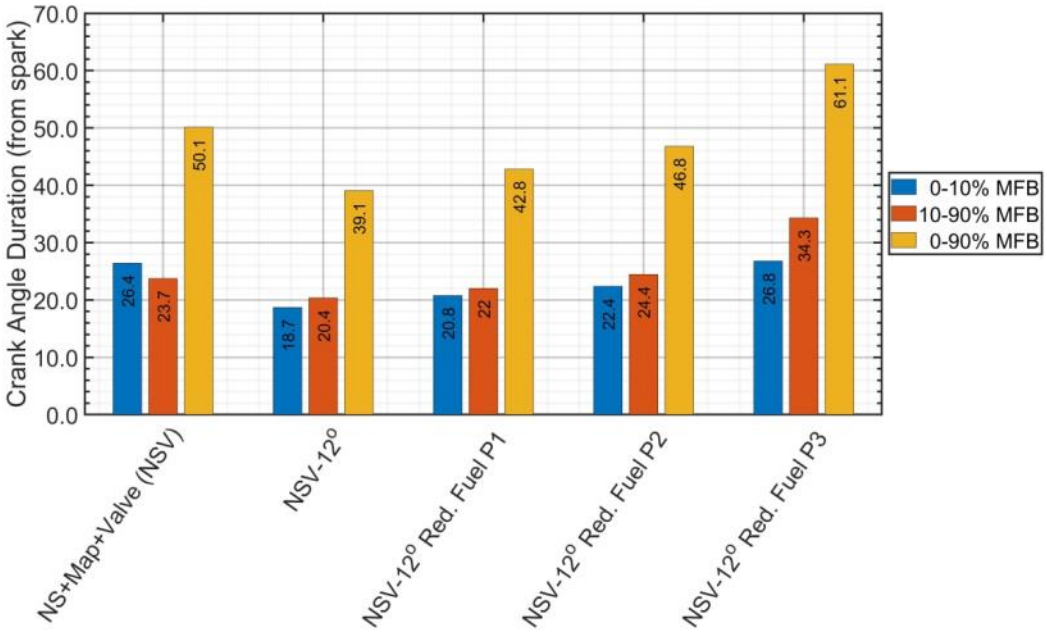

Figure 3.29: Crank angle durations associated with the MFB curves for the reduced fuel header pressure cases.

rapid-burn period nearly 10.6CAD longer. Similarly, Reduced Fuel P3 was also began to misfire and failed to burn completely. As a result, Reduced Fuel P2 was considered the lowest achievable global ER before producing a misfire. By using a reduced fuel injection period with higher injection pressure, NSV-12° Red. Fuel P2 produced 6.21% higher peak pressure while using 4.21% less fuel.

4. SUMMARY AND CONCLUSIONS

This study simulated a full crank cycle of the natural gas two-stroke spark ignited Ajax E-565, then validated the numerical simulation using experimentally obtained datasets. The simulation was then used to analyze performance changes produced by manipulating the low pressure direct injection system. A computational fluid dynamic simulation was built in commercial software Converge CFD, then validated at a variety of spark timings. The effect of altering the fuel injection period and injection pressures was then examined by first lengthening the injection period then shortening the injection period. Fuel header pressures were varied to compensate for the altered injection durations in order to maintain a constant global ER. Lastly, the best performing injection parameters of reducing the injection duration by 12CAD were tested at progressively lower fuel header pressures until misfire. The lower header pressures were then analyzed for fuel and performance benefits. The ultimate objectives were to accurately simulate an entire cycle of the Ajax E-565 including the DI fuel delivery system, as well as determine how to manipulate the DI system to reduce global ER and lower fuel consumption without reducing pressure.

In order to validate the simulation and assess the effectiveness of utilizing a CFD model to predict engine performance, numerical results were compared against experimental datasets for nominal spark timing, 5° retarded spark timing, and 10° advanced timing. After successfully validating pressures in the air manifold, exhaust manifold and main chamber, the numerical traces were shown to match very well against individual experimental cycles.

While testing increased injection durations, peak pressure was found to initially

increase with increasing duration then decrease with increasing durations above 8CAD. Similarly, LoPP was found to advance with increasing injection duration. When MFB was examined to characterize the combustion characteristics, overall combustion duration showed similar trends to peak pressure, and overall chamber stratification was determined to vary little with increase in injection duration due to relatively similar injection pressures.

Decreasing injection duration and increasing injection pressure brought greater variation than the previous increased duration cases. Maximum pressure and earliest LoPP was obtained by decreasing the injection duration by 12CAD with an injection pressure of 214.4kPa. The cylinder pressure measured was nearly 30% higher and 10CAD earlier than the baseline. In general, with exception of the 12CAD decreased case, overall combustion duration increased with decreasing injection period. Increasing injection pressure also tended to produce a more homogeneous main chamber mixture.

Due to producing the highest pressure, the 12CAD reduced injection case was tested at progressively lower fuel header pressures. As injection pressure decreased, peak pressure decreased, and LoPP retarded. A misfire was produced at an ER of 0.644, so then next lowest case was deemed the lowest attainable global ER attainable before misfire. This case utilized an injection pressure of 205kPa and produced 6.21% higher pressure using 4.21% less fuel than the baseline case. After investigating reduced performance with 16CAD injection duration, it was discovered that at such a high injection pressure, the fuel stream broke through the scavenging loop flow and directly impinged upon the piston.

The study produced a number of notable conclusions. First and foremost, the model was shown to be sufficiently high-fidelity as to predict real world engine behavior within

small margins during the validation phase. Not only did this meet the first objective of accurately simulating a full cycle of the Ajax E-565, but it also built trust in the use of CFD models to further examine processes difficult to study through experimental means. Notably, many factors regarding the DI fuel system were unknown, and the model was used to prove the ability to iteratively converge to the best predicted header pressure, valve lift, and valve opening timings. Finally, the highest cylinder pressure and lowest fuel consumption was found by decreasing the fuel injection period and using higher fuel injection pressure. Overall, investigation revealed that in order to obtain the most favorable chamber stratification, effort should be made to utilize as high an injection pressure as possible, without either impinging upon a solid wall (piston crown, cylinder liner, etc.) or over-penetrating the flow field produced by the scavenging loop. This maximized cylinder pressure while minimizing fuel consumption for a given global ER.

5. FUTURE WORK

The results of this study were certainly not exhaustive, but a number of ideas could be implemented to further the research goal. A number of suggestions are presented below:

1. An additional study could investigate the design of the direct injection system and intake manifold. If the system could be designed with greater control over the plume of fuel and scavenging flow, there may be ways to further improve on the mixing characteristics and reduce cycle-to-cycle variability.
2. Faster injection periods at higher pressures were shown to produce favorable characteristics, such as fuel savings and the ability to produce more work. With that being the case, shorter injection periods may be able to be shifted even later in the cycle, closer to spark. An investigation could be performed into shifting the injection later in the cycle.
3. The engine is still highly inconsistent cycle-to-cycle, and the simulation built here would be a good basis to perform an extensive cyclic variability study. CFD may be able to offer insights as to why, as well as test various parameters to improve that variability at relatively low cost. CFD could easily be used to bypass certain components of engine operability to examine best case scenarios and isolate problematic components.
4. Improving emissions should always be at the forefront. This study and findings could be examined to investigate if the same valve parameters and injection pressures could be used to reduce harmful emissions.

6. REFERENCES

[1] Cooper Machinery Services, "AJAX(TM) E-565 Gas Engine," 05 2020. [Online]. Available: https://www.cooperservices.com/wp-content/uploads/2020/06/AJI20026-Ajax-E-565-Engine-r0-web.pdf.

[2] M. D. Ruter, D. B. Olsen, M. V. Scotto and M. A. Perna, Performance of a Large Bore Natural Gas Engine with Reformed Natural Gas Prechamber Fueling, San Antonio, TX: ICEF2010, 2010.

[3] J. B. Heywood, Internal Combustion Engine Fundamentals, New York: McGraw-Hill Companies, Inc., 2011.

[4] J. B. Heywood and E. Sher, The Two-Stroke Cycle Engine, Ann Arbor, MI: Taylor & Francis, 1999.

[5] Cameron Compression Systems, Ajax E-565 Gas Engine Service Manual, Houston, Texas, 2013.

[6] G. P. Blair, Design and Simulation of Two-Stroke Engines, Warrendale, PA: Society of Automotive Engineers, 1996.

[7] Convergent Science, "Applications," Convergent Science, 2021. [Online]. Available: https://convergecfd.com/applications/internal-combustion-engines.

[8] Convergent Science, "Complex Moving Geometries," Convergent Science, 2021. [Online]. Available: https://convergecfd.com/benefits/complex-moving-geometries.

[9] Convergent Science, "Autonomous Meshing," Convergent Science, 2021. [Online].

Available: https://convergecfd.com/benefits/autonomous-meshing.

[10] Convergent Science, "High Performance Computing," Convergent Science, 2021. [Online]. Available: https://convergecfd.com/benefits/high-performance-computing.

[11] A. Mashayekh, Study of Conjugate Heat Transfer of a Spark-Ignited Natural Gas Engine Cylinder, PhD Dissertation, Texas A&M University, 2017.

[12] Atmos Energy - Mid-Tex / APT, "Chromatograph Report," College Station, TX, 2019.

[13] K. J. Richards, P. K. Senecal and E. Pomraning, CONVERGE 3.0 Manual, Madison, WI: Convergent Science, 2021.

[14] K. J. Richards, P. K. Senecal and E. Pomraning, CONVERGE Studio 3.0 Manual, Madison, WI: Convergent Science, 2021.

[15] G. P. Smith, D. M. Golden, M. Frenklach, N. W. Moriarty, B. Eiteneer, M. Goldenberg, C. T. Bowman, R. K. Hanson, S. Song, W. C. G. Jr., V. V. Lissianski and Z. Qin, "GRI-Mech 3.0," [Online]. Available: http://www.me.berkeley.edu/gri_mech/.

[16] J. Etcheverry, M. Patterson and D. Grauer, Virtual Design of an Industrial, Large-Bore, Spark-Ignited, Natural Gas, Internal Combustion Engine for Reduction of Regulated Pollutant Emissiosn, Dearborn, Michigan: ASME 2013 Internal Combustion Engine Division Fall Technical Conference ISEF 2013, 2013.

[17] Convergent Science, "ICE Modeling - Source Modeling," Madison, Wisconsin, 2019.

[18] A. M. Lippert, S. Chang, S. Are and D. P. Schmidt, Mesh Independence and Adaptive Mesh Refinement For Advanced Engine Spray Simulations, SAE 2005 World Congress and Exhibition, 2005.

[19] Cooper Energy Services, Ajax Fuel Injection, Corry, Pennsylvania: Cooper Industries, 2019.

[20] R. W. Woodard, "E-565 Timing Data," 1989.

[21] D. Hung., G. Zhu, J. Winkelman and T. Stuecken et al., *A High Speed Flow Visualization Study of Fuel Spray Pattern Effect on Mixture Formation in a Low Pressure Direct Injection Gasoline Engine,* 2007.

APPENDIX A: ADDITIONAL FIGURES

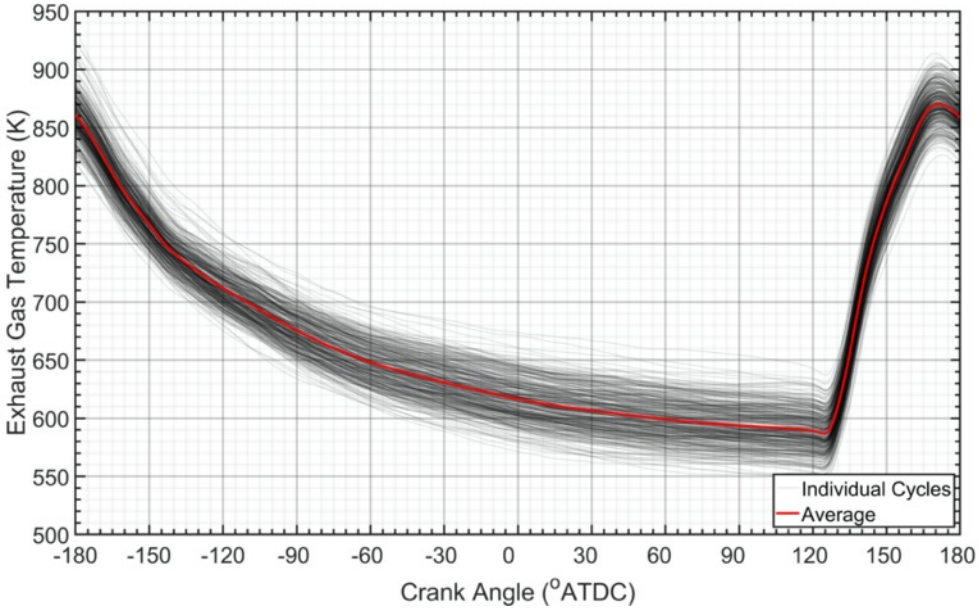

Figure A.1: 200 individual cycles of exhaust gas temperature for the nominal spark timing case overlaid with the 200-cycle average.

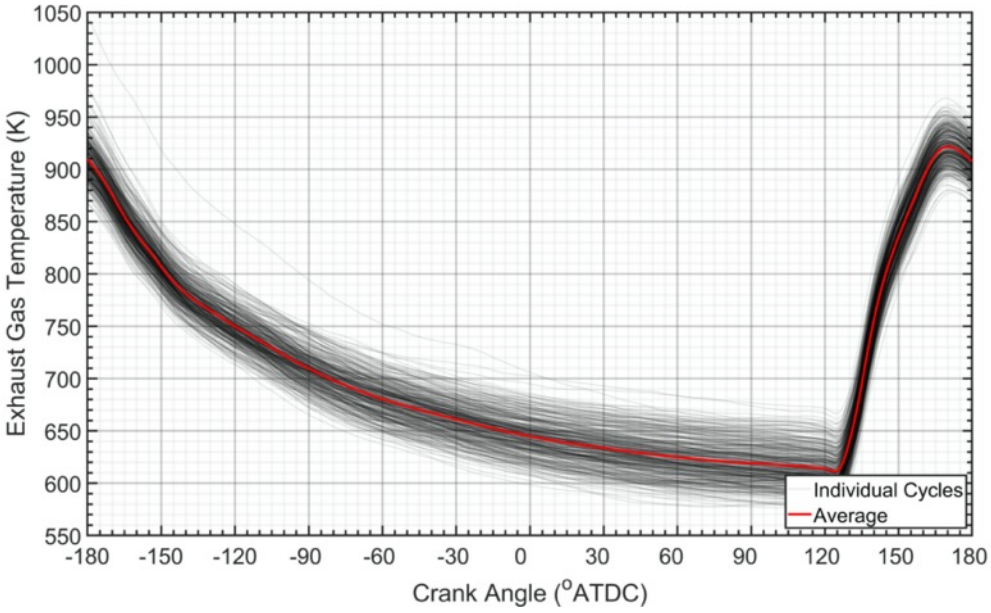

Figure A.2: 200 individual cycles of exhaust gas temperature for the retarded spark timing case overlaid with the 200-cycle average.

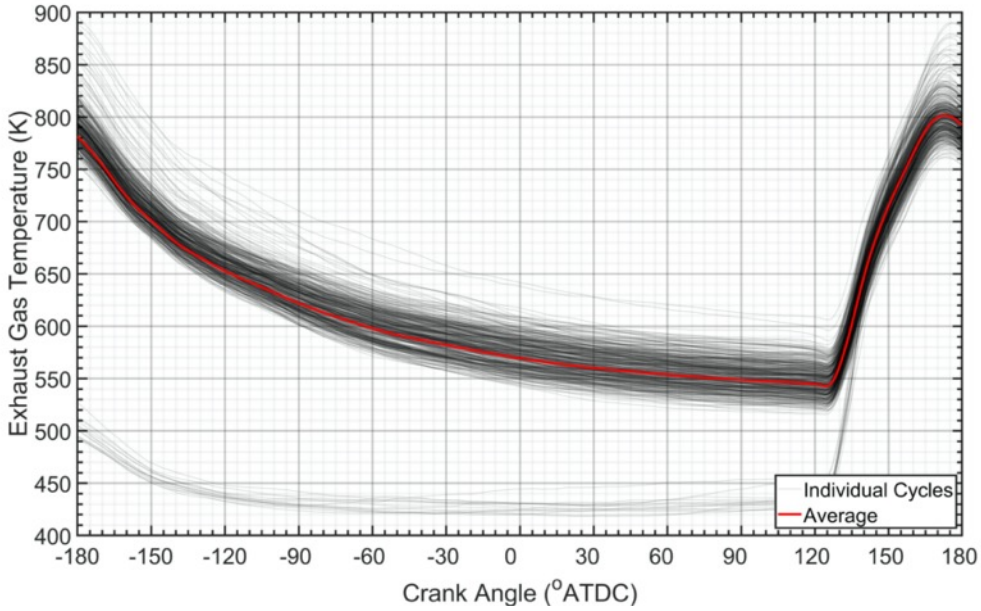

Figure A.3: 200 individual cycles of exhaust gas temperature for the advanced spark timing case overlaid with the 200-cycle average.

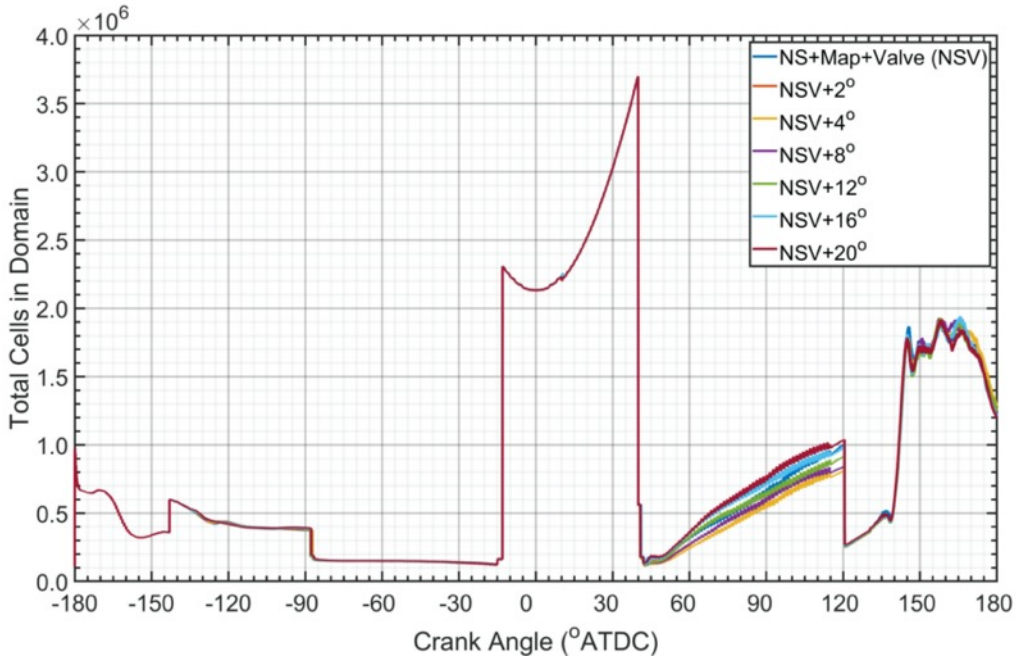

Figure A.4: Total cell counts for the increased dwell time cases.

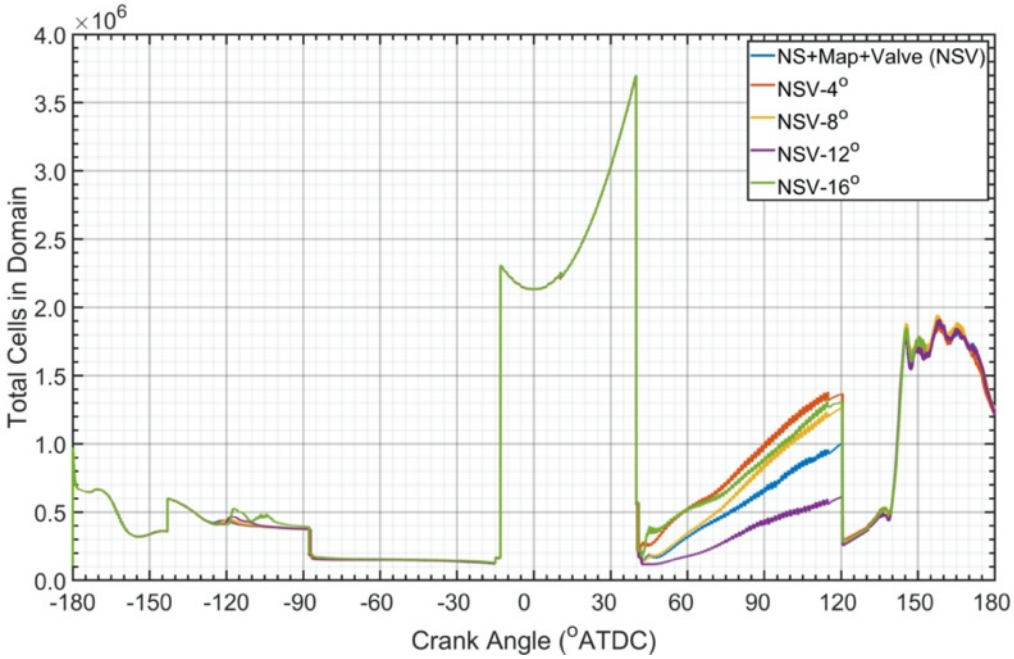

Figure A.5: Total cell counts for the decreased dwell time cases.

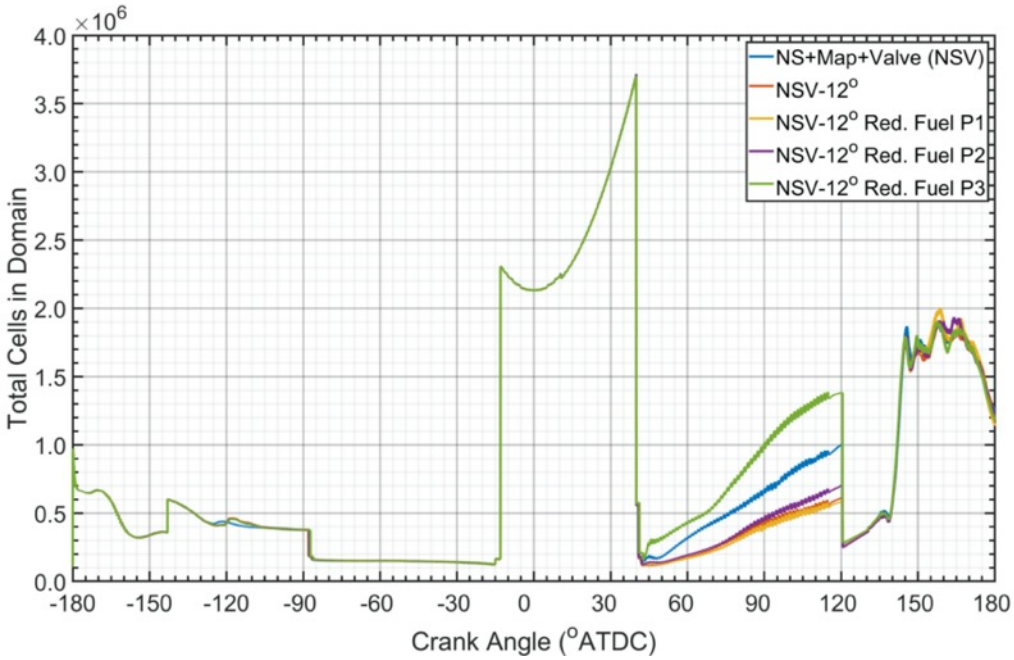

Figure A.6: Total cell counts for the fuel reduction study cases.

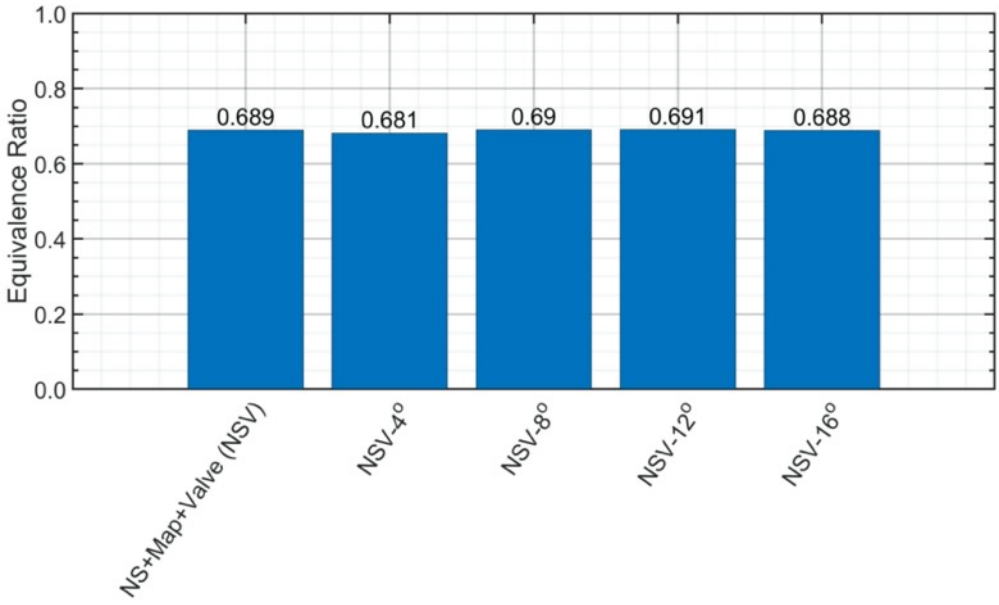

Figure A.7: Global equivalence ratios for all decreased injection period cases.

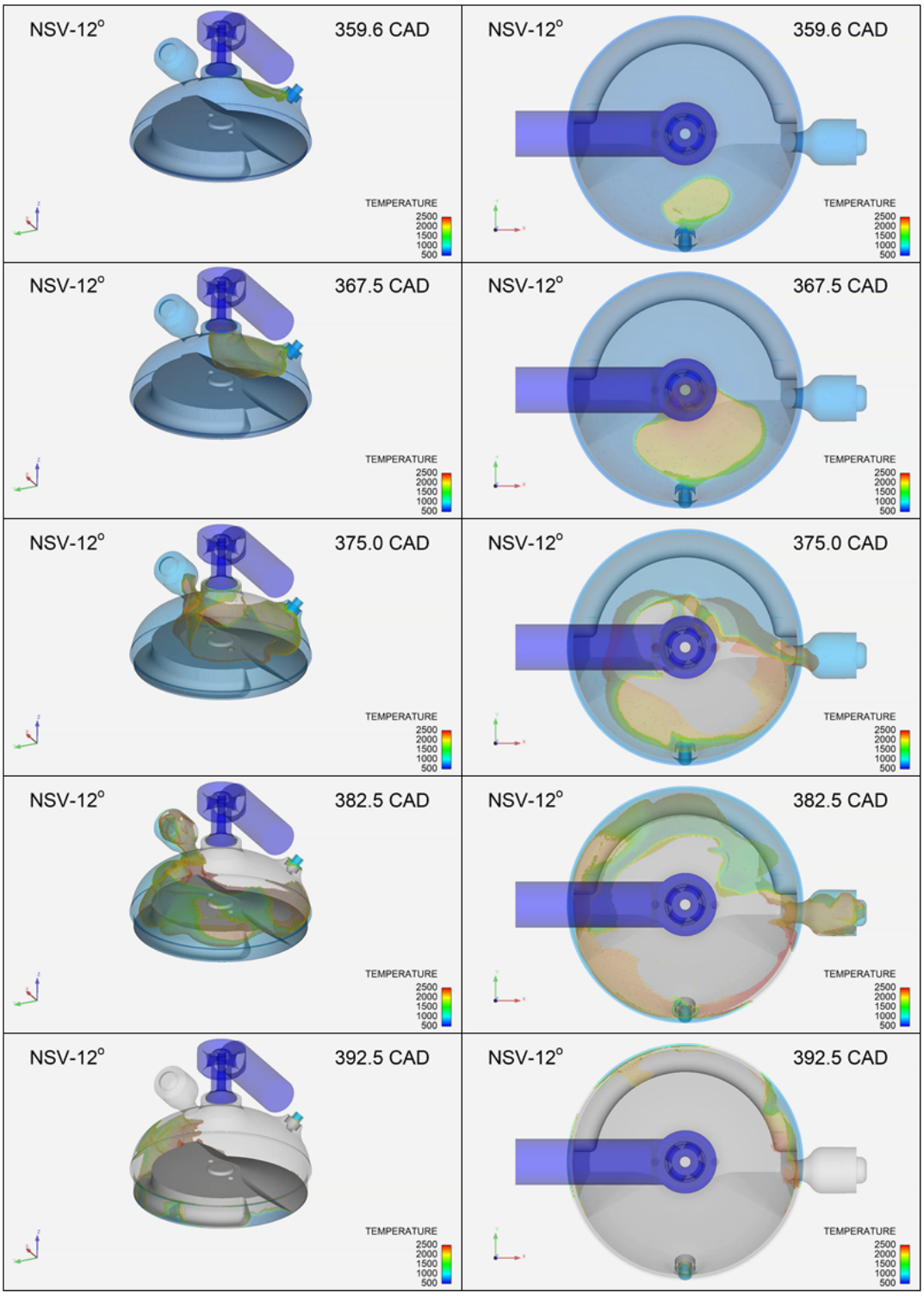

Figure A.8: Typical flame front propagation in the MCC during case NSV-12° visualized using a CH4 volume colored by temperature.

APPENDIX B: FUEL HEADER PRESSURE ESTIMATION

The behavior of fuel flowing from upstream of the injection valve into the main chamber was treated as the emptying of a pressure vessel. With these assumptions, the basic equation to represent the mass flow rate through an orifice is represented by the following:

$$\dot{m}_e = \rho_e A_e V_e \tag{1a}$$

where ρ represents the fluid density, A represents the area of the orifice, and V represents the fluid velocity. The naming convention of the subscript e represents exit conditions, for example in this case, the main chamber. By treating the fluid as an ideal gas, then the ideal gas equation may be used to solve for the fluid density and is given by:

$$\rho_e = \frac{P_e}{RT_e} \tag{2}$$

where P_e is the fluid pressure, T_e is the fluid temperature, and R is a universal gas constant. Treating the process as both isentropic and compressible allows for the following two relations to be used to obtain relationships between the stagnation properties and the Mach number of the flow:

$$\frac{P_o}{P_e} = \left[1 + \left(\frac{\gamma - 1}{2}\right) {M_e}^2\right]^{\frac{\gamma}{\gamma - 1}} \tag{3a}$$

$$\frac{T_o}{T_e} = 1 + \left(\frac{\gamma - 1}{2}\right) {M_e}^2 \tag{4a}$$

where γ represents the ratio of specific heats of the fluid and M_e the exit Mach number. The following is the definition of the Mach number:

$$M_e = \frac{V_e}{a_e} \tag{5a}$$

where a is a new parameter known as the sound speed of the gas and is defined by:

$$a_e = \sqrt{\gamma R T_e} \tag{6}$$

Substitution of equation (6) into equation (5) gives and solving for V_e gives:

$$V_e = M_e \sqrt{\gamma R T_e} \tag{5b}$$

If the fuel supply is considered a reservoir, then the properties within it represent the stagnation properties such that $T_o = T_{fuel}$ and $P_o = P_{fuel}$. The exit conditions are the chamber conditions so long as the flow remains subsonic (so that the backpressure equals the exit pressure). Solving for the main chamber conditions, the equations then become:

$$T_e = T_{fuel}\left[1 + \left(\frac{\gamma - 1}{2}\right) {M_e}^2\right]^{-1} \tag{4b}$$

Equation (3b) can be algebraically rearranged to solve for M_e:

$$M_e = \left\{\left[\left(\frac{P_{fuel}}{P_e}\right)^{\frac{\gamma-1}{\gamma}} - 1\right]\left(\frac{2}{\gamma - 1}\right)\right\}^{1/2} \tag{3b}$$

Substituting equations (3b) and (4b) into equation (5b) completes a final expression for V_e in terms of known quantities P_{fuel}, P_e, and T_{fuel}. Final substitution of equations gives a completed expression for the mass flow rate out of the fuel header region. After again substituting equations for the exit Mach number, exit pressure, and exit temperature, the total expression can then be simplified down to the final expression for the mass flow rate, where M_e is given by equation (3b):

$$\dot{m}_e = P_{fuel} A_e M_e \sqrt{\frac{\gamma}{RT_{fuel}}} \left[1 + \left(\frac{\gamma - 1}{2}\right) {M_e}^2\right]^{\frac{\gamma+1}{2(1-\gamma)}}$$

Taking flow losses into consideration by use of a discharge coefficient C_D gives:

$$\dot{m}_e = C_D P_{fuel} A_e M_e \sqrt{\frac{\gamma}{RT_{fuel}}} \left[1 + \left(\frac{\gamma - 1}{2}\right) {M_e}^2\right]^{\frac{\gamma+1}{2(1-\gamma)}}$$

Finally, the expression may be used to predict the mass flow rate of fuel entering the main chamber, which may subsequently be used to estimate global ER as a function of any of the parameters above, namely fuel header pressure. Simulation outputs from the nominal spark (NS) case were used to estimate main chamber conditions, and simulated mass flow rate between the fuel intake and main chamber regions was compared against the estimated mass flow rates to determine the discharge coefficient.